J. Fluid Mech. (1979), *vol.* 95, *part* 1, *pp.* 1–78
Printed in Great Britain

Unsteady flow in a collapsible tube subjected to external pressure or body forces

By ROGER D. KAMM AND ASCHER H. SHAPIRO
Massachusetts Institute of Technology, Cambridge, MA. 02139

(Received 19 June 1978 and in revised form 23 February 1979)

Flows in thin-walled, collapsible tubes are of fundamental importance to various physiologic phenomena and clinical devices.

A one-dimensional, unsteady theory is developed for flows generated either by externally applied pressures or by body forces. Part 1 deals with small-amplitude, linearized flows, part 2 with large amplitude, nonlinear flows. Experimental results for a tube collapsing under external pressure are given in part 3, together with theoretical interpretations and comparative results of numerical simulations.

Several new and unanticipated phenomena are revealed. These are in part associated with the highly nonlinear 'equation of state' (transmural pressure *versus* area) for a partially collapsed tube, and in part with whether the flow speed is sub- or supercritical relative to the speed of area waves. For instance, a flow produced by a spatially uniform external pressure applied to a limited region becomes choked at a flow-limiting throat at which point the fluid speed reaches the local wave speed. This throat forms at the edge of the pressurized region. The critical velocity can be exceeded with the application of certain types of spatially graded external pressures.

CONTENTS

1. Introduction *page* 2
2. Formulation of the one-dimensional theory 4

Part 1. Linearized theory for small amplitudes

3. Formulation of small-amplitude theory 7
4. Solution by a linear method of characteristics 8
5. Generation and transmission of waves 17
6. Distributions of applied pressure yielding the homogeneous wave equation 19
7. Solutions with prescribed area variation 27
8. Wave generation in a moving fluid 28
9. Wave transmission and reflexion in a moving fluid 31

Part 2. Nonlinear theory

10. Exact solutions for area changing only in time 36
11. The characteristic curves 37
12. Simple waves 38
13. Collapse of a tube by a ramp of external pressure 47
14. Numerical integrations of the characteristic equations 56

0022-1120/79/4305-7540 $02.00

Part 3. A simple experiment and its interpretation

15. Description of the experiment *page* 60
16. General character of the collapse process 62
17. Order-of-magnitude estimates 65
18. Experimental results and comparison with numerical integrations 68
19. Theoretical details of the collapse process 74

1. Introduction

1.1. *The problem*

This paper deals with unsteady, one-dimensional flows in thin-walled compliant tubes, particularly under conditions where the tube is partially collapsed as the result of a negative transmural pressure (internal pressure p minus external pressure p_e). The flows considered are generated either by the application of external pressure or by body forces. Also included in the theory are the effects of friction and other dissipative losses, of inflow from tributaries, and of non-uniformities due to longitudinal gradients in tube diameter and wall thickness.

1.2. *Context of the problem*

Flows in thin-walled distensible and collapsible tubes have numerous applications to physiology and to medical devices.

Previous investigations have dealt mainly with unsteady flows in the range of positive transmural pressures, with the vessel distended and of circular cross-section (Rudinger 1970; Attinger 1964; Olsen & Shapiro 1967; Kivity & Collins 1974; Beam 1968). These are applicable to a wide range of arterial blood flow conditions, but they fail when the transmural pressure, $p-p_e$, becomes negative and the vessel assumes a collapsed configuration.

Vessel collapse is most readily observed in the veins (e.g. the jugular vein when standing erect, or the veins of the hand when one's arm is raised), but the arteries also collapse when subjected to high external pressure. The airways of the lung are known to collapse during a cough and in the manoeuvre of forced expiration common to tests of pulmonary function. Similar phenomena are thought to occur in the urethra during micturition by reason of elastic constrictions due to tissue pressure (Griffiths 1969, 1971*a*, 1973). Several other physiological examples of steady or quasi-steady collapsible-tube flows exist, as well as many that occur in diagnostic and therapeutic devices (Shapiro 1977*a*).

Recently, steady and quasi-steady flows in collapsible tubes have become the object of study (Griffiths 1971*a*, *b*; Oates 1975; Shapiro 1977*b*). These investigations have focused primarily on those aspects having to do with the relative magnitudes of the fluid velocity u and the wave speed c, as well as on transitions between sub- and supercritical flow ($u < c$ and $u > c$, respectively). Since the equations governing steady flow in collapsible tubes closely resemble those for either free surface flow or compressible fluid flow in a duct of varying cross-sectional area, these studies parallel closely the well-known methods developed for gasdynamics and free-surface flows (e.g. Shapiro & Hawthorne 1947).

1.3. *Objectives*

The theoretical and experimental studies to be described were initially motivated by the desire to understand better, and to improve upon, a non-invasive, fluid-mechanical method for preventing deep vein thrombosis, i.e. clotting, with its attendant risk of pulmonary embolism, in patients during and after surgery (Collins 1976; Roberts & Cotton 1975). In this technique, currently under clinical trial, the legs are intermittently compressed by pressurization of double-walled boots extending to the knees; the veins are thereby periodically collapsed and venous stasis is prevented.

However, the understanding of similar unsteady flows is significant to many other physiological phenomena and clinical devices, among which are: (*a*) flow through the lung airways during either a cough (Ross, Gramiak & Rahn 1955; Mead *et al.* 1967) or a forced expiration (Macklem & Mead 1967); (*b*) regulation of cardiac output by collapse of the venae cavae (Wexler *et al.* 1968; Guyton, Langston & Carrier 1962); (*c*) unsteady effects on the venous flow returning to the heart, produced by contractions of the right atrium and by respiratory waves (Wexler *et al.* 1968; Brawley *et al.* 1966); (*d*) unsteady flows produced by high accelerations from collisional impact (Kivity & Collins 1974); (*e*) the method of intra-aortic balloon pumping for temporary cardiac assist now coming into widespread use (Kantrowitz 1968; McMahon *et al.* 1971); (*f*) the method of external cardiac assist employing intermittent external compression of the arteries of the lower extremities (Soroff *et al.* 1969); (*g*) the cardio-ballistic method of external cardiac assist, using an oscillating table (Arnitzenius *et al.* 1970); (*h*) prosthetic heart pumps that use collapsing bladders (Weissman & Mockros, 1967).

The objective of the paper, then, is to develop by theory and experiment, and in a quite general fashion, an understanding of *unsteady flows in collapsible tubes* when subjected to *external pressure or body forces*. Although the theory is one-dimensional, it is otherwise quite general in that it allows for friction, for spatial gradients in the resting cross-sectional area and vessel stiffness, and for temporal and spatial gradients in external pressure and in body force per unit volume. It can approximate flows in a branching system of vessels and accepts any constitutive expression or 'tube law' relating transmural pressure to local cross-sectional area.

1.4. *Structure of the paper*

The paper is divided into three interconnected parts, preceded by a formulation of the one-dimensional theory and a discussion of certain concepts peculiar to collapsible-tube flows. Part 1 deals with the linearized theory for small-amplitude phenomena; this introduces in a simple manner many of the phenomena later demonstrated by the nonlinear theory of part 2. The latter deals in addition with the powerful nonlinear phenomena produced by the peculiar 'equation of state' (i.e. the tube law) of collapsible tubes. Part 3 presents results for some simple experiments, compares the experimental data with numerical simulations, and interprets these in the context of parts 1 and 2.

Although the experiment of part 3, and many of the examples of parts 1 and 2, refer specifically to the collapse of a tube by external pressure, the methods as well as many of the particular results are of general applicability to unsteady flows in collapsible tubes.

2. Formulation of the one-dimensional theory

2.1. *Description and assumptions of the model*

We consider unsteady flows in relatively long, compliant tubes. Longitudinal non-uniformities in the tube are represented by the gradients of neutral area A_0 (corresponding to zero transmural pressure), and by the gradient of circumferential bending, K_p; the latter is inversely proportional to the local compliance when the tube is partially collapsed.

Incompressible fluid. In cases of practical interest, the fluid is either a liquid or a gas flowing at low Mach number. Accordingly, the compliance of the system is essentially that of the tube itself. The fluid is therefore assumed to be incompressible.

One-dimensionality. The longitudinal gradient of area, $(1/A)(\partial A/\partial x)$, is assumed to be small compared with unity. This implies that the characteristic wavelength of area variation is large compared with the tube diameter. The equations of continuity and of motion then indicate that the transverse variation in pressure over any cross-section is negligibly small. Therefore the flow is treated as quasi-one-dimensional in terms of a uniform pressure $p(x,t)$ and a uniform speed $u(x,t)$ over each cross-section.

Quasi-static tube law. The long-wavelength assumption has two further consequences concerning the mechanics of the tube: (*a*) the inertia of the tube wall is negligible; and (*b*), as discussed later, the effects of longitudinal tension in the tube wall are negligible. We assume in addition that the tube material exhibits no visco-elastic effects. All this makes it possible to employ, for the so-called 'tube law' (i.e. the relationship between the cross-sectional area A and the transmural pressure difference $p-p_e$), data determined experimentally with very long tubes under static conditions.

2.2. *Governing equations*

Continuity. Conservation of mass for an incompressible fluid requires that

$$\frac{\partial}{\partial x}(uA)+\frac{\partial A}{\partial t}=q_L, \tag{1}$$

where x and t denote distance and time, respectively, and q_L is the volume flow rate per unit length entering the tube from tributaries.

Momentum. Taking account of wall friction by means of a wall shear stress τ_w opposing the flow, and assuming that the added flow q_L enters with a component of velocity u_{Lx} along x (note that, if $q_L < 0$, then $u_{Lx} = u$), the dynamical equation may be written as

$$\frac{\partial u}{\partial t}+u\frac{\partial u}{\partial x}+\frac{1}{\rho}\frac{\partial}{\partial x}(p-p_e)+\frac{1}{\rho}\frac{\partial p_e}{\partial x}-G_x+\frac{4}{D_e}\frac{\tau_w}{\rho}+\frac{q_L(u-u_{Lx})}{A}=0, \tag{2}$$

where G_x is the x component of all body forces per unit mass (including gravity as well as d'Alembert forces associated with an accelerating reference frame), and D_e is the hydraulic diameter.

It is evident that body forces, friction, and the momentum deficiency of inflow from tributaries, all produce dynamical effects similar to those generated by an external

pressure gradient. For instance, accelerations resulting from collisional impact or blows are equivalent to a linear variation of external pressure.

Tube law. For a long tube with properties that change only slowly in the x direction, the variables p and A that appear in the continuity and momentum equations are connected by an 'equation of state' of the implicit form

$$\mathscr{P} = \mathscr{P}(\alpha), \tag{3}$$

where $\mathscr{P} \equiv (p-p_e)/K_p$ and $\alpha \equiv A/A_0$. At any location x, the phase velocity c of long area waves is governed by the inertia of the fluid and the compliance of the tube through the formula

$$c^2(\alpha; x) = \frac{A}{\rho}\left[\frac{\partial(p-p_e)}{\partial A}\right]_x = \frac{K_p(x)}{\rho}\alpha\frac{d\mathscr{P}}{d\alpha}; \quad c_0^2(x) = \frac{K_p(x)}{\rho}\left(\frac{d\mathscr{P}}{d\alpha}\right)_{\alpha=1}, \tag{4}$$

where c_0 is the value at the neutral area, $\alpha = 1$.

In passing, we note that when the wavelength-to-diameter ratio cannot be assumed as infinitely large, forms other than equation (3) must be used to account for effects due to axial tension, wall inertia and radial motion of the fluid. Such forms involve derivatives of α with respect to time (related to wall inertia) or distance (related to axial tension or bending) and give rise to wave speed dispersion not accounted for in (4).

Normalized equations. We introduce the normalized variables

$$\xi \equiv x/L, \quad \tau \equiv c_0^* t/L, \quad \mathscr{U} \equiv u/c_0^*, \quad \mathscr{C}(\alpha;\xi) \equiv c/c_0(\xi),$$

$$C_f \equiv \frac{\tau_w}{\frac{1}{2}\rho u^2}, \quad P \equiv \frac{p-p_e}{\rho c_0^2}, \quad P_e \equiv \frac{1}{c_0^{*2}}\left[\frac{p_e}{\rho} - \int G_x L\,d\xi + \int \frac{q_L(u-u_{Lx})\,L}{A}\,d\xi\right], \tag{5}$$

where L is an appropriate characteristic length, and c_0^* is the value of c_0 at some reference location ξ^*. Inserting these into (1) and (2), and substituting for the term $\partial(p-p_e)/\partial x$ by means of (3) and (4), we obtain

$$\frac{\partial}{\partial\xi}(\mathscr{U}\alpha) + \frac{\partial\alpha}{\partial\tau} + \mathscr{U}\alpha\cdot\frac{1}{A_0}\frac{dA_0}{d\xi} = \frac{Lq_L}{c_0^* A_0} \tag{6}$$

and

$$\frac{\partial\mathscr{U}}{\partial\tau} + \mathscr{U}\frac{\partial\mathscr{U}}{\partial\xi} + \left(\frac{K_p}{K_p^*}\right)\mathscr{C}^2\frac{1}{\alpha}\frac{\partial\alpha}{\partial\xi} + \frac{\mathscr{P}}{\rho c_0^{*2}}\frac{dK_p}{d\xi} = -\frac{\partial P_e}{\partial\xi} - 2\mathscr{U}^2\frac{L}{D_e}C_f, \tag{7}$$

where K_p^* is the value of K_p at ξ^*.

2.3. *The tube law*

Figure 1 shows the curve $\mathscr{P}(\alpha)$ as determined by static observations of transmural pressure difference *versus* volume on long lengths of thin-walled latex tubing of the type used in the experiments described in part 3. In determining $\mathscr{P}(\alpha)$, care was taken to eliminate errors introduced at the end regions where the compliant tube was attached to rigid tubes.

Also shown on figure 1 are several related functions later found to be useful. The curves shown are more or less typical of those for thin-walled compliant tubes, although in the range $\alpha \cong 1$ the curves are highly dependent upon the initial out-of-roundness of the tube.

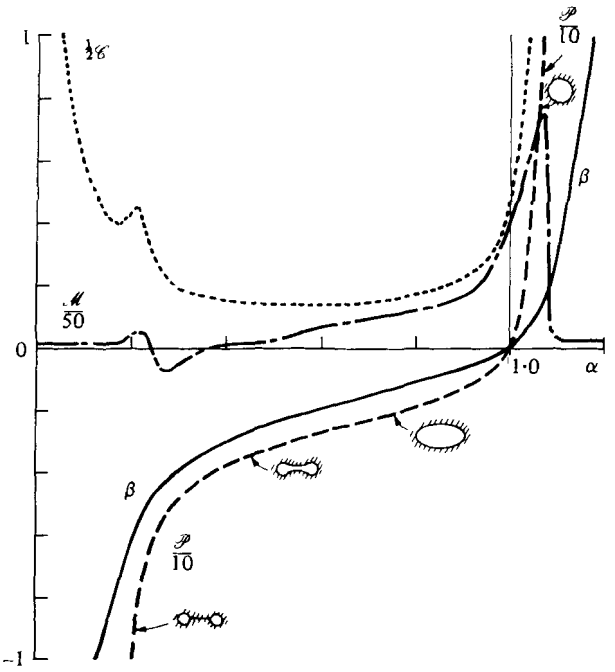

FIGURE 1. Properties of commercial Penrose surgical drain tubing made of latex rubber (diameter, 1·27 cm; nominal wall thickness, 0·032 cm; Young's modulus $\cong 1{\cdot}6 \times 10^7$ dynes cm^{-2}; $c_0 \cong 86$ cm s^{-1}). The wall thickness varied linearly, end to end, from 0·028 cm to 0·036 cm. The functions $\mathscr{C}(\alpha)$, $\beta(\alpha)$ and $\mathscr{M}(\alpha)$ are determined from the experimental curve $\mathscr{P}(\alpha)$ by means of (4), (57) and (59).

Positive transmural pressure difference. When $\mathscr{P} > 0$ the tube is inflated and essentially round. The pressure difference across the wall is supported by hoop tension and the appropriate stiffness constant is that for tension in the tube wall.

Negative transmural pressure difference. When $\mathscr{P} < 0$, the tube is partially collapsed, in the successive shapes shown in figure 1. The pressure difference is supported primarily by the bending stiffness of the tube wall, which, for a linear elastic material, is of the form $K_p \propto EI$, where E is Young's modulus; and I is the bending moment. For a slice of the tube, $I = (h/R_0)^3/(1-\nu^2)$, where h is the wall thickness, R_0 is the radius corresponding to A_0, and ν is Poisson's ratio.

The similarity range. In the range of α below about $\frac{1}{4}$ (0·21 for a perfectly symmetrical, elastic tube, as shown by Flaherty, Keller & Rubinow, 1972) the walls of the tube are in line contact, and two parallel conduits are formed, the shapes of which are self-similar. Self-similarity arguments show that the tube law is then of the form $\mathscr{P} = -\alpha^{\frac{3}{2}}$, a result confirmed by our own experiments.

Effect of longitudinal tension. When the tube is under a longitudinal tension T_L, and there is a local curvature of order R_L^{-1} in the longitudinal plane, the quasi-static tube law no longer holds. Mechanically, the effect of T_L is roughly equivalent to that due to a change in p_e by an amount of order T_L/R_L.

Throughout this paper we assume that $(T_L/R_L) \ll (p - p_e)$ thus rendering the tube law of equation (3) and figure 1 a good approximation. Similarly, we also ignore longitudinal bending stiffness. These assumptions, we note, may involve significant

errors in such cases as (*a*) regions where p_e changes rapidly with distance, (*b*) in the neighbourhood of shock-like transitions (see § 13) and (*c*) near attachment points where the area is constrained to adjust in a short distance to match the area of a rigid end tube. As suggested earlier, the structural mechanics of the tube then enters the problem in a much more complex manner than through the simple description of equation (3).

2.4. *Analogues*

The governing laws, (6) and (7), are similar to those of gas dynamics or free-surface flow, with the tube cross-sectional area corresponding to the gas density or the liquid depth, respectively. The tube law plays the role of an equation of state which, in the analogues, connects the pressure to the density or depth. However, in the range $\alpha < 1$, the nonlinearities brought in by the tube law are much more severe than those in the respective equations of state for gas dynamics or free-surface flow.

In gas-dynamical flows, the term $\partial P_e/\partial \xi$ would arise from inflow or outflow from tributaries and from body forces; in the latter category only electromagnetic forces in plasmas would normally be significant.

Free-surface flows offer perhaps a closer analogue, since the term $\partial P_e/\partial \xi$ would represent the effects of a sloping bottom.

Part 1. Linearized theory for small amplitudes

3. Formulation of small-amplitude theory

While most problems of interest in the range $\alpha < 1$ exhibit considerable nonlinear behaviour, there are some in which the amplitudes are sufficiently small for a linearized theory to be of value.

More importantly, however, the linearized theory is a highly useful preliminary to nonlinear calculations. It describes accurately the early stages of an evolving nonlinear flow. It anticipates many features of the more complex nonlinear flow, and provides insights and interpretations difficult to extract from purely numerical calculations of nonlinear behaviour.

3.1. *Assumptions*

In part 1 of the paper we neglect altogether friction, longitudinal inhomogeneities in tube properties, and inflow from tributaries: thus C_f, dK_p/dx, dA_0/dx and q_L are all zero. Attention is thus focused on the flow and changes of area produced by the pressurization function $P_e(\xi, \tau)$.

3.2. *The linearized equations*

We introduce the definitions

$$\mathscr{U} = \overline{\mathscr{U}} + v, \quad \alpha = \bar{\alpha} + a, \quad \mathscr{C} = 1 + \gamma, \quad P \equiv \bar{P} + \hat{P}, \quad P_e \equiv \bar{P}_e + \hat{P}_e, \tag{8}$$

where $\overline{\mathscr{U}}$, $\bar{\alpha}$, $\bar{P}$ and $\bar{P}_e$ refer to an undisturbed uniform state, and where v, a, γ, $\hat{P}$ and $\hat{P}_e$ represent the dimensionless perturbations in velocity, area, etc. The constant reference wave speed $c_0 = c_0^*$ that appears in (5) should now be taken as the value of $\bar{c}$ corresponding to the area ratio $\bar{\alpha}$. We also transform to a reference frame ξ' which moves with the unperturbed speed $\overline{\mathscr{U}}$, by means of the relationship $\xi' = \xi - \overline{\mathscr{U}}\tau$.

Examination of (3), (4), (6) and (7) shows that v, a, γ, $\hat{P}$ and $\hat{P}_e$ are all of the same order. This is evident physically because it is the perturbation pressure $\hat{P}_e$ that pro-

duces the perturbations in velocity and area. We assume that all are small compared with unity. To the order of this approximation, the perturbation flow rate, made dimensionless with reference to $c_0 A_0$, is equal to v.

The foregoing are now introduced into (3), (4), (6) and (7). Neglecting all but first-order terms in the perturbation quantities, one obtains the linearized equations for the perturbation speed v and perturbation area a.

Continuity: $$a_\tau + v_{\xi'} = 0. \tag{9}$$

Momentum: $$a_{\xi'} + v_\tau = -\hat{P}_{e,\xi'}. \tag{10}$$

Tube law: $$\hat{P} = a/\bar{\alpha}. \tag{11}$$

Cross-differentiation of (9) and (10) produces

$$a_{\tau\tau} - a_{\xi'\xi'} = \hat{P}_{e,\xi'\xi'} \tag{12}$$

and $$v_{\tau\tau} - v_{\xi'\xi'} = -\hat{P}_{e,\xi'\tau}. \tag{13}$$

Henceforth we shall drop the primes, writing ξ instead of ξ', with the understanding that we are then observing the flow in a reference frame moving with the mean fluid speed $\bar{u}$.

The homogeneous forms of (12) and (13), with terms in $\hat{P}_e$ absent, are seen to be the wave equation for plane waves. Their solutions have a well-known physical interpretation: waves of velocity and area propagate with unchanged strength at the dimensionless speed ± 1 relative to the fluid; furthermore, waves are generated only at the boundaries, do not interact with each other, and combine linearly. The terms $\hat{P}_{e,\xi\xi}$ and $-\hat{P}_{e,\xi\tau}$ may be interpreted as *sources* of waves in the region between the boundaries.

4. Solution by a linear method of characteristics

The linearized equations derived above can be solved either by the use of Green's functions (Morse & Ingard 1968) or by the linear method of characteristics. For continuity with later discussions in part 2, the characteristics method will be used.

From (9) and (10), the 'state characteristics' defined by

$$(dv/da)_{\mathscr{R},\mathscr{L}} = \mp 1 - \hat{P}_{e,\xi}(d\tau/da) \tag{14}$$

apply along the 'physical characteristics' defined by

$$(d\xi/d\tau)_{\mathscr{R},\mathscr{L}} = \pm 1. \tag{15}$$

The latter represent the wave trajectories in (ξ, τ) space. Here the symbol $\mathscr{R}$ denotes the rightward- and $\mathscr{L}$ the leftward-running wave path; they correspond respectively to the upper and lower signs in the two equations.

The integrated forms of (14) can be added and subtracted to obtain expressions for the perturbation area and velocity:

$$a = \tfrac{1}{2}(v_{0,\mathscr{R}} - v_{0,\mathscr{L}}) + \tfrac{1}{2}(a_{0,\mathscr{R}} + a_{0,\mathscr{L}}) + \tfrac{1}{2}(\mathbb{P}_{\mathscr{L}} - \mathbb{P}_{\mathscr{R}}); \tag{16a}$$

$$v = \tfrac{1}{2}(v_{0,\mathscr{R}} + v_{0,\mathscr{L}}) + \tfrac{1}{2}(a_{0,\mathscr{R}} - a_{0,\mathscr{L}}) - \tfrac{1}{2}(\mathbb{P}_{\mathscr{R}} + \mathbb{P}_{\mathscr{L}}); \tag{16b}$$

$$\mathbb{P}_{\mathscr{R},\mathscr{L}} \equiv \int_0^\tau \hat{P}_{e,\xi}\, d\tau_{\mathscr{R},\mathscr{L}}; \tag{16c}$$

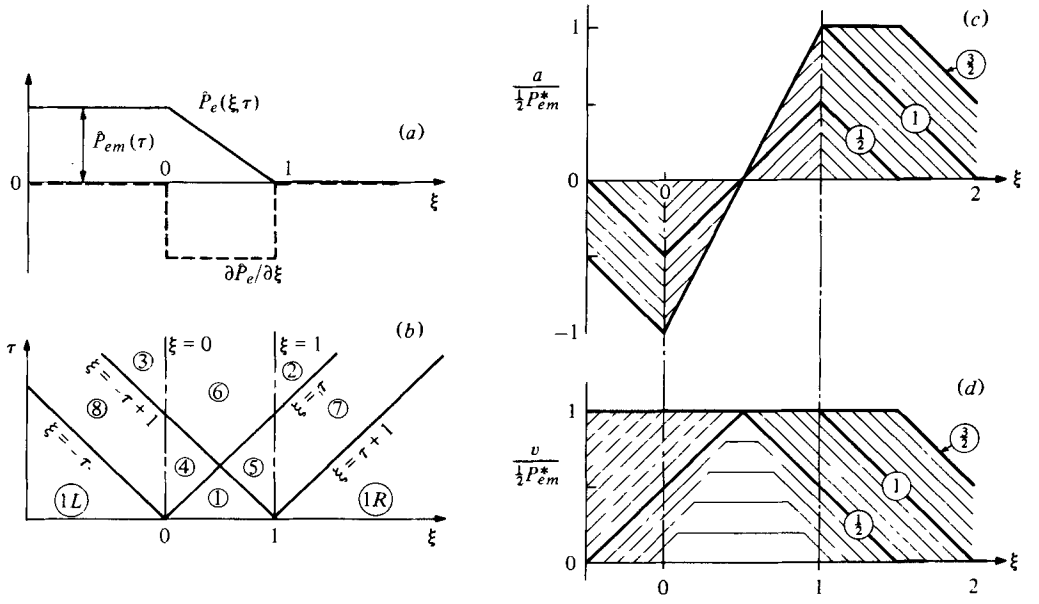

FIGURE 2. Application of a linear pressure ramp to a long tube. (*a*) Distributions of $\hat{P}_e$ and $\partial\hat{P}_e/\partial\xi$. (*b*) Zones in $(\xi;\tau)$ space. (*c*), (*d*) Distributions of $a(\xi;\tau)$ and $v(\xi;\tau)$ for a constant ramp height. Numbers on curves are values of τ.

where v_0 and a_0 represent values of v and a at $\tau = 0$ pertaining to the initial locations of the indicated physical characteristics. In the several examples to which (16) are applied, it is assumed that v_0 and a_0 are everywhere zero.

4.1. *A time-varying linear ramp in* $\hat{P}_e$

Consider a linear ramp in $\hat{P}_e(\xi,\tau)$ of the form shown in figure 2(*a*), extending from $\xi = 0$ to $\xi = 1$, and of time-varying amplitude $\hat{P}_{em}(\tau)$. This is of practical interest as an approximation to the edge regions of pressurization cuffs applied to vessels such as veins or arteries. It also models a segment of a vessel subjected to longitudinal acceleration due to collision or impact.

The integrands in (16) are non-zero only while the relevant characteristic curve passes through the ramp region. At any instant of time, $\hat{P}_{e,\xi}$ has a constant value, $-\hat{P}_{em}(\tau)$, throughout the ramp. The integrals are then easily evaluated and the solution is conveniently represented in terms of a pressure impulse integral:

$$\Pi(z) \equiv \int_0^z \hat{P}_{em}(\tau)\,d\tau. \tag{17}$$

Table 1 presents the area, $a(\xi,\tau)$, and velocity, $v(\xi,\tau)$, for the various zones in (ξ,τ) space identified in figure 2(*b*).

A ramp constant in time. Now consider the case where a *constant* external pressure $\hat{P}^*_{em}$ is applied instantaneously. Equation (17) gives $\Pi(z) = \hat{P}^*_{em}.z$. The solution is then very simple: for example, using table 1, $a_6 = \frac{1}{2}\hat{P}^*_{em}(2\xi - 1)$, and $v_6 = \frac{1}{2}\hat{P}^*_{em}$.

Figures 2(*c*) and 2(*d*) show how the profiles $a(\xi)$ and $v(\xi)$ evolve at successive times τ. In zone 1, which extends to a maximum τ of $\frac{1}{2}$, the area remains unchanged and the velocity depends only on time (true also for the general case, see table 1). Compression

Zone	$2a$	$2v$
1	0	$2\Pi(\tau)$
$1R$	0	0
$1L$	0	0
7	$\Pi(\tau-\xi+1)$	$\Pi(\tau-\xi+1)$
8	$-\Pi(\tau+\xi)$	$\Pi(\tau+\xi)$
4	$-\Pi(\tau-\xi)$	$-\Pi(\tau-\xi)+2\Pi(\tau)$
5	$\Pi(\tau+\xi-1)$	$-\Pi(\tau+\xi-1)+2\Pi(\tau)$
6	$-\Pi(\tau-\xi)+\Pi(\tau+\xi-1)$	$-\Pi(\tau-\xi)-\Pi(\tau+\xi-1)+2\Pi(\tau)$
2	$-\Pi(\tau-\xi)+\Pi(\tau-\xi+1)$	$-\Pi(\tau-\xi)+\Pi(\tau-\xi+1)$
3	$-\Pi(\tau+\xi)+\Pi(\tau+\xi-1)$	$\Pi(\tau+\xi)-\Pi(\tau+\xi-1)$

TABLE 1. Solution for linear ramp of figure 2. $\Pi(z) \equiv \int_0^z \hat{P}_{em}(\tau)\, d\tau$.

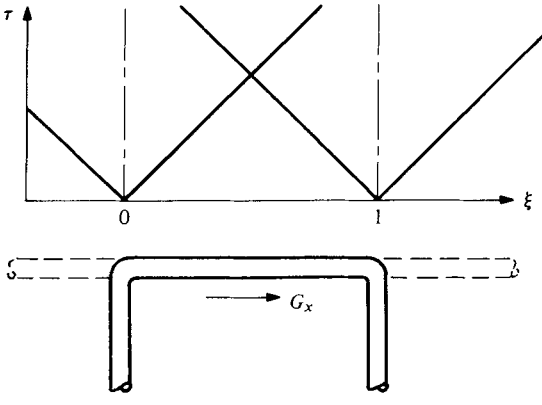

FIGURE 3. Rapid leftwards acceleration of a U-shaped vessel, giving rise to body force G_x. The dashed lines show the vessel unfolded along ξ.

waves proceed downstream and rarefaction waves upstream. Both sets of waves increase the velocity. However, when coupled with the spatial distribution of $\hat{P}_e$, the compression and rarefaction waves create an area bulge which appears to proceed in both directions from $\xi = 1$ and an area contraction which appears to proceed in both directions from $\xi = 0$. The physical behaviour is further clarified in connexion with figure 10.

Two further observations of practical importance deserve mention. First, for $\tau > 1$, no further changes of area or velocity occur within the pressurized zone, $0 < \xi < 1$; that is, the tube then behaves like a rigid, tapered duct within which the perturbation velocity is constant with respect to both ξ and τ. Fluid is transferred through this segment of tube from the steadily lengthening collapsed zone, $\xi < 0$, to the steadily lengthening inflated zone, $\xi > 0$. Second, a minimum area is formed at $\xi = 0$; when friction and flow separation are considered, it is evident that this reduces the rate at which the pressurized portion of the tube can be emptied.

Flow created by acceleration during impact. Consider a U-shaped segment of a long compliant tube (figure 3) that is rapidly brought to rest from an initial speed V_i along ξ. This approximates what happens during an impacting blow or a collision.

Zone	$\frac{a}{V_i/c_0}$	$\frac{v}{V_i/c_0}$
1	0	1
$1R$	0	0
$1L$	0	0
7	$\frac{1}{2}$	$\frac{1}{2}$
8	$-\frac{1}{2}$	$\frac{1}{2}$
4	$-\frac{1}{2}$	$\frac{1}{2}$
5	$\frac{1}{2}$	$\frac{1}{2}$
6	0	0
2	0	0
3	0	0

TABLE 2

In a reference frame moving with the tube, a d'Alembert force $G_x(\tau)$ acts along ξ. Referring to (5), it is seen that $G_x(\tau)$ is equivalent to a distribution of $\hat{P}_e$ exactly like that of figure 2(*a*) and that the solution of table 1 is applicable.

Inasmuch as the wave speed of compliant tubes is quite low, it is likely that the total time period during which G_x acts is small compared with the characteristic time $\Delta\tau = 1$ for one wave passage over the distance $\Delta\xi = 1$. Accordingly, we assume that the body force $G_x(\tau)$ may be represented as a delta function at $\tau = 0$. By equation (17), then, $\Pi(z)$ is a step function which is zero for $\tau < 0$ and which, for $\tau \geqslant 0$, has the value

$$\Pi(z) = \Pi^* = \int_0^z (G_x L/c_0^2)\, d\tau = V_i/c_0.$$

Now, with this constant value for $\Pi(z)$, the formulas in table 1 yield the results shown in table 2.

Uniform increases of area and velocity propagate rightwards in the band 1, 5, 7; a uniform decrease of area and a uniform increase of velocity propagate leftwards in the band 1, 4, 8. In zone 1, the velocity disturbances reinforce but the area disturbances cancel. The net effects on a and v are zero in zones 2, 3 and 6. The rightwards and leftwards disturbances in bands 7 and 8 continue to propagate unchanged except as ultimately dissipated by friction and distorted by reflexions.

4.2. *A time-varying spatial step in* $\hat{P}_e$

By considering the limit of the solution for the linear ramp of figure 2(*a*), as the ramp length L goes to zero, one obtains the solution for a spatial time-varying step in $\hat{P}_e$ at $\xi = 0$, shown in figure 4(*a*). Referring to figure 2(*b*), the variables ξ and τ become very large compared with unity as $L \to 0$. Zones 1, 4, 5, 6, 7 and 8 in effect shrink to infinitesimal size, leaving only zones $1R$, $1L$, 2 and 3, as in figure 4(*b*).

Inspection of the definite integral of (17), for the circumstances where $|\xi| \gg 1$ and $\tau \gg 1$, shows that the expressions in table 1 for zones 2 and 3 reduce to the limiting forms

$$v_2 = v_3 = a_2 = -a_3 = \tfrac{1}{2}\hat{P}_{em}(\tau - |\xi|). \tag{18}$$

Suppose, for instance, that the amplitude $\hat{P}_{em}(\tau)$ of the step increases with time as shown in figure 5(*a*), reaching the constant value $\hat{P}_{em}^*$ at the time τ^*. Then, according to (18), the area and velocity distributions at a time $\tau > \tau^*$ will be as shown in figure 5(*b*); the curves are replicas of the $\hat{P}_{em}(\tau)$ curve of figure 5(*a*).

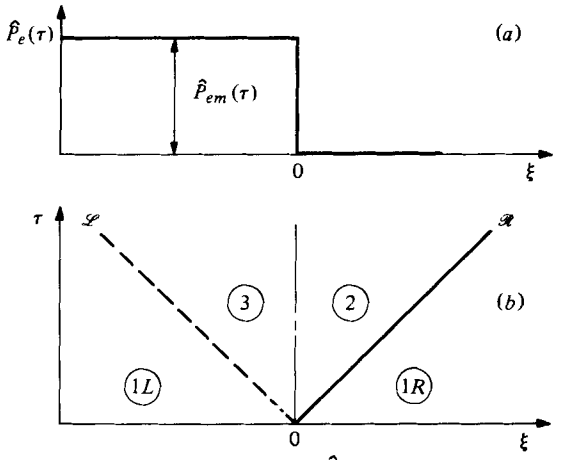

FIGURE 4. A time-varying step in $\hat{P}_e$ at $\xi = 0$. (*a*) Instantaneous distribution $\hat{P}_{em}(\xi;\tau)$. (*b*) Wave diagram.

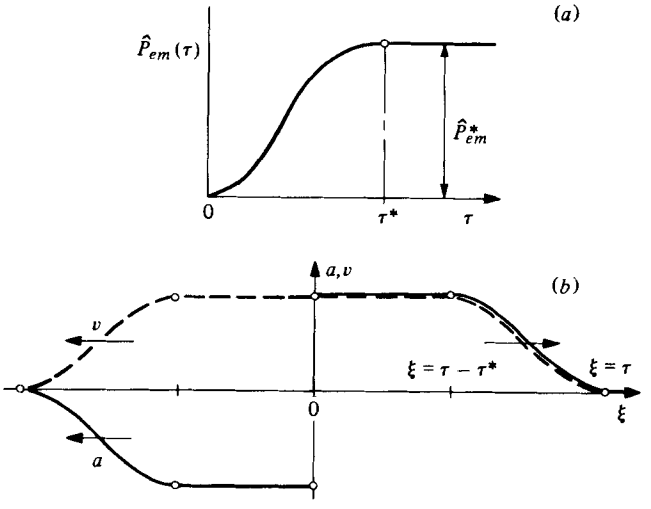

FIGURE 5. (*a*) An S-ramp in $\hat{P}_{em}(\tau)$, with maximum value $\hat{P}^*_{em}$ and rise time τ^*. (*b*) Corresponding distributions of $a(\xi,\tau)$ and $v(\xi;\tau)$.

A constant step in $\hat{P}_e$, instantaneously applied. Let $\tau^* \to 0$ in figure 5(*a*), so that figure 4 now refers to a constant increment $\hat{P}^*_{em}$ that is instantaneously applied in the region $\xi < 0$. Then figure 5(*b*) takes the form of figure 6(*a*). The latter, together with (18), reveals that the fluid states are respectively constant in zones 2 and 3 of figure 4(*b*). Thus the lines $\xi = \pm\tau$ may be identified as physical waves ($\mathscr{R}$ for rightwards, $\mathscr{L}$ for leftwards), generated by the step pulse of pressure, carrying signals the amplitudes of which are given by

$$\left.\begin{aligned} \Delta v_{\mathscr{R}} &= \Delta v_{\mathscr{L}} \\ \Delta\alpha_{\mathscr{R}} &= -\Delta\alpha_{\mathscr{L}} \\ \Delta\hat{P}_{\mathscr{R}} &= -\Delta\hat{P}_{\mathscr{L}} \end{aligned}\right\} = \tfrac{1}{2}\hat{P}^*_{em}, \tag{19}$$

where $\Delta v_{\mathscr{R}} = v_2 - v_{1\mathscr{R}}$, etc. After the $\mathscr{R}$ and $\mathscr{L}$ waves are generated, the velocity and pressure are continuous across the step, but the area is discontinuous, as seen in figure 6(*a*).

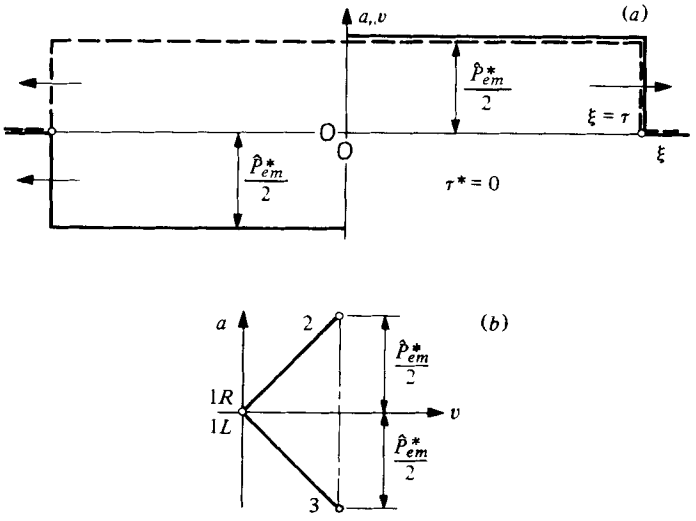

FIGURE 6. (*a*) Distributions of $a(\xi, \tau)$ and $v(\xi; \tau)$ for a step of constant amplitude, i.e. τ^* in figure 5 equal to 0. (*b*) State diagram corresponding to (*a*).

The changes produced by such a unit pulse are conveniently represented in graphic form on a (v, a) 'state plane', as in figure 6(*b*).

In § 8, a generalization of (19) is derived for the case where the step change in $\hat{P}_e(\xi)$ is at a fixed location but the mean speed $\overline{\mathscr{U}}$ relative to the step is not negligible compared with unity.

4.3. *A uniformly growing linear ramp*

Consider a tube, closed at $\xi = 0$, to which is applied a linear ramp of constant slope $(-\partial\hat{P}_e/\partial\xi)$ which proceeds outward from the origin at a constant rate (figure 7*a*). At time τ, the leading edge of the ramp is at $\xi = V_r\tau$, where V_r is the dimensionless ramp speed. To meet the condition that $v = 0$ at $\xi = 0$, an image ramp is applied in the region $\xi < 0$.

The physical situation described may be established experimentally in a vertical apparatus in which the compliant tube, closed at the upper end, is surrounded by a chamber containing the same liquid. If the fluid level in the outer chamber is lowered at a constant rate, the distribution $\hat{P}_e(\xi, \tau)$ of figure 7(*a*) will be established.

(*a*) $V_r < 1$. The integrand of (16*c*) is zero for $|\xi| > V_r\tau$, and has the constant values $+\hat{P}_{e,\xi}$ and $-\hat{P}_{e,\xi}$ for $0 < \xi < V_r\tau$ and $-V_r\tau < \xi < 0$, respectively. For an arbitrary point in region *e*–*f* of figure 7(*b*), application of (16*a*, *b*) produces

$$a_{ef} = v_{ef} = \tfrac{1}{2}\hat{P}_{e,\xi}(2\tau_2 - \tau_1 - \tau_3).$$

Geometry gives us the values of τ_1, τ_2, and τ_3 to yield

$$a_{ef} = v_{ef} = \hat{P}_{e,\xi}\frac{V_r^2}{1-V_r^2}(\xi - \tau). \tag{20}$$

Similarly,

$$a_{fg} = \frac{\hat{P}_{e,\xi}}{2}(2\tau_5 - \tau_6 - \tau_4) = \hat{P}_{e,\xi}\left(\frac{V_r\tau}{1+V_r} - \xi\right) \tag{21a}$$

and

$$v_{fg} = -\frac{\hat{P}_{e,\xi}}{2}(2\tau - 2\tau_5 - \tau_6 + \tau_4) = -\hat{P}_{e,\xi}\frac{V_r}{1+V_r}\xi. \tag{21b}$$

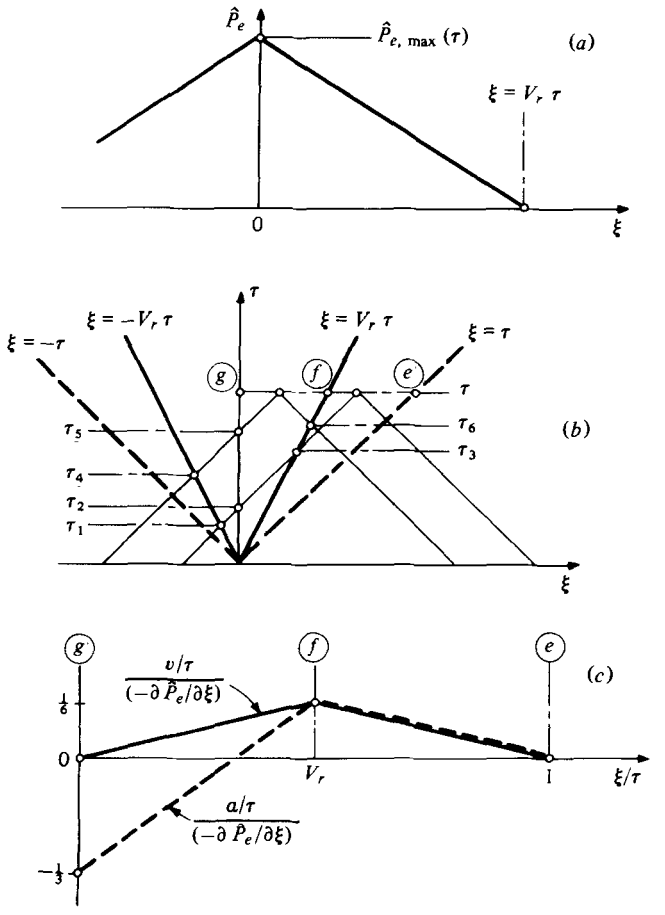

FIGURE 7. A uniformly growing linear ramp, for $V_r < 1$. (*a*) Applied pressure distribution. (*b*) Wave diagram. (*c*) Area and velocity distributions for $V_r = \frac{1}{2}$.

The spatial distributions of a and v are shown in figure 7 (*c*) for the case $V_r = \frac{1}{2}$. We note that there is no area throat near the downstream end of the pressurized region, such as appeared in figure 2. As contrasted with the latter, the tube of figure 7 empties first at the upstream end rather than at the downstream end, in a sort of milking action, which indeed this moving pressure ramp simulates.

(*b*) $V_r > 1$. Figure 8 shows results similarly obtained for the case $V_r > 1$, where the moving ramp outruns the pressure waves. The corresponding formulas are:

$$a_{ef} = \hat{P}_{e,\xi}\frac{V_r\tau - \xi}{1 - V_r^2}; \quad v_{ef} = \hat{P}_{e,\xi}\frac{V_r(V_r\tau - \xi)}{1 - V_r^2}; \tag{22a}$$

$$a_{fg} = \hat{P}_{e,\xi}\left(\frac{V_r\tau}{1+V_r} - \xi\right); \quad v_{fg} = -\hat{P}_{e,\xi}\frac{V_r}{1+V_r}\xi. \tag{22b}$$

Perhaps surprisingly, the two cases $V_r < 1$ and $V_r > 1$ produce quite similar results.

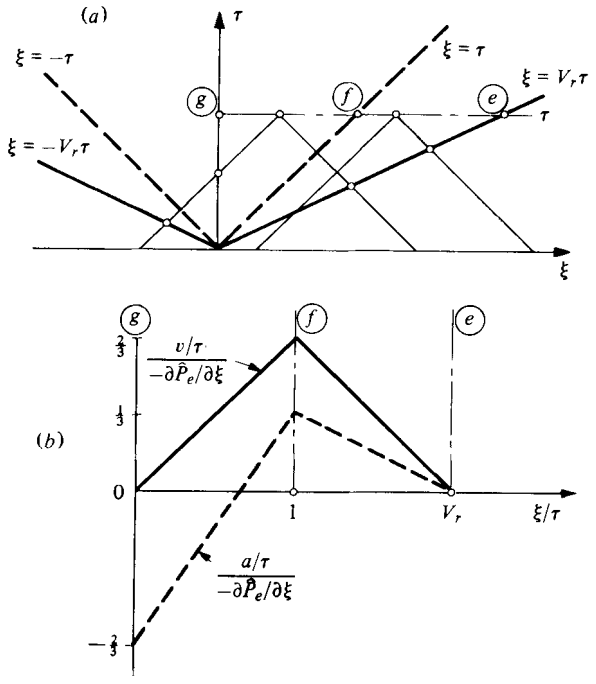

FIGURE 8. Similar to figure 7, but for $V_r > 1$. (*a*) Wave diagram. (*b*) Area and velocity distributions for $V_r = 2$.

4.4. *A rectangular 'milking wave' of constant pressure*

Figure 9(*a*) shows a uniformly widening rectangular distribution of constant applied pressure, $\hat{P}_e^*$, the leading edge of which moves with the dimensionless speed V_r. The effect of a closed end is represented by means of the image distribution for $\xi < 0$.

To evaluate the integral of (16*c*), we first define a new variable, $\eta = V_r\tau \mp \xi$; the upper sign applies in the region $\xi > 0$ and the lower sign in the region $\xi < 0$. Since η defines the trajectories of the progressing pressure fronts, $\hat{P}_e$ is a function of η alone and the integrand of (16*c*) can be written as

$$\frac{\partial \hat{P}_e}{\partial \xi} = \frac{d\hat{P}_e}{d\eta}\frac{\partial \eta}{\partial \xi} = \begin{cases} -\dfrac{d\hat{P}_e}{d\eta} & \text{for} \quad \xi > 0, \\ +\dfrac{d\hat{P}_e}{d\eta} & \text{for} \quad \xi < 0. \end{cases}$$

We can also replace $d\tau_{\mathscr{R},\mathscr{L}}$ in the integral using the expressions

$$\left(\frac{d\tau}{d\eta}\right)_{\mathscr{R},\mathscr{L}} = \begin{cases} (V_r \mp 1)^{-1} & \text{for} \quad \xi > 0, \\ (V_r \pm 1)^{-1} & \text{for} \quad \xi < 0. \end{cases}$$

Combining these in the integration of (16*c*) produces the results

$$\int_0^\tau \frac{\partial \hat{P}_e}{\partial \xi} d\tau_{\mathscr{R},\mathscr{L}} = \begin{cases} \Delta\hat{P}_e/(V_r+1) & \text{for} \quad \xi > 0, \\ \Delta\hat{P}_e/(V_r-1) & \text{for} \quad \xi < 0, \end{cases}$$

where $\Delta\hat{P}_e$ is the pressure jump across the discontinuity along the appropriate characteristic curve.

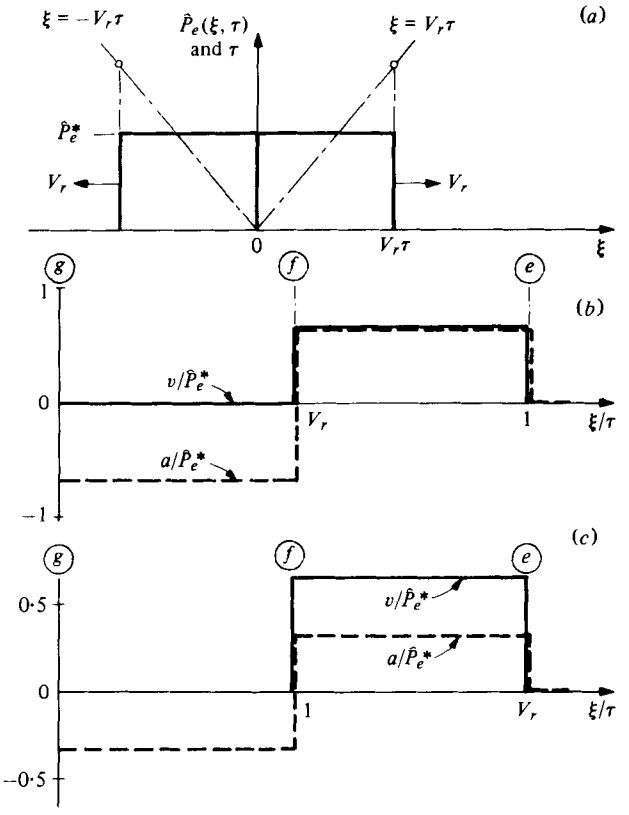

FIGURE 9. A rectangular 'milking wave' of constant pressure applied to a tube with closed end. (*a*) The distribution of applied pressure. The leading edges of the pressurized regions move on trajectories $\xi = \pm V_r\tau$. (*b*) Distributions of area and velocity for $V_r = \frac{1}{2}$. (*c*) Distributions of area and velocity for $V_r = 2$.

(*a*) $V_r < 1$. These integrals yield the solutions given below for area and velocity in the regions identified in figure 7(*b*):

$$a_{ef} = v_{ef} = \hat{P}_e^* \frac{V_r}{1 - V_r^2}; \tag{23a}$$

$$a_{fg} = -\frac{\hat{P}_e^*}{1 + V_r}; \quad v_{fg} = 0. \tag{23b}$$

Area and velocity distributions for $V_r < 1$ are shown in figure 9(*b*). Behind the leading edge of the zone of applied pressure, the fluid is motionless, and the area is uniformly reduced. Ahead of the leading edge, and up to the trajectory $\xi = \tau$ of the first wavelet, the fluid is accelerated to uniform speed and the area is uniformly increased. As the speed of the pressure front approaches the wave speed, the width of the region ahead of the leading edge diminishes; the corresponding amplitudes of a and v become large. We note that the linearized solution is not valid as $V_r \to 1$, so that the formulas are then only indicative of general behaviour.

(*b*) $V_r > 1$. Using the same method as above and referring now to the regions identified in figure 8(*a*), the area and velocity are given by

$$a_{ef} = \frac{\hat{P}_e^*}{V_r^2 - 1}; \quad v_{ef} = \hat{P}_e^* \frac{V_r}{V_r^2 - 1}; \tag{24a}$$

$$a_{fg} = -\frac{\hat{P}_e^*}{1 + V_r}; \quad v_{fg} = 0. \tag{24b}$$

Typical area and velocity distributions for $V_r > 1$ are shown in figure 9(*c*). Again, both a and v tend to infinity at the forward end as $V_r \to 1$. The two cases, $V_r < 1$ and $V_r > 1$, exhibit no remarkable differences.

5. Generation and transmission of waves

Waves may be generated in the usual way at the boundaries, for example by the injection of fluid, by the motion of a piston, by opening a valve to a region of different pressure, or by reflexion of arriving waves. Here, however, we consider the two questions of (*a*) wave generation remote from boundaries, and (*b*) the transmission and reflexion of waves due to spatial gradients of external pressure.

A continuously variable $\hat{P}_e(\xi, \tau)$ may be approximated by piecewise constant intervals of $\hat{P}_e$, with small discrete steps in $\hat{P}_e$ occurring at particular intervals $\Delta\xi$ and $\Delta\tau$. Owing to the linearity of the equations, the solution for the given $\hat{P}_e(\xi, \tau)$ may be obtained by summing the contributions to a and v produced by all the steps. This approach is more than a basis for numerical computations. It also yields illuminating physical insights.

5.1. *Wave generation*

Consider what happens when $\hat{P}_e(\xi)$ changes instantaneously, say, by an elevation of the external pressure. The immediate consequence, before any time elapses, is an accompanying change in the *internal pressure* of precisely the same amount; however, neither $a(\xi)$ nor $v(\xi)$ is at first altered. If the applied $\hat{P}_e(\xi)$ is uniform with ξ, so is the change in the internal pressure; hence no pressure gradient is created, no force acts to accelerate the fluid, and neither the velocity nor area are affected. But if the applied $\hat{P}_e(\xi)$ is non-uniform in ξ, so is the change in internal pressure; now the gradient of the latter produces fluid acceleration, with consequent effects on the velocity and area distributions.

From this physical point of view the *basic mechanism of wave generation* (away from the boundaries) is the term $\hat{P}_{e,\xi\tau}$, that is, a temporal variation of $\hat{P}_e$ that is spatially non-uniform. The unit step of wave generation is evidently the instantaneous pulse shown in figures 4 and 6(*a*) and described by the formulas in (19).

5.2. *Wave transmission and reflexion*

Next consider a wave previously generated that arrives at a location where there is a time-invariant spatial step in $\hat{P}_e$. Since the term $\hat{P}_{e,\xi\tau}$ is zero, (13) reduces to the homogeneous wave equation. Consequently the velocity wave continues through the step with unaltered strength, and with no reflexions.

In (12), on the other hand, the term $\hat{P}_{e,\xi\xi}$ is not only non-zero, but is of the form of a delta function at the step. What this signifies physically is revealed by integrating (10) with respect to ξ across the step at constant time. Since $\Delta\xi \to 0$, the term in $\partial v/\partial\tau$ vanishes, with the result that $\Delta a = -\Delta\hat{P}_e$. This has a simple meaning: since the

internal pressure is continuous across the step, the area must decrease discontinuously by an amount equal to the step increase in external pressure $\hat{P}_e$.

In the static case, with the same distribution $\hat{P}_e(\xi)$, the area change at the step would be the same, namely, $\Delta a = -\Delta\hat{P}_e$. By the principle of superposition of solutions, therefore, a wavelet passing through the region of a step is in effect governed by the homogeneous wave equation and experiences neither a change in amplitude nor a reflexion when crossing the step.

Thus the conclusion is that purely spatial gradients in $\hat{P}_e$ do not generate waves nor do they modify the strength of transmitted waves or produce wave reflexions.

In § 9 wave transmission and reflexion at a step $\hat{P}_e(\xi)$, are considered when the mean fluid speed is not small compared with the wave speed; there it is shown that the foregoing results still apply unless second-order terms in the perturbation area and velocity are considered.

5.3. *An example: the linear ramp of constant amplitude*

A reconsideration of the problem of the instantaneously applied linear ramp of $\hat{P}_e$ (figure 2*a* with constant $\hat{P}^*_{em}$) nicely illustrates these physical concepts and clarifies the mathematical solution obtained previously.

Figure 10 shows the right-hand end of the ramp, which is approximated by a staircase of ten equal steps, each of strength 2 units. When the stairway is suddenly applied, equations (19) show that each step generates a right-moving wave of strength $+1$, across which $\Delta v = \Delta a = +1$, and a left-moving wave of strength -1, across which $-\Delta v = \Delta a = -1$. By adding up the contributions of all waves crossed by a particle (which moves essentially vertically in the ξ, τ diagram), one may enter in each zone a pair of numbers, the upper one representing a, the lower one representing v. Across each vertical line representing a step in $\hat{P}_e$, v and the internal pressure are continuous, but a jumps by 2 units.

Figure 10 clearly illustrates how the motion is created by the rightwards family of compression waves and the leftwards family of rarefaction waves generated at $\tau = 0$. These propagate with unchanged strength and are transmitted across the steps in $\hat{P}_e$ without modification or reflexion. The two families of waves are generated uniformly along the interval $0 < \xi < 1$. No waves are generated for $\xi < 0$ and $\xi > 0$. In the middle of the ramp, at $\xi = 0{\cdot}5$, the two families are equally present; hence their effects on area cancel each other, while their effects on velocity reinforce each other. Near the right-hand end of the ramp, the compression waves predominate, hence both a and v are positive. Near the left-hand end of the ramp the rarefaction waves predominate, hence v is positive, but a is negative.

At large times, $\tau > 1$, both families of waves have entirely left the ramp region, leaving behind a static situation: the velocity and pressure are constant and the area varies linearly with distance because of the linear change in $\hat{P}_e$. Outside of the ramp but within either the rightward or leftward running band of waves, v and a change linearly with both distance and time because only one propagating wave family is present, a family originally generated uniformly with distance at $\tau = 0$.

Taken to the limit of many small steps, figure 10 shows the phenomena which physically establish the solution represented in figures 2(*c*) and (*d*). These graphs of course agree with the numerical values in figure 10, having in mind the discrete character of the latter.

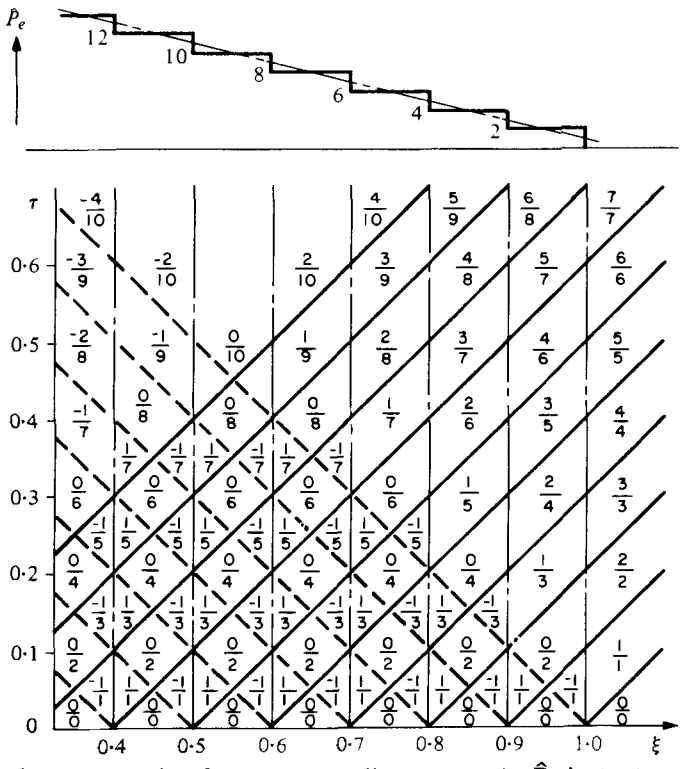

FIGURE 10. Wavelet construction for a constant linear ramp in $\hat{P}_e$, instantaneously applied, of strength 20 units. The ramp is approximated by a ten-step stairway. The solid lines represent positive waves generated of strength $+1$ in a and v; the dashed lines represent negative waves of strength -1 unit for a and $+1$ unit for v. In each zone the upper number represents a, the lower number represents v.

5.4. *Localized application of pressure*

Consider now a constant pressure $\hat{P}_e^*$ applied instantaneously over the *finite* interval $-0{\cdot}5 < \xi < 0{\cdot}5$. Figure 11 exhibits the solution, using the rules of calculation given in (19)

For reasons of symmetry, this solution also applies to a tube with a closed end at $\xi = 0$ that lies in the region $\xi > 0$. The wavelet 4–8 would then be seen as the reflexion at the closed end of the wavelet 1–4.

After a period of interaction the four wavelets generated at $\xi = \pm 0{\cdot}5$ pass completely out of the pressurized zone. For $\tau > 1$, the pressurized zone contains stationary fluid in a reduced area; all other effects of the pressure application are confined to the uniform corridors 2 and 3 which propagate with speeds $d\xi/d\tau = \pm 1$, respectively.

6. Distributions of applied pressure yielding the homogeneous wave equation

Although general methods of solution for arbitrary $\hat{P}_e(\xi, \tau)$, using the method of characteristics, have been presented, the solutions for a considerable variety of applied pressure distributions can be obtained more easily. These are for cases where (12) or (13) reduces to the homogeneous plane wave equation. The solutions may then be

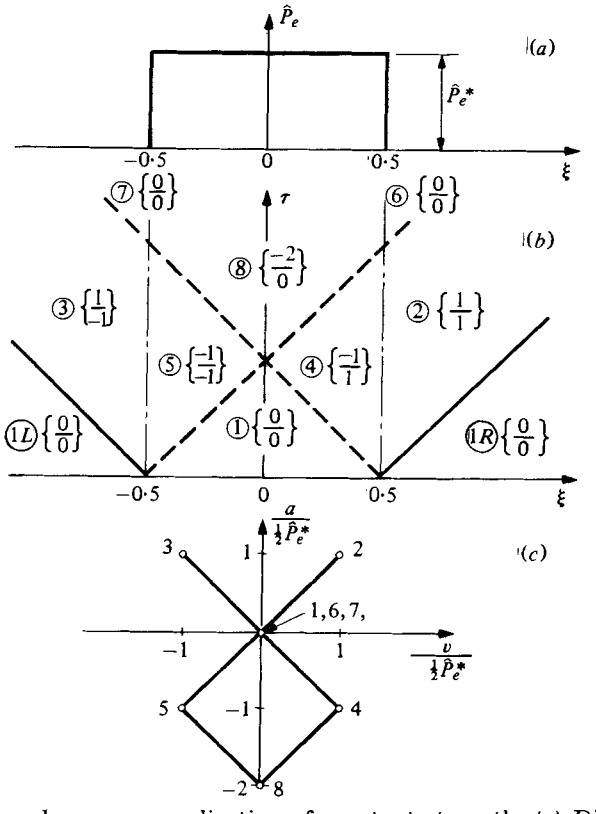

FIGURE 11. A hat-shaped pressure application of constant strength. (*a*) Distribution of $\hat{P}_e(\xi)$, constant in time. (*b*) Wave diagram. Upper numbers: $2a/\hat{P}_e^*$; lower numbers: $2v/\hat{P}_e^*$. (*c*) State diagram.

written down quickly and in simple form. Fortunately, the distributions $\hat{P}_e(\xi, \tau)$ falling within this seemingly special class are in fact quite broad in scope, and are of considerable practical interest.

6.1. *The special distributions* $\hat{P}_e(\xi, \tau)$

The distributions $\hat{P}_e(\xi, \tau)$ which lead (either directly or by a transformation of variables) to the homogeneous plane wave equation are those for which $\hat{P}_{e,\xi\xi}$ either vanishes or is a function of ξ or τ only; together with those for which $\hat{P}_{e,\xi\tau}$ either vanishes or is a function of ξ or τ only. All such possible forms are contained within the additive function

$$\hat{P}_e = T_0(\tau) + \xi . T_1(\tau) + \frac{\xi^2}{2} . T_2(\tau) + \Xi_0(\xi) + \tau . \Xi_1(\xi). \tag{25}$$

Direct substitution verifies that the solutions of (9), (10), (12) and (13) are then

$$a = f(\xi - \tau) + g(\xi + \tau) - \Xi_0(\xi) - \tau . \Xi_1(\xi) + T_2^{(2)}(\tau) \tag{26}$$

and

$$v = f(\xi - \tau) - g(\xi + \tau) - T_1^{(1)}(\tau) + \Xi_1^{(1)}(\xi) - \xi . T_2^{(1)}(\tau), \tag{27}$$

where the superscripts in parentheses indicate integration with respect to the respective arguments either once, signified by $(\ )^{(1)}$, or twice, signified by $(\ )^{(2)}$; e.g.

$$T_2^{(2)}(\tau) = \int_0^\tau \int_0^\tau T_2(\tau)\, d\tau\, d\tau.$$

Initial conditions. Let the distributions of area and velocity at $\tau = 0$ be given by $a_0(\xi) \equiv a(\xi, 0)$ and $v_0(\xi) \equiv v(\xi, 0)$. Then the functions f and g in (26) and (27) are given by

$$f(\xi-\tau) = \tfrac{1}{2}[a_0(\xi-\tau)+v_0(\xi-\tau)+\Xi_0(\xi-\tau)-\Xi_1^{(1)}(\xi-\tau)] \tag{28}$$

and

$$g(\xi+\tau) = \tfrac{1}{2}[a_0(\xi+\tau)-v_0(\xi+\tau)+\Xi_0(\xi+\tau)+\Xi_1^{(1)}(\xi+\tau)]. \tag{29}$$

6.2. *Collapse from a uniform state*

We shall consider here cases in which the initial state is free of motion and uniform in area, and where positive external pressures are applied in order to empty the tube.

For this case the initial conditions are $a_0(\xi) = 0$ and $v_0(\xi) = 0$. Using these, (26), (27), (28) and (29) may be brought into the forms:

$$\begin{aligned} a = & -\Xi_0(\xi)+\tfrac{1}{2}[\Xi_0(\xi-\tau)+\Xi_0(\xi+\tau)] \\ & -\tau.\Xi_1(\xi)-\tfrac{1}{2}[\Xi_1^{(1)}(\xi-\tau)-\Xi_1^{(1)}(\xi+\tau)] \\ & +T_2^{(2)}(\tau); \end{aligned} \tag{30}$$

$$\begin{aligned} v = & \tfrac{1}{2}[\Xi_0(\xi-\tau)-\Xi_0(\xi+\tau)] \\ & +\Xi_1^{(1)}(\xi)-\tfrac{1}{2}[\Xi_1^{(1)}(\xi-\tau)+\Xi_1^{(1)}(\xi+\tau)] \\ & -T_1^{(1)}(\tau)-\xi.T_2^{(1)}(\tau). \end{aligned} \tag{31}$$

We now examine how the mode of emptying is determined by the several individual components of $\hat{P}_e(\xi, \tau)$ appearing in (25).

(*a*) *The function* $T_0(\tau)$. This does not appear at all in the solution, reflecting a conclusion previously deduced in § 5.1 by physical argument: a temporal variation in $\hat{P}_e$ has no effect on a or v if it is spatially uniform.

(*b*) *The function* $T_1(\tau)$. In this case $\hat{P}_e$ is linear in ξ, with slope that varies arbitrarily with τ. Equations (30) and (31) give $a = 0$ and $v = -T_1^{(1)}(\tau)$. Thus the area is unaltered and the velocity is independent of ξ. This is the result already obtained for the linear ramp of figure 2 (see table 2); here it is applicable only to zone 1 because of waves generated at the corners of the ramp.

(*c*) *The function* $T_2(\tau)$. Now $\hat{P}_e$ is parabolic in ξ, with its amplitude an arbitrary function of time. Apart from a deliberate pressurization, such a variation in $\hat{P}_e$ would occur as the result of angular accelerations resulting, for instance, from an automobile collision.

From (30) and (31), $a = T_2^{(2)}(\tau)$ and $v = -\xi.T_2^{(1)}(\tau)$. Thus, for $T_2(\tau) < 0$, the tube collapses uniformly, and the velocity varies linearly with distance.

More particularly, suppose a constant parabolic distribution is applied suddenly: $\hat{P}_e = (1-\xi^2)\,T_2(\tau)$, where $T_2(\tau) = 0$ for $\tau \leqslant 0$; and $T_2(\tau) = T_2^*$ for $\tau > 0$. Then $a = -T_2^*.\tau^2$ (uniform, but increasingly rapid collapse), and $v = 2T_2^*.\xi\tau$ (velocity increasing linearly with both ξ and τ).

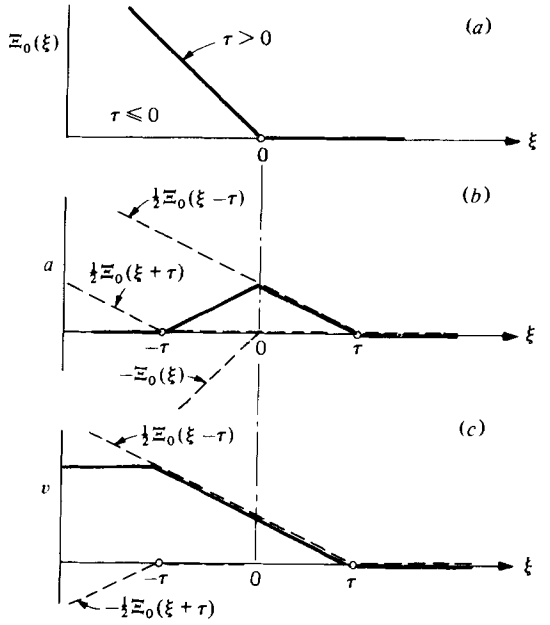

FIGURE 12. Graphical solution for a step change in the slope of $\Xi_0(\xi)$. (*a*) Distribution $\Xi_0(\xi)$ applied at $\tau = 0$. (*b*), (*c*) The distributions of $a(\xi;\tau)$ and $v(\xi;\tau)$, shown by solid lines, are found by algebraic additions of the components of (30) and (31), shown by the dashed lines.

(*d*) *The function* $\Xi_0(\xi)$. This represents an arbitrary distribution of applied pressure with distance, instantaneously applied and constant in time.

(i) *Graphical solution.* As may be seen from the first lines of (30) and (31), the solutions for $a(\xi,\tau)$ and $v(\xi,\tau)$ are easily obtained graphically by additions and subtractions of several terms, each representing some multiple of the function $\Xi_0(\xi)$ translated along ξ by an appropriate amount: 0, $+\tau$, or $-\tau$. The procedure is illustrated in figure 12 for a local discontinuity in slope $\partial\hat{P}_e/\partial\xi$. The resulting solutions agree with those of figures 2(*c*) and (*d*) in the neighbourhood of $\xi = 1$, up to $\tau = \frac{1}{2}$, beyond which figures 2 and 12 can no longer be compared.

The graphical solutions for $a(\xi,\tau)$ and $v(\xi,\tau)$, as given by the first lines of (30) and (31), are not limited in applicability to particular ranges of ξ and τ, even when there are singularities in $\hat{P}_{e,\xi\xi}$. One may quickly verify that the graphical solution easily and correctly produces the full results of figures 2, 4 and 6 when the applied pressure distributions are time-invariant. To clarify the point: the results are not restricted, for example, to zone 1 of figure 2(*b*).

(ii) *Parabolic distribution of* $\Xi_0(\xi)$. Consider the function $\Xi_0(\xi) = \hat{P}^*_{em}[1 - \xi - \frac{1}{2}b\xi^2]$. Then (30) and (31) yield $a/\hat{P}^*_{em} = -\frac{1}{2}b\tau^2$ and $v/\hat{P}^*_{em} = (1 + b\xi)\tau$. The linear term recovers the results previously obtained for the linear distribution of figure 2 and for the function $T_1(\tau) = \text{constant} = -\hat{P}^*_{em}$. The quadratic term recovers the results for $T_2(\tau) = \text{constant} = -b\hat{P}^*_{em}$. However, because of the way in which the initial conditions were used to obtain (28) and (29), these specific algebraic results are limited to a triangular region like zone 1 of figure 2, defined by the wavelet trajectories originating at the edges of the zone in which the prescribed $\Xi_0(\xi)$ is applicable. We repeat, however, that the graphical solution is not so limited.

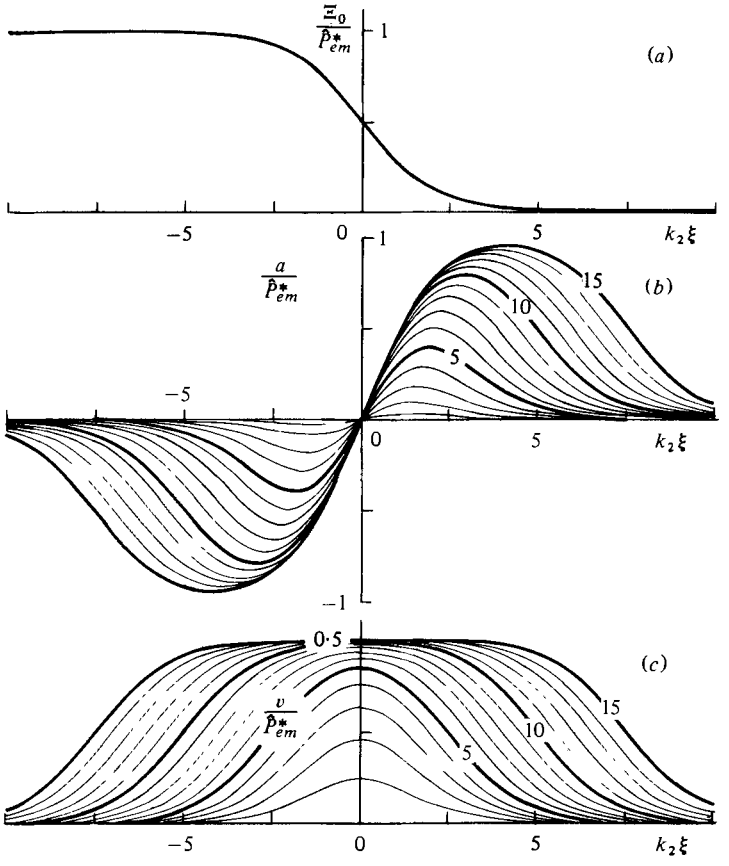

FIGURE 13. Asymptotic pressure ramp, $\Xi_0(\xi) = P^*_{em}/[1+k_1\exp(k_2\xi)]$. (*a*) Distribution of applied pressure. (*b*), (*c*) Distributions of $a(k_2\xi; k_2\tau)$ and $v(k_2\xi; k_2\tau)$, for $k_1 = 1$. Numbers on curves represent values of $2k_2\tau$.

(iii) *An asymptotic ramp in* $\Xi_0(\xi)$ (*figure* 13*a*). The asymptotic pressure ramp, $\Xi_0(\xi) = \hat{P}^*_{em}/[1+k_1\exp(k_2\xi)]$, is of interest because it removes the physically impracticable corners of the linear ramp of figure 2. The solution, according to (30) and (31), is given by

$$a/\hat{P}^*_{em} = -\frac{1}{1+k_1\exp(k_2\xi)} + \frac{\frac{1}{2}}{1+k_1\exp[k_2(\xi-\tau)]} + \frac{\frac{1}{2}}{1+k_1\exp[k_2(\xi+\tau)]},$$

$$v/\hat{P}^*_{em} = \frac{\frac{1}{2}}{1+k_1\exp[k_2(\xi-\tau)]} - \frac{\frac{1}{2}}{1+k_1\exp[k_2(\xi+\tau)]}.$$

Typical distributions of $a/\hat{P}^*_{em}$ and $v/\hat{P}^*_{em}$ are shown in figures 13(*b*) and (*c*). These are generally similar to the results for the linear ramp of pressurization (figures 2*c* and *d*), but the effects of discontinuities in slope are no longer present.

When $k_2 \to \infty$, the asymptotic ramp approaches as a limit the step of figure 4. It may then be verified that the formulas above pass over in the limit to the results of figures 4(*b*) and 6(*a*) and of equation (19).

(iv) *A rectangular distribution applied to a tube with a closed end.* Using the method

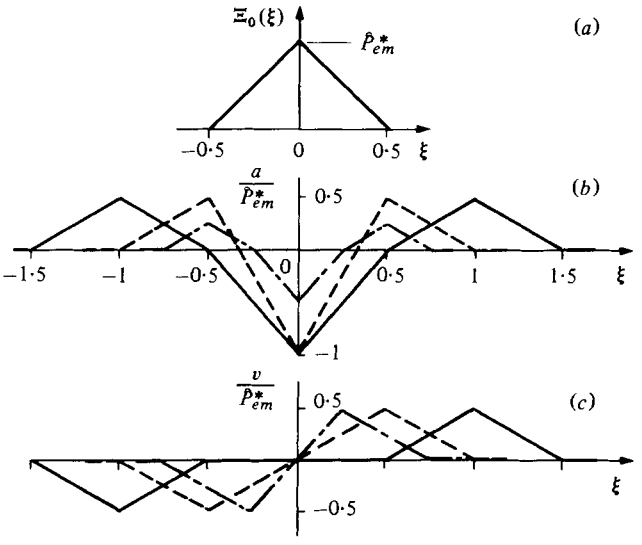

FIGURE 14. Triangular pressure ramp applied to a vessel with closed end. (*a*) Distribution of applied pressure. (*b*), (*c*) Distributions of area and velocity: ——·——, $\tau = 0{\cdot}5$; – – –, $\tau = 1{\cdot}0$; ——, $\tau = 2{\cdot}0$.

of pressure pulses, we have already given the solution for a rectangular, constant distribution of $\hat{P}_e$, applied suddenly to a vessel with a closed end (figure 11). The result is of interest because it approximates the simplest way of pressurizing a limb. Note that the emptying begins at the downstream edge of the pressurized region; the high velocity there, associated with a reduced area that is followed by an area increase, tends in practice to produce head losses that would reduce the rate of emptying.

(v) *A triangular distribution* (*figure* 14). The flow-reducing effect just mentioned may be substantially averted by employing a graded application of pressure, decreasing from upstream to downstream. Whereas in figure 11 the flow is accelerated mainly by *upstream*-running rarefaction waves which decrease the area, in figure 14 the flow is accelerated in addition by *downstream*-running waves which increase the area at the point of highest velocity.

This solution, in the region $\xi > 0$, applies also to gravity drainage without external pressurization. As given, it refers to a tube, initially uniform in the horizontal position and closed at one end, which is suddenly tilted to some fixed angle to the horizontal. However, if the tube is initially tilted, with both ends closed, and the lower end is suddenly opened, the solution given still applies provided that the perturbations in area are deemed to be superposed upon the linear area distribution associated with the initial static state.

(vi) *A ramp at the edge of a rectangular distribution.* Any practical attempt to apply uniform pressure to a part of a limb will actually produce a ramp at the edge of the pressurized region. Figure 15 shows a simple distribution modelling this effect. It is seen that collapse first occurs at the edge of the constant-pressure region, at a location of high velocity. This localized constriction, as in case (iv), would in practice induce losses that in turn would reduce the rate of emptying.

(*e*) *The function* $\Xi_1(\xi)$. This represents pressurizations of unchanging spatial form, the amplitudes of which grow uniformly in time. Since external pressures cannot be

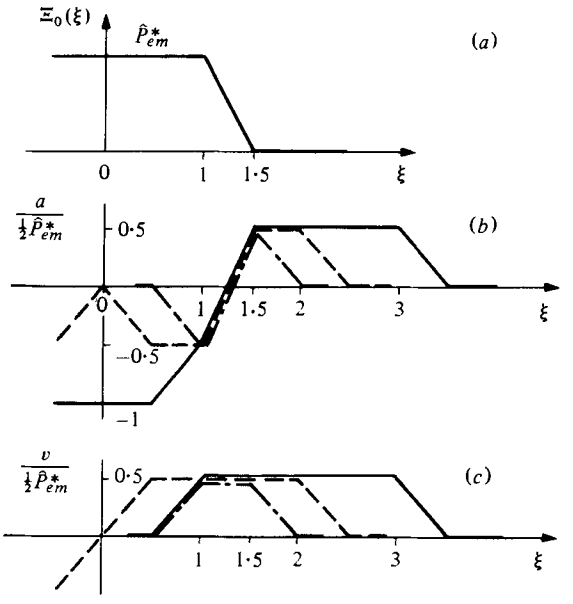

FIGURE 15. Rectangular applied pressure with linear edge region. (*a*) Distribution of applied pressure, symmetrical about $\xi = 0$. (*b*), (*c*) Distributions of area and velocity: ———, $\tau = 0{\cdot}5$; – – –, $\tau = 1{\cdot}0$; ——, $\tau = 2{\cdot}0$.

applied instantaneously, the solutions now discussed refer to the early stages of any rapid pressurization, as well as to a deliberate linear rise.

The second lines of (30) and (31) show that the graphical method of solution is convenient for these cases.

Figure 16 shows the solution for a rectangular distribution of applied pressure, as in figure 11, but with the amplitude $\hat{P}_e^*$ growing linearly in time. In addition to the graphical method, this problem is accessible to the concept of pressure pulses. Over the range $-0{\cdot}5 < \xi < 0{\cdot}5$, small increments $\delta\hat{P}_e$ are applied uniformly at each interval of time $\delta\tau$. Thus rightward- and leftward-moving wavelets are uniformly shed from the lines $\xi = \pm 0{\cdot}5$. The effects of these on $a(\xi, \tau)$ and $v(\xi, \tau)$ may be summed at any point in the ξ, τ field.

As illustrated in figure 16, the points of maximum velocity occur first at the edges of the pressurized region. For $\tau > 1$, the regions of maximum velocity spread outwards. Within the compression zone the area continues to decrease as $\hat{P}_e$ increases, while inflation waves spread outwards beyond the inflation zone.

6.3. *Refilling of a vessel*

In most medical applications of vessel emptying, it is necessary to refill the vessel periodically. If one attempts cardiac assist by means of counter-pulsation on the arterial volume of the legs, for instance, effective operation requires that the arteries substantially refill within a fraction of one heartbeat. Thus we are concerned with the details of how a partially emptied vessel refills.

Initial condition. We shall assume that, emptying having ended, the situation at $\tau = 0$ is one without motion but with some distribution of $a(\xi, \tau)$ from an appropriate base state.

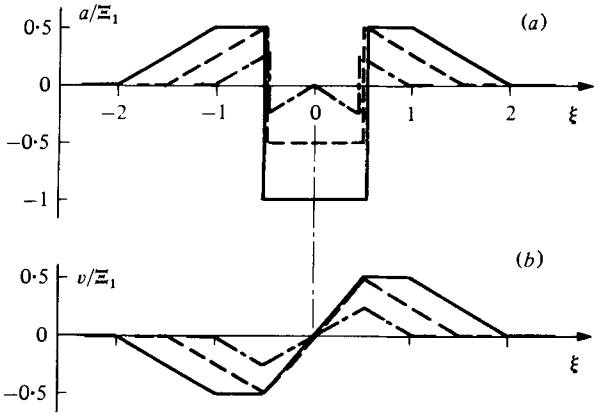

FIGURE 16. A rectangular pressure distribution as in figure 11, but with the amplitude $\hat{P}_e$ growing uniformly in time. —·—·—, $\tau = 0{\cdot}5$; – – –, $\tau = 1{\cdot}0$; ——, $\tau = 1{\cdot}5$.

Solution. One method is to suppose that, for $\tau < 0$, there exists the pressurization function $\Xi_0(\xi)$ which maintains the static configuration before refilling begins. To represent the release of external pressure, we then add the function $-\Xi_0(\xi)$ at $\tau = 0$. This procedure is easily effected by means of the graphical method.

Alternatively, we note that $a_0(\xi) \equiv a(\xi, 0)$ is known, and that $v_0(\xi) \equiv v(\xi, 0) = 0$. Moreover, $\hat{P}_e(\xi, \tau) = 0$ during refilling, hence a and v obey the wave equation. Applying these considerations to the determination of $f(\xi - \tau)$ and $g(\xi - \tau)$ in (26) and (27) we obtain the solution to the refilling problem in the form

$$a(\xi, \tau) = \tfrac{1}{2}a_0(\xi - \tau) + \tfrac{1}{2}a_0(\xi + \tau), \tag{32}$$

$$v(\xi, \tau) = \tfrac{1}{2}a_0(\xi - \tau) - \tfrac{1}{2}a_0(\xi + \tau). \tag{33}$$

These may also be solved graphically by suitable translations and graphical additions of the function $a_0(\xi)$.

A more physical interpretation of the solution is that the two terms in each of (32) and (33) represent two families of area waves accompanied by corresponding velocity and pressure signals. The $\mathscr{R}$ waves (rightwards) propagate along lines $\xi - \tau =$ constant; the $\mathscr{L}$ waves (leftwards) along lines $\xi + \tau =$ constant. Each wavelet carries a certain signal strength, determined by the change in properties *across* the wave. *Across* the $\mathscr{R}$ wave, in the direction $\xi + \tau =$ constant, (32) and (33) give

$$\delta a_{\mathscr{R}} = \delta v_{\mathscr{R}} = \delta P_{\mathscr{R}}. \tag{34}$$

Similarly, *across* an $\mathscr{L}$ wave, in the direction $\xi - \tau =$ constant,

$$\delta a_{\mathscr{L}} = -\delta v_{\mathscr{L}} = \delta P_{\mathscr{L}}. \tag{35}$$

These provide simple and convenient rules of calculation.

Refilling of a step change in area. Figure 17 shows the solution to this case, based upon (34) and (35). The right-hand end of the vessel is assumed closed. The rightward compression wave $\mathscr{R}$ and leftward rarefaction wave $\mathscr{L}$ remove the initial discontinuity in area, and are of such respective strengths as to create continuity of pressure, area and velocity between fields 3 and 4. Field 3 is a corridor of area decrease and velocity increase, which in effect supplies from the tubing at the left the fluid that ultimately refills the tube in field 5.

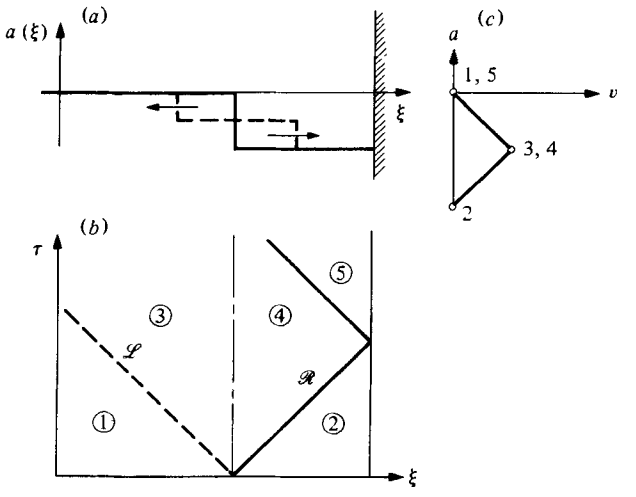

FIGURE 17. Refilling of a step change in area. (*a*) Area distribution at $\tau = 0$. (*b*) Wave diagram. (*c*) State diagram.

7. Solutions with prescribed area variation

Often it is of greater practical value to prescribe the desired area variation $a(\xi, \tau)$ and then to determine the applied pressure distribution $\hat{P}_e(\xi, \tau)$ needed to effect it.

7.1. *Method of solution*

We suppose $a(\xi, \tau)$ to be given. Integration of (9) with respect to ξ, while holding τ constant, then produces

$$v = -\int a_\tau(\xi, \tau)\, d\xi + \theta_1(\tau), \tag{36}$$

where $\theta_1(\tau)$ is arbitrary. Similarly, integration of (10) with respect to ξ, again while holding τ constant, and with $\partial v/\partial \tau$ calculated from (36), yields

$$\hat{P}_e = \int\int a_{\tau\tau}\, d\xi\, d\xi - \int a_\xi d\xi - \xi\theta_1'(\tau) + \theta_2(\tau), \tag{37}$$

where the function $\theta_2(\tau)$ is also arbitrary but immaterial.

7.2. *Examples*

We consider examples of tube emptying from an initial state of uniform area and zero velocity, i.e. $a(\xi, 0) = 0 = v(\xi, 0)$.

(i) *Uniform collapse.* If we set $a = a(\tau)$, and arbitrarily set $\theta_1(\tau) = 0$, then equation (36) gives the velocity as $v = -\xi a'(\tau)$, with the further requirement that $a'(0) = 0$; and equation (37) gives the applied pressure as $\hat{P}_e = \frac{1}{2}\xi^2 a''(\tau)$. These results are seen to correspond with the function $T_2(\tau)$ of (25), and with the solutions for a and v given in § 6.2 (*c*).

(ii) *A uniformly translating wave of collapse.* Let the area variation be described by $a = a(\xi - V_a\tau)$, where V_a is the dimensionless speed with which a given area profile propagates uniformly in the ξ direction. Then (36) and (37) yield

$$v = V_a . a(\xi - V_a\tau) + \theta_1(\tau)$$

and

$$\hat{P}_e = (V_a^2 - 1) . a(\xi - V_a\tau) - \xi . \theta_1'(\tau).$$

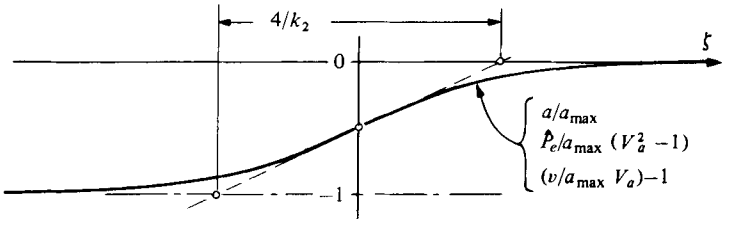

FIGURE 18. An asymptotic area ramp moving with dimensionless speed V_a, with the corresponding curves for velocity and applied pressure.

Omitting the effects of $\theta_1(\tau)$, which have been determined already from (25) and *seq.*, and discussed specifically in § 6.2(*b*), the interesting result here is that the sign of the external pressure depends upon the dimensionless speed V_a of the area wave, relative to unity. Thus, counter-intuitively, a wave of area reduction travelling along $+\xi$ requires a negative applied pressure if $V_a > 1$.

One interpretation of this result derives from a consideration of the steady flow that is perceived in a co-ordinate frame travelling with the wave, in which the fluid moves from right to left. When the flow is subcritical ($V_a < 1$) an area decrease in the direction of flow requires an increase of external pressure, while the opposite is true at supercritical speed ($V_a > 1$); this finding has previously been established for steady flow (Shapiro 1977*b*).

Consider the specific case (figure 18) of an asymptotic ramp of area reduction of the form $a = -a_{\max}(1+k_1\exp[k_2\zeta])^{-1}$, where $\zeta \equiv \xi - V_a\tau$, travelling with the speed V_a. The solutions for the area and applied pressure distributions may be expressed as

$$\frac{v}{a_{\max}V_a} - 1 = \frac{\hat{P}_e}{a_{\max}(V_a^2-1)} = \frac{a}{a_{\max}} = -(1+k_1\exp[k_2\zeta])^{-1}$$

and are displayed in figure 18.

(iii) *Area variation of the form* $T(\tau).\Xi(\xi)$. Introduction of this form into (36) and (37) leads to

$$v = -T'(\tau).\int \Xi(\xi)\,d\xi + \theta(\tau)$$

and

$$\hat{P}_e = T''(\tau).\int\int \Xi(\xi)\,d\xi\,d\xi - T(\tau).\Xi(\xi) - \xi\theta'(\tau).$$

From the condition that $a(\xi, 0) = 0$, it is required that $T(0) = 0$. And, from the condition that $v(\xi, 0) = 0$, the first expression above may be brought into the form

$$v = \theta(\tau) - \theta(0).T'(\tau)/T'(0),$$

which shows that with this specified area variation the velocity is independent of distance. This is a powerful solution, considering the generality of the assumed area variation.

8. Wave generation in a moving fluid

The concept of unit wave generation for an instantaneous step in $\hat{P}_e$ over a limited range of ξ was developed previously for the case where the step is spatially fixed in a reference frame moving with the mean fluid speed [see figures 4, 6(*a*) and (*b*), and equation (19)]. Consequently, the results are applicable to a stationary step only if u, or, more strictly, $S \equiv u/c$, is small.

Consider now a stationary time-varying step with external pressures so large that the dimensionless speed, S, becomes substantial. So that linearized concepts may be used, $\hat{P}_e$ is broken up into small steps, each of which is considered separately. However, since S need not now be of perturbation order, we must determine how equations (19) are modified for finite values of S. The analysis, we shall see, offers physical insights into certain aspects of nonlinear behaviour.

8.1. *The case* $S < 1$ (*figure* 19)

Consider a region of sub-critical flow ($S < 1$) with uniform properties, A, u, p and c and with an external pressure p_e. At the time t^*, the external pressure in the region $x < x^*$ is instantaneously raised by the amount $\delta p_e^{(t)}$. This generates the wavelets $\mathscr{R}$ and $\mathscr{L}$, propagating at the speeds $u \pm c$. When these wavelets pass over a fluid particle, they produce the changes $\delta A_{\mathscr{R}}$, $\delta u_{\mathscr{R}}$, etc. shown in the diagram for the several angular fields of constant properties.

Assuming all changes to be of small order, and neglecting second-order terms, the changes across the wavelets $\mathscr{R}$ and $\mathscr{L}$ may be expressed respectively as

$$\delta p_{\mathscr{R}} = \rho c\, \delta u_{\mathscr{R}}, \quad \delta A_{\mathscr{R}}/A = \delta u_{\mathscr{R}}/c; \tag{38}$$

$$\delta p_{\mathscr{L}} = -\rho c\, \delta u_{\mathscr{L}}, \quad \delta A_{\mathscr{L}}/A = -\delta u_{\mathscr{L}}/c. \tag{39}$$

Corresponding to the jump $\delta p_e^{(t)}$ at the location x^* are jumps in the fluid properties. Across the jump, the space derivatives in the equations of continuity and momentum overwhelm the time derivatives, hence the flow may be treated locally as quasi-steady. Accordingly, the volume flows are equal on the two sides;

$$(A + \delta A_{\mathscr{L}})(u + \delta u_{\mathscr{L}}) = (A + \delta A_{\mathscr{R}})(u + \delta u_{\mathscr{R}})$$

and, in the absence of dissipative losses, Bernoulli's equation is applicable:

$$(p + \delta p_{\mathscr{R}}) + \tfrac{1}{2}\rho(u + \delta u_{\mathscr{R}})^2 = (p + \delta p_e^{(t)} + \delta p_{\mathscr{L}}) + \tfrac{1}{2}\rho(u + \delta u_{\mathscr{L}})^2.$$

Retaining only first-order terms, and combining these expressions with equations (38) and (39), we manipulate the equations into the forms

$$\frac{\delta p_{\mathscr{R}}/\rho c^2}{\delta p_e^{(t)}/\rho c^2} = \frac{\delta u_{\mathscr{R}}/c}{\delta p_e^{(t)}/\rho c^2} = \frac{\delta A_{\mathscr{R}}/A}{\delta p_e^{(t)}/\rho c^2} = \frac{1}{2(1+S)}, \tag{40}$$

$$\frac{\delta p_{\mathscr{L}}/\rho c^2}{\delta p_e^{(t)}/\rho c^2} = -\frac{\delta u_{\mathscr{L}}/c}{\delta p_e^{(t)}/\rho c^2} = \frac{\delta A_{\mathscr{L}}/A}{\delta p_e^{(t)}/\rho c^2} = -\frac{1}{2(1-S)}. \tag{41}$$

Limiting case, $S \to 0$. The formulas go to the limits previously derived in (19). The absolute strengths of the $\mathscr{R}$ and $\mathscr{L}$ waves are equal, and there is a discontinuity in A, but not in u or p, at the location x^*.

Asymmetries when $S \neq 0$. When S is not zero, the absolute strengths of the $\mathscr{R}$ and $\mathscr{L}$ waves differ, and at the location x^* the jump $\delta p_e^{(t)}$ creates discontinuities in all properties: A, u and p. When $\delta p_e^{(t)}$ is positive, in the sense of figure 19, the $\mathscr{R}$ wave is compressive and the $\mathscr{L}$ wave expansive, but the former is weaker than the latter.

Entirely apart from those nonlinearities associated with changes in the values of A and c, it is evident from the results given here that finite amplitudes of $\hat{P}_e$ will produce asymmetrical distortions of the solutions of figures 2, 4, 5, 6, etc.

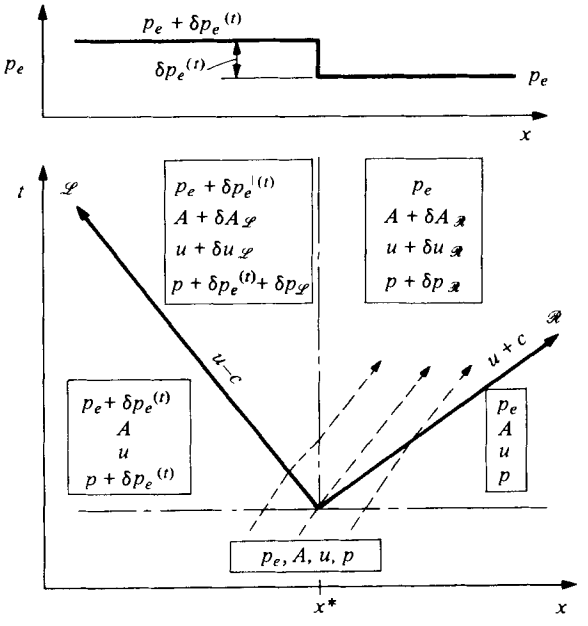

FIGURE 19. Pressure pulses generated by the application of external pressure $\delta p_e^{(t)}$, for subcritical flow, $S < 1$. Dashed lines represent particle trajectories.

If $\delta p_e^{(t)}$ occurs in the region $x > x^*$, then the signs of (40) and (41) are reversed. If the flow is in the negative x direction, (40) and (41) remain correct provided that S is substituted as a negative number.

8.2. *The case $S > 1$ (figure 20)*

The formulation of the problem now differs from that of figure 19 in that a fluid particle enters the $\mathscr{L}$ wave *after* first crossing the quasi-steady discontinuity at x^*. Writing the appropriate wavelet equations for $\mathscr{R}$ and $\mathscr{L}$, and the quasi-steady equations across x^*, as was done for $S < 1$, one finds, surprisingly, the *same result*: that is, (40) and (41) apply to this case as well.

At supercritical speeds, however, we see that a positive $\delta p_e^{(t)}$ produces compressive waves in *both* directions.

When $S \to \infty$, the generated wavelets become vanishingly small in strength.

8.3. *The limit as $S \to 1$*

The right-hand side of (40) approaches the value $\frac{1}{4}$ as S goes to unity. Thus, for instance, $\delta p_{\mathscr{R}} \to \frac{1}{4}\delta p_e^{(t)}$.

Inspection of (41) seems to suggest that the $\mathscr{L}$ wave becomes infinitely strong as $S \to 1$. This is not true, as another consideration comes into play. In steady flow, it has been shown (Shapiro 1977*b*) that

$$(1-S^2)\frac{dS^2}{S^2} = \mathscr{M}\frac{dp_e}{\rho c^2}; \quad \mathscr{M} = 3 + \frac{\alpha \mathscr{P}''}{\mathscr{P}'}. \tag{42}$$

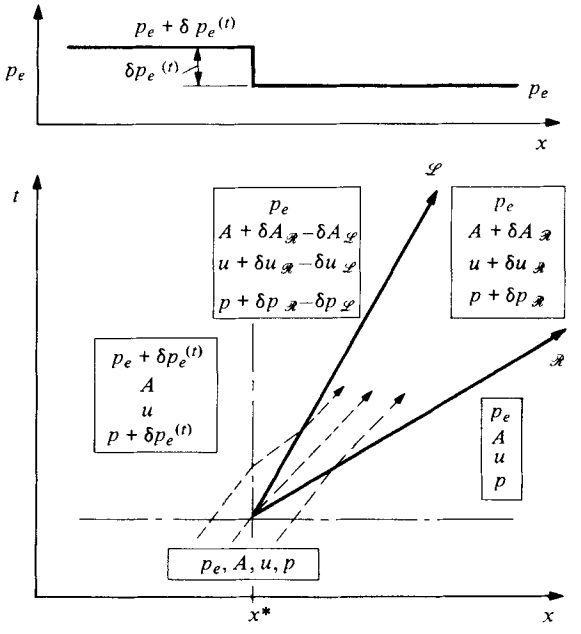

FIGURE 20. Similar to figure 19, but for supercritical flow, $S > 1$.

Inspection of this formula reveals the important consequence that, when

$$\mathscr{M}\, dp_e/dx > 0,$$

the solution cannot be continued beyond $S = 1$. Thus, increasing the value of p_e ultimately produces 'choking', analogous to gas-dynamic choking in convergent–divergent nozzles. In the present context, this means that, if $\mathscr{M}\delta p_e^{(t)} < 0$, the allowable value of $-\mathscr{M}\delta p_e^{(t)}$ goes to zero as $S \to 1$ [note that dp_e of (42) corresponds to $-\delta p_e^{(t)}$]. In the neighbourhood $S \cong 1$, the solution of (42) for the maximum possible value of $\delta p_e^{(t)}$ is of the limiting form

$$\left[-\frac{\delta p_e^{(t)}}{\rho c^2}\right]_{\max} \cong \frac{2}{\mathscr{M}}(1-S)^2.$$

Therefore, as $S \to 1$, (41) yields maximum values

$$\left(\frac{\delta p_{\mathscr{L}}}{\rho c^2}\right)_{\max} = -\left(\frac{\delta u_{\mathscr{L}}}{c}\right)_{\max} = \left(\frac{\delta A_{\mathscr{L}}}{A}\right)_{\max} \cong \frac{1-S}{\mathscr{M}}.$$

Accordingly, the strength of the $\mathscr{L}$ wave remains bounded as $S \to 1$.

9. Wave transmission and reflexion in a moving fluid

9.1. *Intent and assumptions of the analysis*

Consider a tube with non-uniform rest area $A_0(x)$, non-uniform stiffness $K_p(x)$, on which a non-uniform external pressure $p_e(x)$ is acting. Let us suppose that wavelets have been generated, either at the boundaries, or away from the boundaries by means of steps $\delta p_e^{(t)}$. The non-uniformities will cause changes in the amplitude of the wavelet

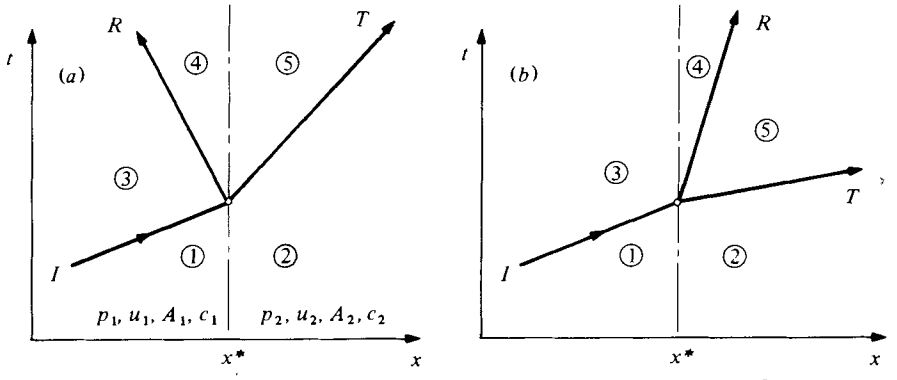

FIGURE 21. Wavelet incident upon a discontinuity in A and c.
(*a*) Subcritical flow, $S < 1$. (*b*) Supercritical flow, $S > 1$.

as it propagates, and will also cause waves travelling in the opposite direction (partial reflexions) to appear.

The nature of these events, the changes in the transmitted wave and the generation of reflected waves, will now be established in a manner that is useful for gaining physical insights. We suppose that the non-uniformities are lumped into steps, between which the values A_0, K_p and p_e are assumed uniform. In this view we focus attention on what happens when a wavelet arrives at a junction where there are step changes in A_0, K_p and p_e. Since we assume the incident wavelet to be of small amplitude, all second-order effects connected with it are ignored.

9.2. *A finite discontinuity in c and A*

First we consider the case where a small-amplitude wavelet is incident upon a junction at which the step changes in A_0, K_p and p_e are arbitrary and of finite size (figure 21). Insofar as the fluid-mechanical equations are concerned, the steps in A_0, K_p and p_e are important only as they affect the local values of c and A.

The case $S < 1$. In figure 21 (*a*), we suppose that there exists a discontinuity at x^* such that, initially, the properties for $x < x^*$ are: p_1, u_1, A_1 and c_1; and, for $x > x^*$: p_2, u_2, A_2 and c_2. When incident wavelet I (which changes the fluid state from 1 to 3) reaches the discontinuity, it is in part transmitted as wavelet T (which changes the fluid state from 2 to 5) and it is in part reflected as wavelet R (which changes the fluid state from 3 to 4).

Employing the small-amplitude formulas for wavelets, and ignoring quadratic terms, we may write the dynamical and continuity equations for the three wavelets as

$$u_3 - u_1 = \delta p_I/\rho c_1, \quad A_3 - A_1 = A_1 \delta p_I/\rho c_1^2;$$
$$u_4 - u_3 = -\delta p_R/\rho c_1, \quad A_4 - A_3 = A_1 \delta p_R/\rho c_1^2;$$
$$u_5 - u_2 = \delta p_T/\rho c_2, \quad A_5 - A_2 = A_2 \delta p_T/\rho c_2^2.$$

As in § 8, the flow across the discontinuity is treated as quasi-steady by means of the equation of continuity and Bernoulli's theorem:

$$A_1 u_1 = A_2 u_2, \quad p_1 + \tfrac{1}{2}\rho u_1^2 = p_2 + \tfrac{1}{2}\rho u_2^2;$$
$$A_4 u_4 = A_5 u_5, \quad p_4 + \tfrac{1}{2}\rho u_4^2 = p_5 + \tfrac{1}{2}\rho u_5^2.$$

Combination and algebraic manipulation of all the foregoing yields the following transmission and reflexion ratios:

$$\frac{\delta p_T}{\delta p_I} = \frac{2(1+S_1)}{1+\dfrac{c_1/A_1}{c_2/A_2}+S_1\left(\dfrac{c_1}{c_2}\right)^2\left(1+\dfrac{c_2/A_2}{c_1/A_1}\right)}; \tag{43}$$

$$\frac{\delta p_R}{\delta p_I} = \frac{1+S_1}{1-S_1}\cdot\frac{1-\dfrac{c_1/A_1}{c_2/A_2}-S_1\left(\dfrac{c_1}{c_2}\right)^2\left(1-\dfrac{c_2/A_2}{c_1/A_1}\right)}{1+\dfrac{c_1/A_1}{c_2/A_2}+S_1\left(\dfrac{c_1}{c_2}\right)^2\left(1+\dfrac{c_2/A_2}{c_1/A_1}\right)}. \tag{44}$$

In these we see the strong role played by the ratio of the two acoustic impedances $\rho c/A$. Suppose, for instance, that $S = 0$: then, if $c_2/A_2 > c_1/A_1$, the transmitted wavelet is stronger (in pressure amplitude) than the incident wavelet, and the reflected wavelet is of the same sign as the incident wavelet; if, on the other hand, $c_1/A_1 > c_2/A_2$, the transmitted wavelet is weaker and the reflected wavelet is of opposite sense.

Unfortunately, the role of the speed index S cannot be simply stated from these results.

The case $S > 1$. The wave diagram is now as in figure 21 (*b*), the main difference being that the reflected wavelet R propagates in the positive x direction. In this case a fluid particle crosses the junction, from state 3 to 4, before its state is changed from 4 to 5 as it crosses wavelet R.

Following the same procedure as for $S < 1$, the results are obtained as

$$\frac{\delta p_T}{\delta p_I} = \frac{1+S_1}{2}\cdot\frac{1+\dfrac{c_2/A_2}{c_1/A_1}-S_1\left(\dfrac{A_1}{A_2}\right)^2\left(1+\dfrac{c_1/A_1}{c_2/A_2}\right)}{1-S_1^2\left(\dfrac{A_1}{A_2}\right)^2\left(\dfrac{c_1}{c_2}\right)^2} \tag{45}$$

and

$$\frac{\delta p_R}{\delta p_I} = -\frac{1+S_1}{2}\cdot\frac{1-\dfrac{c_2/A_2}{c_1/A_1}-S_1\left(\dfrac{A_1}{A_2}\right)^2\left(1-\dfrac{c_1/A_1}{c_2/A_2}\right)}{1-S_1^2\left(\dfrac{A_1}{A_2}\right)^2\left(\dfrac{c_1}{c_2}\right)^2}. \tag{46}$$

9.3. *The limit of a small discontinuity*

Now suppose that the changes from state 1 to state 2 across the junction J are very small. Accordingly, we write $A_1 = A$, $A_2 = A+\delta A_J$; $c_1 = c$, $c_2 = c+\delta c_J$; and $S_1 = S$.

The case $S < 1$. Inserting the above values into (43) and (44), expanding in powers of $\delta A_J/A$ and $\delta c_J/c$, and retaining only first-order terms, we get

$$\frac{\delta p_T-\delta p_I}{\delta p_I} = -\frac{1-S}{2(1+S)}\frac{\delta A_J}{A}+\frac{1+3S}{2(1+S)}\frac{\delta c_J}{c} \tag{47}$$

and

$$\frac{\delta p_R}{\delta p_I} = \frac{1+S}{2(1-S)}\left(\frac{\delta c_J}{c}-\frac{\delta A_J}{A}\right). \tag{48}$$

Now the changes $\delta c_J/c$ and $\delta A_J/A$ are in fact brought about by, and are related to, the changes $\delta A_0/A_0$ and $\delta K_p/K_p$ in tube properties, and the change $\delta p_e/\rho c^2$ in external

F	$\mathscr{T}_F$	$\mathscr{R}_F$
Pressure, p	$\left[1-\frac{(1+3S)\mathscr{M}}{4(1+S)}\right]\frac{1}{(1-S^2)}$	$\left(\frac{4-\mathscr{M}}{4}\right)\frac{1}{(1-S)^2}$
Speed, u	$\frac{\mathscr{M}}{4(1+S)^2}$	$-\left(\frac{4-\mathscr{M}}{4}\right)\frac{1}{(1-S)^2}$
Area, A	$\left[\frac{(3+S)\mathscr{M}}{4(1+S)}-2\right]\frac{1}{(1-S^2)}$	$\left(\frac{4-\mathscr{M}}{4}\right)\frac{1}{(1-S)^2}$

TABLE 3. Reflexion and transmission coefficients for a small discontinuity in external pressure, δp_e. $\mathscr{T}_F \equiv \frac{\delta F_T - \delta F_I}{\delta F_I}\Big/\frac{\delta p_e}{\rho c^2}$; $\mathscr{R}_F \equiv \frac{\delta F_R}{\delta F_I}\Big/\frac{\delta p_e}{\rho c^2}$, where F signifies p, u or A.

pressure. Using the appropriate steady-flow relationships (Shapiro 1977*b*), equations (47) and (48) may be reduced to the more explicit forms

$$2(1+S)^2\frac{\delta p_T-\delta p_I}{\delta p_I} = \left[1-\frac{1+3S}{1-S}\cdot\frac{\mathscr{M}-2}{2}\right]\frac{\delta p_e}{\rho c^2} - \left[1-\frac{S^2(1+3S)}{1-S}\cdot\frac{\mathscr{M}-2}{2}\right]\frac{\delta A_0}{A_0} + \left[\left(1-\frac{1+3S}{1-S}\cdot\frac{\mathscr{M}-2}{2}\right)\frac{K_p\mathscr{P}}{\rho c^2}+\frac{(1+3S)(1+S)}{2}\right]\frac{\delta K_p}{K_p}, \quad (49)$$

$$2(1-S)^2\frac{\delta p_R}{\delta p_I} = \left(\frac{4-\mathscr{M}}{2}\right)\frac{\delta p_e}{\rho c^2} - \left(1-\frac{\mathscr{M}-2}{2}S^2\right)\frac{\delta A_0}{A_0} + \left(\frac{4-\mathscr{M}}{2}\frac{K_p\mathscr{P}}{\rho c^2}-\frac{1-S^2}{2}\right)\frac{\delta K_p}{K_p}. \quad (50)$$

Limit of small speed index, $S \to 0$. In this case, an increase of A_0 across the discontinuity weakens the transmitted wavelet, and produces a reflected wavelet of opposite sign to the incident wavelet.

An increase of external pressure across the discontinuity strengthens the incident wavelet and produces a reflected wavelet whose sign depends upon whether $\mathscr{M} < 4$ or $\mathscr{M} > 4$. When $\mathscr{M} = 4$, there is no reflected wavelet.

The effects of a change in stiffness depend upon the relative magnitudes of $\mathscr{M}$ and $K_p\mathscr{P}/\rho c^2$.

When S is not small, (49) and (50) yield no simple, general rules concerning wave transmission and reflexion.

The foregoing remarks refer to the relative amplitudes of the pressure signals δp_I, δp_T and δp_R. The formulas for the ratios of velocity and area signals may be different, as shown by table 3 for the effects of δp_e only.

Remarks on second-order effects. In § 5 it was stated that, within the limits of the first-order linear theory, wavelets once generated would be transmitted across spatial jumps in δp_e without change of strength or reflexion. Moreover, the only fluid properties affecting the results were found to be ρ and c. We must now reconcile these facts with equations (49) and (50), which seem to contradict the statement on transmission and reflexion of wavelets, and which also contain the tube property $\mathscr{M}$.

In the development of (49) and (50), it is not assumed that quantities $\delta p_e/\rho c^2$, $\delta A_0/A_0$ and $\delta K_p/K_p$ are of the same order of magnitude as $\delta p_I/\rho c^2$. In a wholly linearized theory, however, they would necessarily be of the same order of magnitude. In that case both $(\delta p_T - \delta p_I)$ and δp_R would be of order $(\delta p_I)^2$. Thus they would be

Due to	$\left(\frac{\delta p_T - \delta p_I}{\delta p_I}\right)_{\max}$	$\left(\frac{\delta p_R}{\delta p_I}\right)_{\max}$
δp_e or A_0	$\frac{2-\mathscr{M}}{2\mathscr{M}}(1-S)$	$\frac{4-\mathscr{M}}{2\mathscr{M}}$
δK_p	$\left(\frac{2}{\mathscr{M}-2}\frac{\rho c^2}{K_p \mathscr{P}}-1\right)^{-1}$	$\frac{\mathscr{M}-4}{(1-S)}\left(\frac{2\rho c^2}{K_p \mathscr{P}}-\mathscr{M}+2\right)^{-1}$

TABLE 4

comprised of second-order terms not considered in the linearized theory of § 3. We also observe that, if second-order terms had been retained in the development of (9), (10) and (11), the tube property $\mathscr{M}$ would indeed have appeared.

Of what value then are equations (49) and (50)? If the spatial changes in A_0, K_p, and p_e are large, (49) and (50) do give a correct insight into the manner in which a particular small wavelet will be transmitted and reflected as it traverses these large changes. Thus these formulas provide an appropriate transition to the nonlinear theories of part 2. For instance, reflexions δp_R due to δp_e are seen to depend upon $\mathscr{M} \lesssim 4$, vanishing for $\mathscr{M} = 4$; and, if $S \ll 1$, the same is true for $(\delta p_T - \delta p_I)$. This explains findings that would be obscured in a purely numerical solution of nonlinear flows.

The case $S > 1$. Dealing with equations (45) and (46) in a similar manner, one gets the *same* formulas expressed by (49) and (50).

When $S \to \infty$, (49) and (50) go to the limiting forms

$$(\delta p_T - \delta p_I)/\delta p_I \to -[3(\mathscr{M}-2)/4](\delta A_0/A_0) + \tfrac{3}{4}\delta K_p/K_p$$

and

$$\delta p_R/\delta p_I \to [(\mathscr{M}-2)/4](\delta A_0/A_0) + \tfrac{1}{4}(\delta K_p/K_p).$$

The limit $S \to 1$. Both (49) and (50) appear to blow up when $S = 1$. However, the steady-state equation for dS^2/S^2 across the discontinuity (Shapiro 1977*b*) is given by (42) with added terms on the right in dA_0/A_0 and dK_p/K_p. As in § 8 when S approaches unity choking can be produced by excessively positive values of $-\mathscr{M}dA_0/A_0$ and $\delta K_p/K_p$ as well as of $\mathscr{M}\delta p_e/\rho c^2$. Invoking as before the limits implied by choking produces the maximum values of the transmission and reflexion ratios associated with δp_e, δA_0, and δK_p shown in table 4, when $S \cong 1$.

Thus, except for the reflexion due to δK_p, the effects are bounded as $S \to 1$. With regard to δK_p, it appears that a very small jump δK_p near $S = 1$ can produce a very large reflected wave, a result not readily explainable in physical terms.

Part 2. Nonlinear theory

We turn now to motions of large amplitude, subject to strong nonlinearities. Equations (6) and (7), which govern such flows, form a hyperbolic system. Consequently, characteristic curves exist which may be used as a basis for numerical solution. In what follows, we first discuss several analytical results of interest.

10. Exact solutions for area changing only with time

For practical reasons it may be advantageous to cause a tube to collapse uniformly with distance. Exact solutions for the velocity and external pressure may then be obtained.

Since α is considered now to depend only upon time, equation (6) may be simplified and then integrated once with respect to ξ at constant time. Assuming that the tube has a closed end at $\xi = 0$, where $\mathscr{U} = 0$, the result is

$$\frac{\mathscr{U}}{\xi} = -\frac{1}{\alpha}\frac{d\alpha}{d\tau} \equiv \beta(\tau), \tag{51}$$

from which it is seen that $\mathscr{U}$ varies linearly with ξ. Substitution of this into (7), with the friction term assumed negligible, leads to

$$-\frac{1}{\xi}\frac{\partial P_e}{\partial \xi} = \beta^2 + \frac{d\beta}{d\tau} = \Gamma(\tau). \tag{52}$$

Once $\alpha(\tau)$ has been prescribed, $\beta(\tau)$ and $\Gamma(\tau)$ are successively calculable. The external pressure distribution needed to achieve the prescribed $\alpha(\tau)$ is found by integration as

$$P_e = -\frac{\xi^2}{2}\Gamma(\tau) + G(\tau), \tag{53}$$

where $G(\tau)$ is determined physically by the value of P_e at one boundary, but has no effect on the solution as evidenced in (51) and (52).

These results were partially foreshadowed by linearized examples given in §§ 6 and 7.

Several exact solutions

An instantaneous pressure application. Let the pressure distribution of (53) be applied at $\tau = 0$ and held constant. Then $\Gamma(\tau) = \text{constant} = \theta^{-2}$. We set $G(\tau) = 0$ arbitrarily. Integration of (52) with the initial condition that $\mathscr{U} = 0$ at $\tau = 0$ yields the solution

$$\theta\beta = \theta\frac{\mathscr{U}}{\xi} = \frac{e^{2\tau/\theta} - 1}{e^{2\tau/\theta} + 1},$$

which gives the time variation of velocity shown in figure 22. Integration of (51), with the initial condition that $\alpha = 1$ at $\tau = 0$, gives the area ratio as a function of time,

$$\alpha = \frac{2e^{\tau/\theta}}{1 + e^{2\tau/\theta}},$$

which is also displayed in figure 22.

Linear variation of area with time. If we assume that α decreases linearly with time according to $\alpha = 1 - (\tau/T)$, then $\mathscr{U}/\xi = 1/(T-\tau)$ and $\Gamma(\tau) = 2/(T-\tau)^2$ in (53). The velocity and pressure gradient both go to infinity as $\tau \to T$.

Asymptotic ramp variation of area with time. If $\alpha(\tau)$ descends from $\alpha = 1$ to $\alpha = 0$ according to an asymptotic ramp given by $\alpha = (1 + k_1)/(1 + k_1 e^{\tau/\theta})$, then

$$\mathscr{U}/\xi = k_1 e^{\tau/\theta}/\theta(1 + k_1 e^{\tau/\theta})$$

and $\Gamma(\tau) = k_1 e^{\tau/\theta}/\theta^2(1 + k_1 e^{\tau/\theta})$. The velocity now only changes by the factor $(1 + k_1)/k_1$ from $\tau = 0$ to $\tau \to \infty$, and the pressure gradient by the same factor.

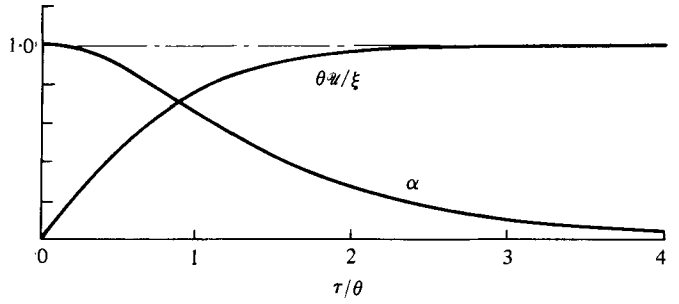

FIGURE 22. Velocity and area distributions for uniform collapse according to (52) with $\Gamma(\tau) = \text{constant} = \theta^{-2}$.

11. The characteristic curves

The solutions to the hyperbolic system comprising equations (6) and (7) contain curves on which the first derivatives of the dependent variables may be discontinuous. Formulated along these so-called characteristic curves, the partial differential equations are in effect transformed into ordinary differential equations, the equations of the characteristics.

Using well-known methods (e.g. Abbott 1966), the characteristic curves corresponding to (6) and (7) are found to be

$$\frac{d\xi}{d\tau} = \mathscr{U} \pm \left(\frac{K_p}{K_p^*}\right)^{\frac{1}{2}} \mathscr{C} \tag{54}$$

and

$$d\mathscr{U} \pm \left(\frac{K_p}{K_p^*}\right)^{\frac{1}{2}} \mathscr{C}\frac{d\alpha}{\alpha} + \mathscr{H}d\tau = 0, \tag{55a}$$

where

$$\mathscr{H} \equiv \frac{\partial P_e}{\partial \xi} + 2C_f \frac{L}{D_e}\mathscr{U}^2 \mp \left(\frac{K_p}{K_p^*}\right)^{\frac{1}{2}} \frac{Lq_L}{c_0^* A_0}\frac{\mathscr{C}}{\alpha} + \mathscr{P}\frac{d}{d\xi}\left(\frac{K_p}{\rho c_0^{*2}}\right) \pm \left(\frac{K_p}{K_p^*}\right)^{\frac{1}{2}} \mathscr{C}\mathscr{U}\frac{1}{A_0}\frac{dA_0}{d\xi}. \tag{55b}$$

The x, t trajectories defined by (54) represent signals that propagate in wave-like fashion, with speed $\pm c$ ($+$ for rightward moving, $-$ for leftward moving) with respect to the local fluid. Along these physical characteristics changes in state occur as determined by (55).

Equations (54) and (55) define two families of curves, the former in the 'physical' (ξ, τ) plane, the latter in the 'state' $(\mathscr{U}, \alpha)$ plane. The signs in the two equations correspond to the two families: upper sign for rightward moving, lower sign for leftward moving.

11.1. *Integration of the state characteristic for a uniform tube with* $\mathscr{H} = 0$

The state characteristics, equation (55), are coupled to the physical characteristics, equation (54), by reason of the term $\mathscr{H}$ and the non-uniformity in K_p. However, when $\mathscr{H} = 0$, the state characteristics are integrable wholly independently of the physical characteristics. These integrated state characteristics are useful even when $\mathscr{H}$ is not altogether negligible, as one may then bring in the missing term $\mathscr{H}d\tau$ by various *ad hoc* procedures, particularly in graphical solutions.

The $\mathscr{U},\alpha$ characteristics. The simplified state characteristics, with $\mathscr{H} = 0$ and $K_p/K_p^* = 1$, are given by integration of (55) as

$$\mathscr{U}_{\mathscr{R},\mathscr{L}} = \mp \int \frac{\mathscr{C}(\alpha)}{\alpha} d\alpha + \text{constant}. \tag{56}$$

Here the symbols $\mathscr{R}$ (for rightwards) and $\mathscr{L}$ (for leftwards) refer respectively to the upper and lower signs, and signify the directions of the physical characteristics described by (54).

Quadrature of (56), using the particular function $\mathscr{C}(\alpha)$ of figure 1, produces the curves of figure 23(*a*). Powerful nonlinearities and asymmetries are evident.

The $\mathscr{U},\mathscr{C}$ characteristics. Since $\mathscr{C} = \mathscr{C}(\alpha)$, the characteristic curves $\alpha(\mathscr{U})$ of figure 23(*a*) may be transformed to the characteristic curves $\mathscr{C}(\mathscr{U})$ of figure 23(*b*).

A 'simple' right-running compression wave (see § 12), each element of which propagates at speed $d\xi/d\tau = \mathscr{U} + \mathscr{C}$, will evidently steepen as it progresses if

$$(d\mathscr{C}/d\mathscr{U})_{\mathscr{L}} > -1$$

and will broaden if $(d\mathscr{C}/d\mathscr{U})_{\mathscr{L}} < -1$. The converse is true for a simple right-running rarefaction; it will steepen if $(d\mathscr{C}/d\mathscr{U})_{\mathscr{L}} < -1$ and will broaden if $(d\mathscr{C}/d\mathscr{U})_{\mathscr{L}} > -1$. The $\mathscr{L}$ curves of figure 23(*b*) have, for the most part, a slope $d\mathscr{C}/d\mathscr{U} > -1$; hence simple compression waves generally steepen, and simple rarefaction waves generally broaden. However, over a short segment of each $\mathscr{L}$ curve, $d\mathscr{C}/d\mathscr{U} < -1$, suggesting that the opposite behaviour may also occur.

The $\mathscr{U},\beta$ characteristics. If we introduce the variable $\beta(\alpha)$ through the definition

$$\beta(\alpha) \equiv \int_1^\alpha \frac{\mathscr{C}(\alpha)}{\alpha} d\alpha; \quad d\beta(\alpha) \equiv \frac{\mathscr{C}(\alpha)}{\alpha} d\alpha. \tag{57}$$

Then the $\mathscr{U},\beta$ state characteristics are the curves

$$d\mathscr{U}_{\mathscr{R},\mathscr{L}} = \mp d\beta; \quad \mathscr{U}_{\mathscr{R},\mathscr{L}} = \mp \beta + \text{constant}. \tag{58}$$

These plot as straight lines of slope ± 1, as in figure 23(*c*).

The latter shows on the abscissa scale the function $\mathscr{C}(\beta)$. This is related to the important tube-law property $\mathscr{M}$ (see figure 1) by

$$\frac{d\mathscr{C}(\alpha)}{d\beta(\alpha)} = \frac{\mathscr{M}(\alpha) - 2}{2}; \quad \mathscr{M}(\alpha) \equiv 3 + \alpha\mathscr{P}''(\alpha)/\mathscr{P}'(\alpha). \tag{59}$$

In § 12 it is shown that simple compression waves steepen if $\mathscr{M} > 0$ and broaden if $\mathscr{M} < 0$. The condition $\mathscr{M} = 0$ corresponds to $d\mathscr{C}/d\beta = -1$. Hence, referring to figure 23(*c*), a simple compression wave steepens where $d\beta/d\mathscr{C} > -1$ and broadens where $d\beta/d\mathscr{C} < -1$; and conversely for a simple rarefaction wave. In a narrow range of β below the point marked $\mathscr{M} = 0$, rarefaction waves steepen; outside this range, compression waves steepen.

12. Simple waves

We use the customary definition of a 'simple wave' (Whitham 1974) as a region of flow in which $\mathscr{U}$ is a function of α only. It may be shown that such flows exist only in regions where the tube is uniform and the term $\mathscr{H}$ in (55) is zero.†

† An exception is when α in (55) is a function of ξ alone plus a function of τ alone, but this is quite special and artificial.

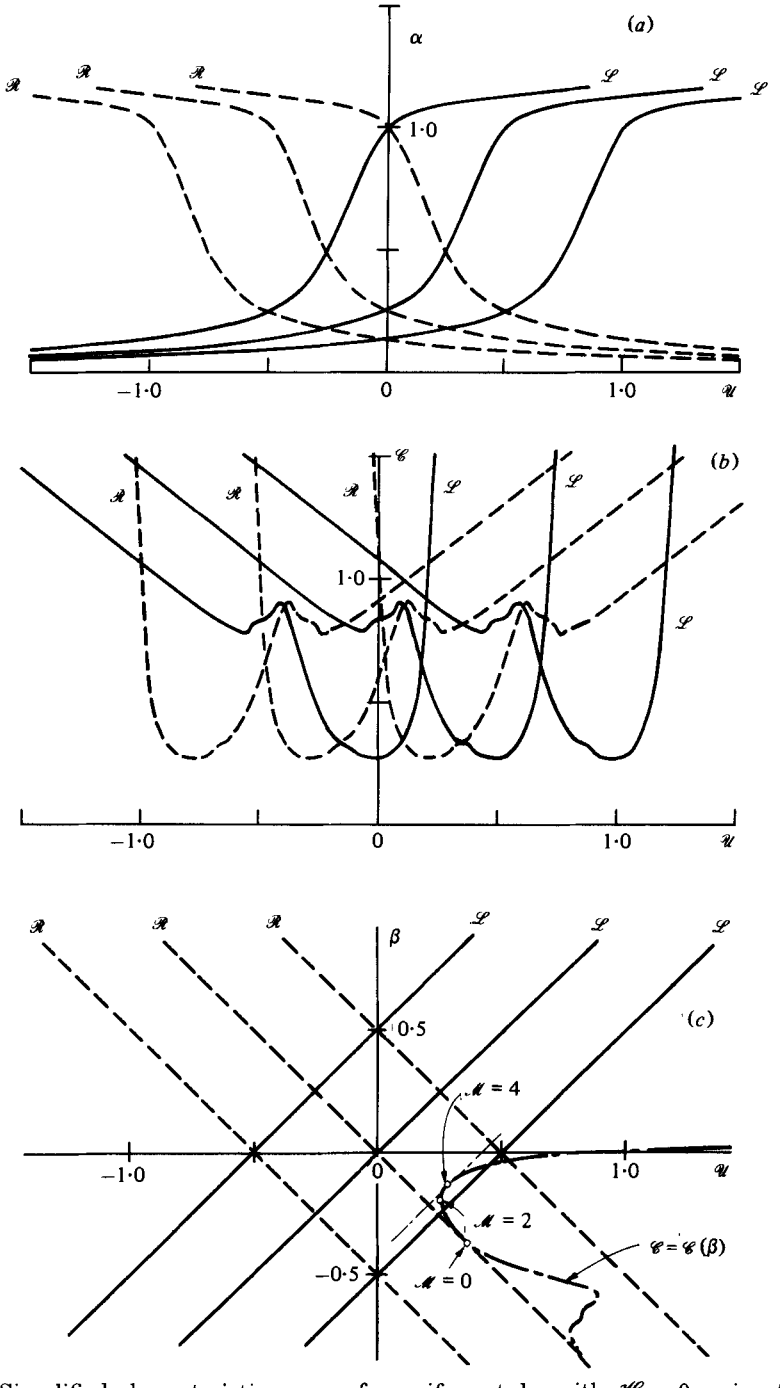

FIGURE 23. Simplified characteristic curves for uniform tube with $\mathscr{H} = 0$, using tube law of figure 1. (*a*) $\mathscr{U}, \alpha$ characteristics. (*b*) $\mathscr{U}, \mathscr{C}$ characteristics. (*c*) $\mathscr{U}, \beta$ characteristics. The dot–dash curve separates the sub- and supercritical zones.

12.1. *Relationships in a simple-wave region*

Limiting ourselves to such regions, the condition that $\mathscr{U} = \mathscr{U}(\alpha)$ allows us to write $\partial\mathscr{U}/\partial\xi = (d\mathscr{U}/d\alpha)(\partial\alpha/\partial\xi)$ and $\partial\mathscr{U}/\partial\tau = (d\mathscr{U}/d\alpha)(\partial\alpha/\partial\tau)$. Substitution of these into (6) produces

$$\frac{\partial\alpha}{\partial\tau} = -\left(\mathscr{U} + \alpha\frac{d\mathscr{U}}{d\alpha}\right)\frac{\partial\alpha}{\partial\xi},$$

while substitution into (7) yields

$$\frac{\partial\alpha}{\partial\tau} = -\left(\mathscr{U} + \frac{\mathscr{C}^2/\alpha}{d\mathscr{U}/d\alpha}\right)\frac{\partial\alpha}{\partial\xi}.$$

Division and simplification then gives

$$d\mathscr{U}/d\alpha = \pm\mathscr{C}/\alpha. \tag{60}$$

Putting this into one of the previous equations, we ge

$$(\mathscr{U} \pm \mathscr{C})\frac{\partial\alpha}{\partial\xi} + \frac{\partial\alpha}{\partial\tau} = 0.$$

Thus the curves of constant α and constant $\mathscr{C}(\alpha)$ (and, since it is a simple-wave region, of constant $\mathscr{U}$ as well) are defined by

$$\left(\frac{d\xi}{d\tau}\right)_{\alpha,\mathscr{C},\mathscr{U}} = -\frac{\partial\alpha/\partial\tau}{\partial\alpha/\partial\xi} = \mathscr{U} \pm \mathscr{C}. \tag{61}$$

12.2. *Physical interpretation of a simple wave*

Comparison of (60) and (61) with (54) and (55) shows that a simple wave of that physical family (e.g. $\mathscr{R}$) on which the state $\mathscr{U}, \alpha$ is constant is mapped on a state characteristic of opposite family (e.g. $\mathscr{L}$).

Thus, in a simple $\mathscr{R}$ wave, the properties $\mathscr{U}$, $\mathscr{C}$, α are constant on the *straight* lines $d\xi/d\tau = \mathscr{U} + \mathscr{C}$, and the changes of state from one such line to the next are connected by the plus sign in

$$d\mathscr{U} = \pm(\mathscr{C}/\alpha)\,d\alpha = \pm dP/\mathscr{C}. \tag{62}$$

An $\mathscr{L}$ simple wave propagates on the *straight* trajectories $d\xi/d\tau = \mathscr{U} - \mathscr{C}$, and (62), but with the minus sign, applies.

Physically, a simple wave represents a continuous train of pressure pulses propagating in a single direction, and without reflexion, at the speed $\pm c$ relative to the fluid. Each small element of the wave amplitude follows the linearized relationships [compare (62) with (34) and (35)]. A simple wave is most easily generated by excitation at one end of a very long tube, for example by injection or withdrawal of fluid, or by means of a piston. And, as will soon be seen, it may also be generated by the application of external pressure over a limited length of a long tube.

12.3. *Change in shape of a simple wave*

Consider a simple $\mathscr{R}$ wave (or a simple $\mathscr{L}$ wave viewed from the rear of the paper), and let the operator $\mathscr{D}/\mathscr{D}\tau$ signify the time rate of change while following the wave at the speed $\mathscr{U} + \mathscr{C}$. We may choose $\partial\mathscr{U}/\partial\xi$ (or, alternatively, $\partial\alpha/\partial\xi$ or $\partial P/\partial\xi$) as a

	$\mathscr{M} > 0$	$\mathscr{M} = 0$	$\mathscr{M} < 0$
Compressive waves	Steepen	Unchanged form	Broaden
Rarefaction waves	Broaden	Unchanged form	Steepen

TABLE 5

measure of the instantaneous steepness of the wave at a particular location. Steepening or broadening of the wave as it progresses is then determined by the sign of

$$\frac{\mathscr{D}}{\mathscr{D}\tau}\left(\frac{\partial \mathscr{U}}{\partial \xi}\right) = \frac{\partial}{\partial \tau}\left(\frac{\partial \mathscr{U}}{\partial \xi}\right) + (\mathscr{U} + \mathscr{C})\frac{\partial}{\partial \xi}\left(\frac{\partial \mathscr{U}}{\partial \xi}\right). \tag{63}$$

Now $(\partial/\partial\tau)(\partial\mathscr{U}/\partial\xi) = (\partial/\partial\xi)(\partial\mathscr{U}/\partial\tau)$ is calculable from the simplified version of (7). The term $\partial\alpha/\partial\xi$ in the latter may, for a simple $\mathscr{R}$ wave, be written as $(\alpha/\mathscr{C})(\partial\mathscr{U}/\partial\xi)$, in keeping with (62).

The ξ derivative of the third term of (7) introduces $\partial\mathscr{C}/\partial\xi$, which may be calculated as $\partial\mathscr{C}/\partial\xi = (d\mathscr{C}/d\alpha).(d\alpha/d\mathscr{U})(\partial\mathscr{U}/\partial\xi)$. By (62), $d\alpha/d\mathscr{U} = \alpha/\mathscr{C}$. Differentiation of (4) produces

$$\frac{d\mathscr{C}}{\mathscr{C}} = \frac{\mathscr{M}-2}{2}\cdot\frac{d\alpha}{\alpha}, \tag{64}$$

where $\mathscr{M}(\alpha)$ is given by (59). Thus we obtain $\partial\mathscr{C}/\partial\xi = \frac{1}{2}(\mathscr{M}-2)(\partial\mathscr{U}/\partial\xi)$.

Making the appropriate substitutions in (63), and simplifying, we finally get, for the simple $\mathscr{R}$ wave,

$$\frac{\mathscr{D}}{\mathscr{D}\tau}\left(\frac{\partial \mathscr{U}}{\partial \xi}\right) = -\frac{\mathscr{M}}{2}\left(\frac{\partial \mathscr{U}}{\partial \xi}\right)^2 \tag{65}$$

or, if the pressure rather than speed were considered,

$$\frac{\mathscr{D}}{\mathscr{D}\tau}\left(\frac{\partial P}{\partial \xi}\right) = -\frac{\mathscr{M}}{2\mathscr{C}}\left(\frac{\partial P}{\partial \xi}\right)^2. \tag{66}$$

A similar expression applies for $\partial\alpha/\partial\xi$.

Consider, for instance, a compressive $\mathscr{R}$ wave: in such, $\partial\mathscr{U}/\partial\xi$, $\partial P/\partial\xi$ and $\partial\alpha/\partial\xi$ are all negative. If $\mathscr{M} > 0$, they all become increasingly negative; thus the wave steepens. Following this line of thought, we may summarize as in table 5.

For $0{\cdot}5 \lesssim \alpha \lesssim 1{\cdot}1$, $\mathscr{M}$ has high positive values (figure 1). In the similarity range ($\alpha < 0{\cdot}21$), $\mathscr{M} = \frac{1}{2}$. The data of figure 1 suggests that $\mathscr{M}$ is negative over a narrow range of α, and this is confirmed by more recent data of exceptional accuracy (McClurken 1978). Does this result depend significantly upon the particular tube? This is difficult to answer conclusively because of the potential for large errors in calculating $\alpha\mathscr{P}''/\mathscr{P}'$ from experimental data.

Thus it appears that, with regard to the partially collapsed range, compressive waves in thin-walled compliant tubes for the most part steepen, but not always; and conversely for rarefaction waves. Whether the same is true of veins and arteries surrounded by tissue is at this stage not known.

12.4. *Simple-wave theory applied to collapse of a tube by a spatial step in external pressure*

We now reconsider the problem of a spatial step in external pressure, as in figures 4, 5 and 6, which previously was solved by the linearized theory. The nonlinearities

produce interesting effects that are vital to the understanding of the experimental results in part 3.

Let the tube be initially full and unpressurized, and the fluid motionless; that is, for $\tau < 0$: $\alpha = 1$ and $\mathscr{U} = 0$. Starting at $\tau = 0$, the time-varying external pressure $P_{e^-}(\tau)$ is applied uniformly over the region $\xi \leqslant 0$, while $P_{e^+}(\tau)$ remains at its original value in the region $\xi > 0$. At $\xi = 0$, the spatial step $P_{e^-}(\tau) - P_{e^+}(\tau)$ is a function of time.

The two simple-wave regions. Since $\mathscr{H}$ is zero except at $\xi = 0$, the regions on each side of the spatial pressure step may be treated by simple-wave theory, with appropriate matching conditions applied at the discontinuity. As shown in figure 24, a simple $\mathscr{R}$ compression wave increases the area, pressure, and velocity in the region $\xi > 0$; simultaneously, a simple $\mathscr{L}$ rarefaction wave increases the velocity but decreases the area and pressure in the region $\xi < 0$. Figure 24(*c*) shows the $\mathscr{R}$ wave mapped on the appropriate $\mathscr{L}$ characteristic of figure 23(*a*), and the $\mathscr{L}$ wave on the appropriate $\mathscr{R}$ characteristic, as determined by constants of integration corresponding to the initial state, namely $\mathscr{U} = 0$ and $\alpha = 1$.

If P_{e^-} is applied instantaneously, all the physical characteristics, or wavelets, originate at $\xi = 0$, $\tau = 0$, and each simple wave is *centred*.

Matching conditions at $\xi = 0$. Within the scope of this solution, the flow at the discontinuity is treated as quasi-steady and free of losses. Thus, conservation of volume flow and Bernoulli's theorem require that the product $\mathscr{U}\alpha$ and the sum $(P + P_e + \frac{1}{2}\mathscr{U}^2)$ be respectively the same at $\xi = \pm 0$.

The characteristic curves $\mathscr{U}(\alpha)$ of figure 24(*c*) are therefore replotted in the form $\mathscr{U}\alpha$ *vs.* α, which offers the advantage that corresponding states on either side of the discontinuity (e.g. $2R$ and $2L$, $3R$ and $3L$, etc.) are connected by a horizontal line. For each such pair of corresponding states, the associated value of $\mathscr{U}\alpha$, together with the constancy of $P + P_e + \frac{1}{2}\mathscr{U}^2$ and the tube law of figure 1, allows one to calculate the associated step in external pressure, $P_{e^-} - P_{e^+}$.

In this manner, starting at the condition $\alpha = 1$, the dimensionless flow $\mathscr{U}\alpha(0, \tau)$ may be determined as a function of the applied pressure $P_{e^-}(\tau)$, as in figure 24(*d*).

Flow limitation (*choking*). In figure 24(*c*), the two branches of the curve $\mathscr{U}\alpha(\alpha)$ for $\alpha < 1$ and $\alpha > 1$, respectively, exhibit a dramatic asymmetry, due to the powerful nonlinearity in the tube law.

In particular, the fact that the curve for $\alpha < 1$ has maxima and minima is of great practical importance with regard to choking, or flow limitation. At an extremum of $\mathscr{U}\alpha$ *vs.* α, we may write $d(\mathscr{U}\alpha)/d\alpha = 0$, whence it follows that $\alpha d\mathscr{U}/d\alpha + \mathscr{U} = 0$. But, writing (62) for an $\mathscr{L}$ wave, $d\mathscr{U}/d\alpha = -\mathscr{C}/\alpha$, we get $\mathscr{U} = \mathscr{C}$ at any extremum. Thus, quite independently of any particular tube law, the flow speed $\mathscr{U}$ equals the wave speed $\mathscr{C}$, and the characteristic curve of $\mathscr{U}(\alpha)$ for $\alpha < 1$ crosses the curve of $\mathscr{C}(\alpha)$, at exactly those values of α corresponding to extrema in the flow curve of figure 24(*c*). These correspond also to the locations in figure 24(*d*) where the curve of $(\mathscr{U}\alpha)_{\xi=0}$ *vs.* $P_{e^-}(\tau)$ doubles back onto itself.

Thus it appears that the flow rate becomes limited when left-running rarefaction waves propagating at the speed $\mathscr{U} - \mathscr{C}$ become trapped at the location where $\mathscr{U} = \mathscr{C}$. Of the two maxima in $\mathscr{U}\alpha$ in figure 24(*c*), only the first one, at $\alpha^* \cong 0{\cdot}44$, is physically meaningful. In figure 24(*d*), this corresponds to the first cusp at $P_{e^-} \cong 0{\cdot}32$.

Beyond this first occurrence of $\mathscr{U} = \mathscr{C}$, the solution as given fails: the succeeding $\mathscr{L}$

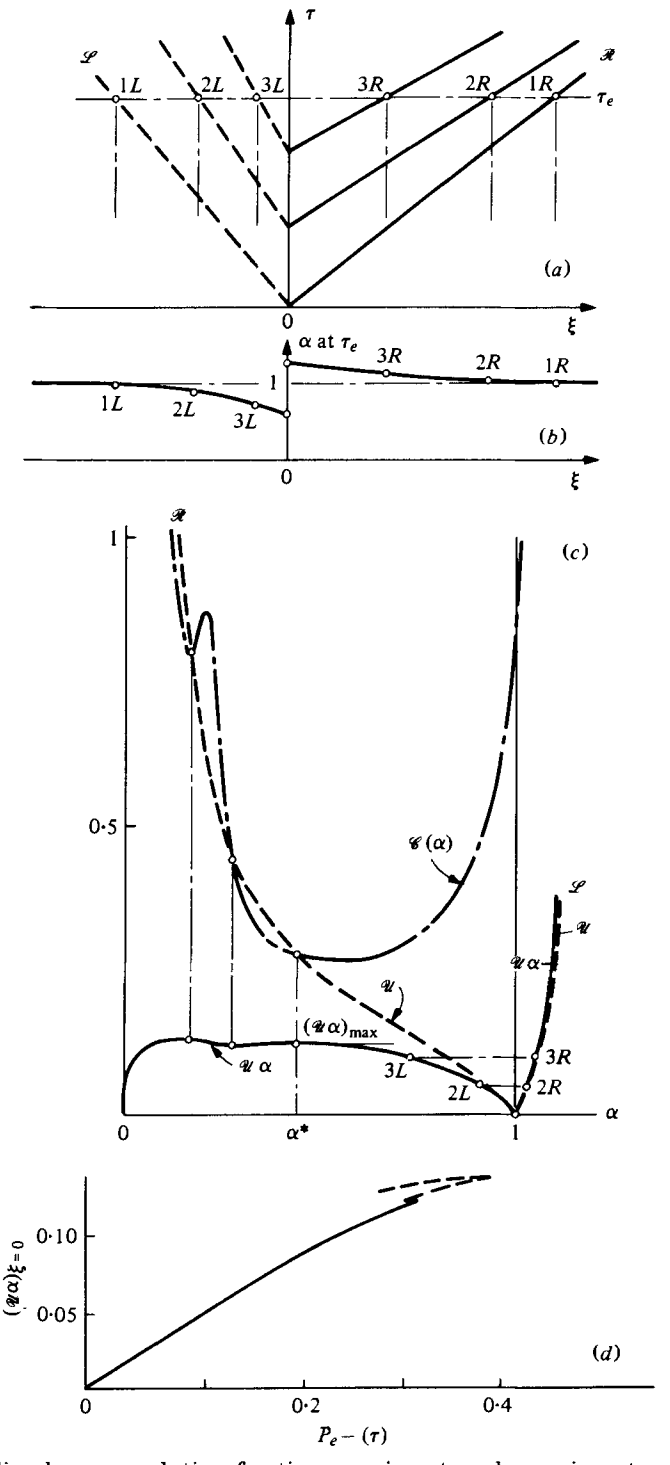

FIGURE 24. Simple-wave solution for time-varying step change in external pressure over the range $\xi \leqslant 0$. (*a*) ξ–τ wave diagram, showing $\mathscr{R}$ compression wavelets (solid lines) and $\mathscr{L}$ rarefaction wavelets (dashed lines). (*b*) Area distribution at the time τ_e. (*c*) Characteristic curves $\mathscr{U}(\alpha)$ from figure 23 (*a*) and corresponding curves of $\mathscr{U}\alpha$ *vs.* α. Also curve of $\mathscr{C}(\alpha)$ from figure 1. (*d*) Dimensionless flow at $\xi = 0$ as a function of applied external pressure. The dashed portions of the curve are physically meaningless.

waves generated at $\xi = -0$ can no longer propagate into the region $\xi < 0$, whereas the calculation assumes that the state at $\xi = -0$ is determined by the entire $\mathscr{L}$ wave.

Post-choking; shock-like transition. What happens physically when P_{e-} exceeds $\sim 0{\cdot}32$, at which condition $\mathscr{U}$ first reaches $\mathscr{C}$ and the flow $\mathscr{U}\alpha$ reaches the first maximum? The model as given requires that the flow at $\xi = +0$ have the now-fixed choked value of $\mathscr{U}\alpha$ as well as the Bernoulli constant at $\xi = -0$; it must also lie on the $\mathscr{L}$-state characteristic in figure 24(*c*). So stated, the problem is over defined: all these conditions cannot be met.

Some modification of the model is evidently required. This can presumably be in the form of a shock-like dissipative transition.

Imagine the discontinuity to have a small but finite width. The matching conditions previously specified for the step change in P_{e-} are now replaced by quasi-steady inviscid equations, with changes in state brought about by continuous changes in P_e (Shapiro 1977*b*). When the flow is just critical at the upstream end ($\xi = 0$) of what is now a short pressure ramp, the reduction in P_e along the ramp allows the downstream state ($\xi > 0$) to follow one of two paths: either subcritical or supercritical. If the external pressure P_{e-} is increased just beyond that necessary to attain critical velocity at $\xi = 0$, a supercritical path will be followed and a shock-like transition, involving a rapid area increase and velocity decrease will appear at an appropriate location. This can provide the adjustment, by way of energy dissipation due to flow separation, needed to match the downstream solution.

Such shock-like transitions for supercritical steady flow in collapsible tubes, occurring over a distance of the order of the tube diameter, have been observed, although there is as yet no fully satisfactory theory for either the shock structure or the trans-shock changes in state (Griffiths 1971*a*; Oates 1975; Shapiro 1977*b*; Dawson & Elliott 1977; Elliott & Dawson 1977; Kececioglu 1978).

The greater the external pressure, the larger the region of supercritical flow to be expected, and the stronger the shock. An analogous situation is the development of a shock, downstream of the throat, for gas flow through a Laval nozzle when the supply pressure is raised beyond a certain value while the exhaust-region pressure is maintained constant.

One is struck by certain similarities between the problem discussed above and a gasdynamics shock tube experiment. As in the collapsible tube following upon external compression, the flow in a shock tube is accelerated when the diaphragm is punctured; on the high pressure side by rarefaction waves propagating upstream and on the low pressure side by compression waves propagating downstream. In both cases a shock develops downstream at the leading edge of the compression wave. However, because the wave speed is monotonic in ρ for gasdynamic flows, the anomalous behaviour described above, producing a second shock close to the initial discontinuity, is not observed in the shock tube.

Further comments on the origin and development of a shock-like transition appear in § 13.

Practical interpretation of the results. Even before choking and its consequences occur, the discontinuities in all properties at the location of the pressure step (except for $u \ll c$, when the discontinuity in internal pressure is negligible) suggest other considerations in the interpretation of the results.

First, the tube law of figure 1 ignores what are now large effects due to bending

moments and membrane forces associated with axial tension and longitudinal curvature of the tube wall.

Second, even if one ignores the frictional stresses associated with high velocity at the throat formed at $\xi = -0$, one cannot dismiss what would surely be serious head losses due to separated flow in the rapid expansion of area.

While the model is for these reasons incorrect in detail, it surely indicates: (i) a tendency to form a throat that will ultimately be flow limiting; (ii) that large head losses will occur downstream of the throat in a region of continuous but rapid change; (iii) that, beyond a certain value of the applied external pressure, the rate of emptying cannot be further increased; and (iv) that, beyond this value, conditions downstream of the pressure step have no effect upstream of the throat.

We also observe that, because in general $\mathscr{M} > 0$, the compression wavelets in the region $\xi > 0$ are convergent, with the consequence that a shock-like structure will ultimately form there, as in the gasdynamic or free-surface analogue.

Finally, we remark that a *reduction* in the external pressure P_{e+}, in the downstream region $\xi > 0$, while maintaining constant the external pressure P_{e-} in the upstream region, $\xi < 0$, will produce results equivalent to those described.

12.5. *Application of simple wave theory to refilling of a collapsed tube*

Imagine a long tube in static equilibrium, the right-hand portion of which is partially collapsed by the external pressure P_{e+}. The latter is released, and the tube refills. We now improve upon the linearized solution of § 6.3 (see figure 17).

Instantaneous pressure release. Since $\partial P_e/\partial\xi = 0$ on both sides of $\xi = 0$, the instantaneous vanishing of P_{e+} results in two centred simple waves: an $\mathscr{R}$ compression (2 to $2c$) and an $\mathscr{L}$ rarefaction (1 to $1c$), as in figure 25.

The solution is shown as though both wave trains broaden rather than steepen. More likely, however, the compression wave propagating rightwards will have intersecting physical characteristics, and a shock-like transition will quickly form.

Disregarding this for the moment, the simple waves are of such strength as to remove the discontinuity in area at $\xi = 0$, without creating any discontinuity in velocity. Zone 3 is a finite region of uniform state. The latter is determined by equations (58) as follows: between zones 1 and 3, on an $\mathscr{R}$ characteristic, $\mathscr{U}_3 = -(\beta_3 - \beta_1)$; between zones 2 and 3, on an $\mathscr{L}$ characteristic, $\mathscr{U}_3 = \beta_3 - \beta_2$. Solving these, we get

$$\beta_3 = \tfrac{1}{2}(\beta_1 + \beta_2) \quad \text{and} \quad \mathscr{U}_3 = \tfrac{1}{2}(\beta_1 - \beta_2),$$

results which are evident graphically in figure 25 (*c*).

The magnitudes of the two area waves depend upon the tube law, $\mathscr{P}(\alpha)$, and the value of α_2. For a highly collapsed state 2, the right-running area wave is small, the left-running wave is very large. Conversely, for states 2 which are not so highly collapsed, the two area waves will be more comparable in magnitude.

If the $\mathscr{R}$ wave forms a shock-like transition, the wavelet system 2–2*a*–2*b*–2*c* would coalesce into a shock structure that progresses on a ξ, τ trajectory flatter than that of wavelet 2, that is, more rapidly. There is no reason, if β_2 is sufficiently small, for state 3 not to be supercritical; if this is so, wavelet $1c$ propagates rightwards.

Gradual release of pressure. Suppose now that P_{e+} is released only gradually. The situation is then somewhat comparable to that of figure 24. Simple waves are generated, as above, but now they are non-centred. Thus figure 25 (*b*) is modified, but

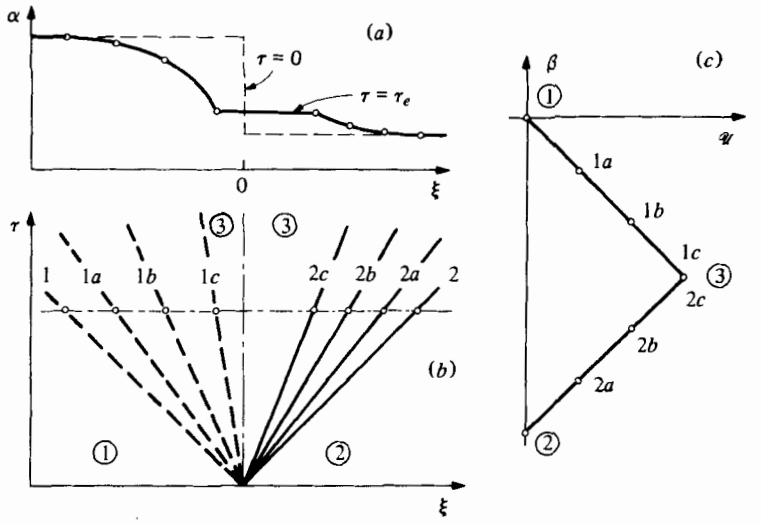

FIGURE 25. Refilling of a partially collapsed tube. (*a*) Area distributions at $\tau = 0$ and $\tau = \tau_e$. (*b*) Wave diagram in physical plane. (*c*) Solution in $\mathscr{U}, \beta$ state plane.

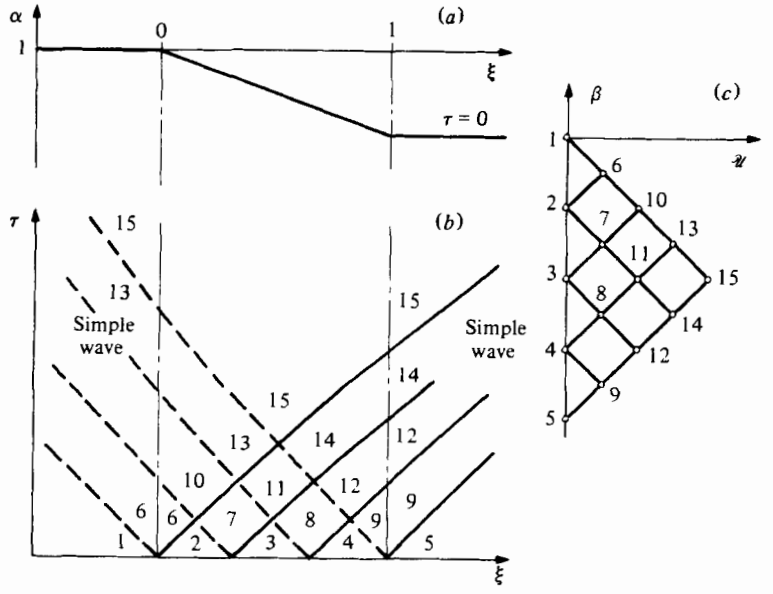

FIGURE 26. Refilling of a tube partially collapsed over a finite ramp length. (*a*) Area distribution at $\tau = 0$. (*b*) Wave diagram. (*c*) $\mathscr{U}, \beta$ state diagram.

figure 25 (*c*) remains unchanged. A shock presumably forms as the compression wavelets merge, but this occurs some distance downstream, rather than instantaneously. Until P_{e+} is reduced to zero, there exist at $\xi = 0$ discontinuities in area, velocity and pressure which are subject at each instant to the matching conditions, at $\xi = \pm 0$, of equal volume flow and equal Bernoulli constant.

Refilling of a linear area ramp. Figure 26 shows the solution for a linear ramp in area when the external pressure that maintained it is released instantaneously. Within the ramp region, waves of both families are present during a brief period, but

the final state 15 in the ramp region and beyond is uniform and identical with the final state for a step change in area (see figure 25). The waves emerging from the ramp region are simple waves.

13. Collapse of a tube by a ramp of external pressure

In the presence of an external pressure gradient $\partial P_e/\partial\xi$, or whenever $\mathscr{H}$ is not zero, it is usually necessary to construct the solution by numerical integration of the characteristic curves (54) and (55). However, if the gradient $\partial P_e/\partial\xi$ is constant, certain interesting and useful results fall out analytically, and quite independently of any particular tube law. Accordingly, we reconsider the linear ramp in $P_e(\xi)$ of figure 2(*a*), but now without the restriction of small amplitude.

Inasmuch as reflexions from boundaries are assumed not to occur, the problem as stated may be regarded as a model of the early stages of collapse near the edge region of a uniformly applied external pressure. That the edge region is here assumed linear rather than, say, S-shaped is probably of small consequence provided that we ignore pecularities due to the corners in $P_e(\xi)$.

This example also expands the details of the seeming discontinuity that inevitably appeared in the analysis of a spatial step in external pressure (§ 12.4 and figure 24), and of course it is physically more realistic.

13.1. *Formulation of the analysis*

Initially, the tube is at rest and the fluid motionless. At $\tau = 0$, therefore, $\mathscr{U} = 0$, $\alpha = 1$, $\mathscr{C} = 1$, and $\beta = 0$. Relative to its initial uniform value (which is conveniently called zero), the external pressure for $\tau \geqslant 0$ is given by: $P_e = 0$ for $\xi > 1$; $P_e = P_{e^-}(\tau)$ for $\xi < 0$; and $P_e = (1-\xi).P_{e^-}(\tau)$ for $0 < \xi < 1$. The gradient $\partial P_e/\partial\xi$ is zero outside the pressure ramp, i.e. for $\xi < 0$ and $\xi > 1$; within the ramp region, $0 < \xi < 1$, it is given by $-P_{e^-}(\tau)$.

For convenience later, we introduce the notation

$$\Pi^{(1)}(\tau) \equiv P_{e^-}(\tau); \quad \Pi^{(2)}(\tau) \equiv \int_0^\tau \Pi^{(1)}(\tau)\,d\tau; \quad \Pi^{(3)}(\tau) \equiv \int_0^\tau \Pi^{(2)}(\tau)\,d\tau. \tag{67}$$

Note that $\Pi^{(2)}$ and $\Pi^{(3)}$ have the character of pressure-impulse integrals.

We assume the tube to be uniform, and we neglect friction and tributary flows. In the ramp region, (54) and (55) now reduce to

$$(d\xi/d\tau)_{\mathscr{R},\mathscr{L}} = \mathscr{U} \pm \mathscr{C}(\alpha) \tag{68}$$

and

$$d\mathscr{U}_{\mathscr{R},\mathscr{L}} = \mp\, d\beta(\alpha) + d\Pi^{(2)}(\tau), \tag{69}$$

where in each case the upper sign goes with $\mathscr{R}$, and the lower sign with $\mathscr{L}$. Equations (68) and (69) also apply outside the ramp region, except that $d\Pi^{(2)}(\tau)$ is to be taken as zero.

13.2. *Graphical solution* (*figure* 27)

Given a particular pressurization function, the solution may be developed graphically by simultaneous construction of the physical and state characteristics (figures 27*a* and *b*). In the state diagram, the change along an $\mathscr{R}$ characteristic (or, respectively, an $\mathscr{L}$ characteristic) may be represented by a horizontal displacement of magnitude $\Delta\Pi^{(2)}$ followed by a displacement along a line of slope -1 (or, respectively, $+1$). For

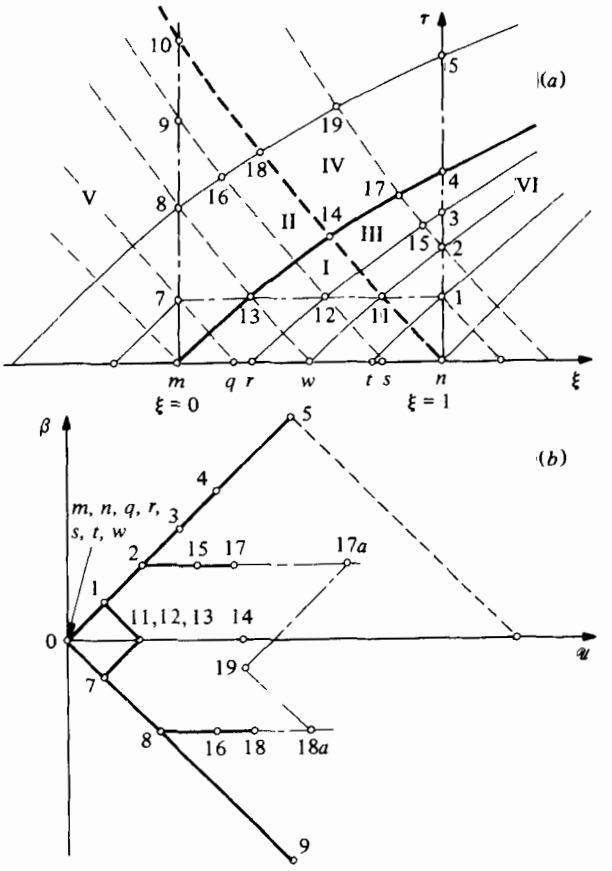

FIGURE 27. Collapse of a tube by a descending linear ramp of external pressure in the range $0 < \xi < 1$. (*a*) Wave diagram. Zone I: triangle *n*–14–*m*. Zone II: triangle *m*–14–10. Zone III: triangle *n*–4–14. Zone IV: bounded by $\xi = 0$, $\xi = 1$, 14–4, and 14–10. Zone V: region $\xi < 0$; $0 < \tau < \tau_{10}$. Zone VI: region $\xi > 1$; $0 < \tau < \tau_4$. (*b*) State diagram.

instance, to locate state 19 from states 17 and 18, one first lays off 17–17*a* equal to $\Pi_{19}^{(2)} - \Pi_{17}^{(2)}$ and 18–18*a* equal to $\Pi_{19}^{(2)} - \Pi_{18}^{(2)}$, and then finds the intersection point 19. The respective slopes in the physical diagram are given by the appropriate mean values of $\mathscr{U} \pm \mathscr{C}$.

13.3. *Results for an arbitrary tube law*

Outside the ramp: simple waves. For $\xi > 1$, in zone VI, a simple wave of compression propagates to the right, increasing $\mathscr{U}$, β and α. For $\xi < 1$, in zone V, a simple wave of rarefaction propagates to the left, also increasing $\mathscr{U}$ but decreasing β and α. These simple waves outside the ramp are similar to those that occur with the spatial step of pressure (figure 24). However, the physical characteristics have to be integrated through the ramp in order to establish the values of τ at the points $1, 2, \ldots, 9, 10$ from which the simple waves originate. This of course requires knowledge of the particular tube law and of the pressurization function.

Zone I. Consider a typical point 12 in this region. Noting that $\mathscr{U} = 0$ and $\beta = 0$ for *m*, *r*, *s* and *n*, (69), applied along *r*-12, gives $\mathscr{U}_{12} = -\beta_{12} + \Pi_{12}^{(2)}$; and, along *s*-12, $\mathscr{U}_{12} = \beta_{12} + \Pi_{12}^{(2)}$. Solved, these define the state at 12 as $\mathscr{U}_{12} = \Pi_{12}^{(2)}$ and $\beta_{12} = 0$.

Along a line of constant τ, therefore, say 11–12–13, the velocity is independent of ξ and the area is unaltered from its original value.

The entire zone I of figure 27 (*a*) is thus mapped onto the straight line from the origin to 14 in figure 27 (*b*).

Along a line of constant τ, e.g. 11–12–13, $\mathscr{U}$ and $\mathscr{C}$ are both constant. Consequently the wave slopes $(d\xi/d\tau)_{\mathscr{R},\mathscr{L}} = \mathscr{U} \pm \mathscr{C}$ are also constant. Thus the physical $\mathscr{R}$ characteristics in the triangle n–14–m are identical in form and parallel, displaced one from the other along the ξ axis; similarly so for the $\mathscr{L}$ characteristics. In zone I, therefore, waves can never intersect.

Employing the previous results, namely that $\mathscr{C} = 1$ and $\mathscr{U} = \Pi^{(2)}$, the equations of the two bounding characteristics of zone I may be integrated: $\xi_{13} = \tau_{13} + \Pi^{(3)}_{13}$; and $\xi_{11} = 1 - \tau_{11} + \Pi^{(3)}_{11}$. Simultaneous solution of these at the apex point 14 yields $\tau_{14} = \frac{1}{2}$ and $\xi_{14} = \frac{1}{2} + \Pi^{(3)}(\frac{1}{2})$.

The $\mathscr{L}$ characteristics become vertical when the flow speed reaches critical speed, $\mathscr{U} = \mathscr{C}$, that is, at the time defined by $\Pi^{(2)}(\tau) = 1$. This will occur somewhere within zone I only if the pressurization function is sufficiently large that $\Pi^{(2)}(\frac{1}{2}) \geqslant 1$.

If, however, $\Pi^{(2)}(\tau)$ is too large, the solution as described above may not be valid for one of two reasons. First, if $\Pi^{(3)}(\frac{1}{2}) > \frac{1}{2}$, $\mathscr{U} > \mathscr{C}$ and, also, point 14 moves outside the ramp; in that case the solution as given is valid in the region below the $\mathscr{R}$ characteristic that passes through the intersection with $\xi = 1$ of the $\mathscr{L}$ characteristic starting at point n. Second, two characteristic curves of the same family may intersect. When this occurs, the method of solution beyond the point of intersection must be modified as described later. If the intersection occurs between, for example, the $\mathscr{L}$ characteristic n–11–14 and its neighbour in zone III, point 14 will lie in a region of multi-valued solution.

The left-hand edge of the ramp, $\xi = 0$. Consider a typical point 8 at $\xi = 0$, such that $0 < \tau_8 < \tau_{10}$. Written for the $\mathscr{R}$ and $\mathscr{L}$ characteristics arriving at 8, (69) gives $\mathscr{U}_8 = -\beta_8$ and $\mathscr{U}_8 = \beta_8 + \Pi^{(2)}_8$, respectively. Solved, these yield $\mathscr{U}_8 = \frac{1}{2}\Pi^{(2)}_8$ and $\beta_8 = -\frac{1}{2}\Pi^{(2)}_8$. Assuming that $\Pi^{(2)}(\tau)$ increases monotonically, this shows that at $\xi = 0$ the velocity increases monotonically with time and the area decreases monotonically. For $0 < \tau < \tau_{14}$, the velocity at $\xi = 0$ (say at 7) is exactly half the velocity within zone I at the same instant of time (i.e. at 13, 12 and 11).

The line $\xi = 0$ in figure 27 (*a*) is mapped onto the $\mathscr{R}$ characteristic m–7–8–9 in figure 27 (*b*), which also represents all of the simple-wave region of zone V.

The right-hand edge of the ramp, $\xi = 1$. By a similar calculation, at any point on $\xi = 1$ where $\tau < \tau_4$, $\mathscr{U} = \frac{1}{2}\Pi^{(2)}$ and $\beta = \frac{1}{2}\Pi^{(2)}$. Thus both $\mathscr{U}$ and β increase monotonically with time, and are equal. For $0 < \tau < \tau_4$ (say at 1) the velocity is equal to the velocity at $\xi = 0$ at the same time (i.e. at 7) and is half the velocity within zone I at the same time (i.e. at 11, 12 and 13). The increase of β at 1 equals the decrease at 7, but the area changes may be quite different because of the nonlinearity of the curve $\alpha(\beta)$.

The line $\xi = 1$ in figure 27 (*a*) maps onto the $\mathscr{L}$ characteristic n–1–2–3–4–5 in figure 27 (*b*), which also represents the entire simple-wave region of zone VI.

Flow limitation. If the pressurization function $\Pi^{(1)}$ is sufficiently intense to produce supercritical speed, this will presumably occur first in the upstream portion of the pressure ramp.

Neglecting peculiarities associated with the corner in $P_e(\xi)$ at $\xi = 0$, the wave

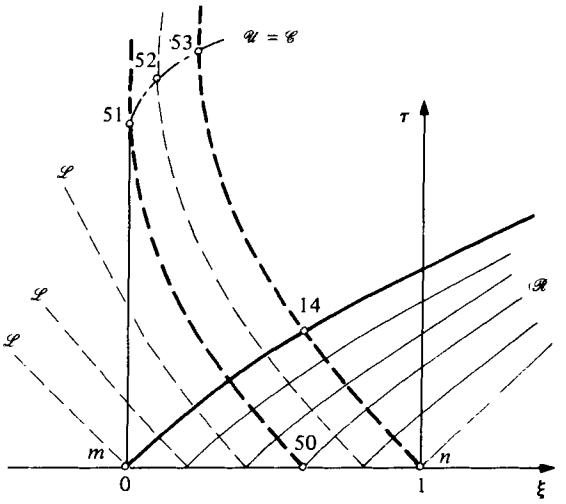

FIGURE 28. Wave diagram of figure 27(*b*) when critical speed $\mathscr{U} = \mathscr{C}$ is reached at $\xi = 0, \tau = \tau_{51}$.

diagram would then be as in figure 28. Critical speed, $\mathscr{U} = \mathscr{C}$, as shown, first occurs at point 51, and curve 51–52–53 is the boundary between the zones of subcritical and supercritical speed. Above this curve, the $\mathscr{R}$ characteristics, as well as the $\mathscr{L}$ characteristics, have positive slopes.

Once the flow has reached critical velocity at $\xi = 0$, $\mathscr{L}$-rarefaction waves can no longer accelerate the flow there. Since the flow velocity in zone V cannot become supercritical for the reasons given in § 12, the flow at $\xi = 0$ remains exactly critical. The velocity, area and flow rate at $\xi = 0$ then correspond precisely to the conditions at α^* in figure 24(*c*). As a result, the $\mathscr{L}$ characteristic 50–51 remains vertical above τ_{51}. However, within the ramp region, $\mathscr{R}$ compression waves may in fact accelerate the fluid to supercritical speeds, contrary to the view often expressed that there is no way of exceeding the critical speed. Thus the flow inside the pressure ramp or even emerging from the ramp may be supercritical. But if any increase of flow rate, beyond the value of $(\mathscr{U}\alpha)_{\max}$ in figure 24(*c*), occurs downstream of the ramp, it is only by reason of the more rapid collapse within the ramp region itself, since the rate of collapse upstream of the ramp is no longer affected by the pressurization, no matter how large the latter may be.

Typical results. Figure 29 shows schematically the distributions of area and velocity at various times for the wave diagram of figure 28, in which supercritical speeds are reached. After the time τ_{51}, the flow at the upstream end of the ramp is choked, and remains unchanged.

13.4. *Development of shock-like transitions*

We must now inquire whether, in the solutions presented, physical characteristics of the same family can intersect. Should this happen, the mathematical solution would produce multi-valued fluid properties, a physical impossibility. Presumably, as in gasdynamics, a shock-like transition would then appear.

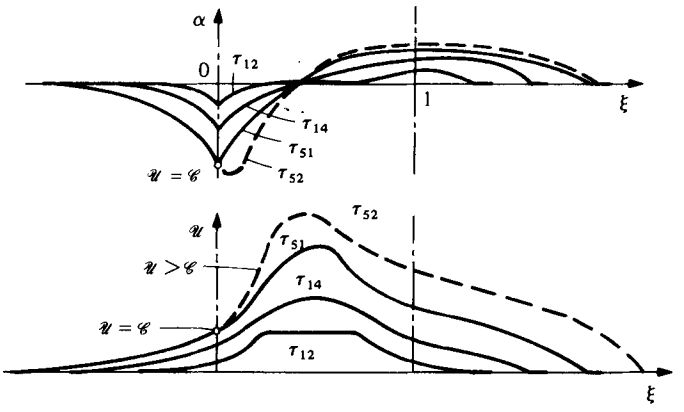

FIGURE 29. Schematic profiles of area and velocity corresponding to figure 28.

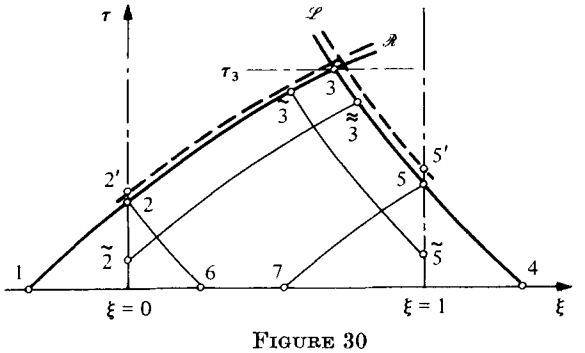

FIGURE 30

Outside the ramp. Assuming that $\mathscr{M} > 0$, the simple compression wave system downstream of the ramp will steepen and form a shock. Upstream of the ramp, again with $\mathscr{M} > 0$, the simple rarefaction wave system will broaden rather than steepen; thus no shock will form.

Inside the ramp. We have already shown that neither the $\mathscr{R}$ waves nor the $\mathscr{L}$ waves that originate at $\tau = 0$ inside the ramp region intersect within zone I of figure 27 (*a*).

What remains to be considered then is the situation of figure 30. Here either the $\mathscr{L}$ characteristic 4–5–3, or the $\mathscr{R}$ characteristic 1–2–3, or both, intersecting at (ξ_3, τ_3), originate at $\tau = 0$ outside the ramp. Equations (69), written respectively along $\mathscr{R}$ and $\mathscr{L}$, give $\mathscr{U}_3 = -\beta_3 + \Pi_3^{(2)} - \Pi_2^{(2)}$; and $\mathscr{U}_3 = \beta_3 + \Pi_3^{(2)} - \Pi_5^{(2)}$. Addition and subtraction of these yield

$$\mathscr{U}_3 = \Pi_3^{(2)} - \tfrac{1}{2}\Pi_2^{(2)} - \tfrac{1}{2}\Pi_5^{(2)} \tag{70a}$$

and

$$\beta_3 = \tfrac{1}{2}\Pi_5^{(2)} - \tfrac{1}{2}\Pi_2^{(2)}. \tag{70b}$$

Intersection of $\mathscr{R}$ waves. Consider the $\mathscr{R}$ wave passing through the fixed point 2. The slope of $\mathscr{R}$ at any point 3, within the range $0 < \xi < 1$, is given by

$$\left(\frac{d\xi_{\tilde{3}}}{d\tau}\right)_{\mathscr{R}} = \mathscr{U}_{\tilde{3}} + \mathscr{C}_{\tilde{3}} = \Pi_{\tilde{3}}^{(2)} - \tfrac{1}{2}\Pi_2^{(2)} - \tfrac{1}{2}\Pi_{\tilde{5}}^{(2)} + \mathscr{C}(\beta_{\tilde{3}}). \tag{71}$$

Point $\tilde{5}$ is located at the intersection of the $\mathscr{L}$ wave passing through $\tilde{3}$ with either the line $\tau = 0$ or the line $\xi = 1$. Note that, if $\tilde{5}$ lies on $\tau = 0$, $\Pi_{\tilde{5}}^{(2)} = 0$.

Integration of (71) along $\mathscr{R}$, from τ_2 to τ_3, produces

$$\xi_3 = \Pi_3^{(3)} - \Pi_2^{(3)} - \tfrac{1}{2}(\tau_3 - \tau_2)\,\Pi_2^{(2)} + \int_{\tau_2}^{\tau_3} [\mathscr{C}(\beta_{\tilde{3}}) - \tfrac{1}{2}\Pi_{\tilde{5}}^{(2)}]\, d\tau_{\tilde{3}}. \tag{72}$$

Now, considering a neighbouring $\mathscr{R}$ characteristic passing through point 2′, we shall form the derivative $(\partial\xi_3/\partial\tau_2)_{\tau_3=\text{const.}}$. This is the ratio of the horizontal spacing between the neighbouring curves at any time τ_3 to the vertical spacing at $\xi = 0$; should this derivative vanish, neighbouring $\mathscr{R}$ characteristics passing through 2 intersect at the time τ_3. Differentiation of (72) gives

$$\left(\frac{\partial\xi_3}{\partial\tau_2}\right)_{\tau_3} = -\frac{d\Pi_2^{(3)}}{d\tau_2} - \tfrac{1}{2}(\tau_3 - \tau_2)\frac{d\Pi_2^{(2)}}{d\tau_2} + \tfrac{1}{2}\Pi_2^{(2)} - \mathscr{C}(\beta_2) + \tfrac{1}{2}\Pi_6^{(2)} + \int_{\tau_2}^{\tau_3}\left[\frac{\partial\mathscr{C}(\beta_{\tilde{3}})}{\partial\tau_2}\right]_{\tau_{\tilde{3}}} d\tau_{\tilde{3}} - \frac{1}{2}\int_{\tau_2}^{\tau_3}\left[\frac{\partial\Pi_{\tilde{5}}^{(2)}}{\partial\tau_2}\right]_{\tau_{\tilde{3}}} d\tau_{\tilde{3}}. \tag{73}$$

From (67), we see that $d\Pi_2^{(3)}/d\tau_2 = \Pi_2^{(2)}$, and that $d\Pi_2^{(2)}/d\tau_2 = \Pi_2^{(1)}$. Using (59) and (70), we form

$$\left[\frac{\partial\mathscr{C}(\beta_{\tilde{3}})}{\partial\tau_2}\right]_{\tau_{\tilde{3}}} = \left(\frac{d\mathscr{C}}{d\beta}\right)_{\tau_{\tilde{3}}} \cdot \left(\frac{\partial\beta_3}{\partial\tau_2}\right)_{\tau_{\tilde{3}}} = \frac{\mathscr{M}_{\tilde{3}} - 2}{4}\left[\left(\frac{\partial\Pi_{\tilde{5}}^{(2)}}{\partial\tau_2}\right)_{\tau_{\tilde{3}}} - \frac{d\Pi_2^{(2)}}{d\tau_2}\right].$$

Integrating this along $\mathscr{R}$, we obtain the approximation

$$\int_{\tau_2}^{\tau_3}\left[\frac{\partial\mathscr{C}(\beta_{\tilde{3}})}{\partial\tau_2}\right]_{\tau_{\tilde{3}}} d\tau_{\tilde{3}} \cong \frac{2 - \bar{\mathscr{M}}}{4}(\tau_3 - \tau_2)\,\Pi_2^{(1)} + \frac{\bar{\mathscr{M}} - 2}{4}\int_{\tau_2}^{\tau_3}\left[\frac{\partial\Pi_{\tilde{5}}^{(2)}}{\partial\tau_2}\right]_{\tau_{\tilde{3}}} d\tau_{\tilde{3}},$$

where $\bar{\mathscr{M}}$ is now some reasonably selected mean value within the interval 2–3. The last term of (73) may be written as

$$\left[\frac{\partial\Pi_{\tilde{5}}^{(2)}}{\partial\tau_2}\right]_{\tau_{\tilde{3}}} = \frac{d\Pi_{\tilde{5}}^{(2)}}{d\tau_{\tilde{5}}} \cdot \left(\frac{\partial\tau_{\tilde{5}}}{\partial\tau_2}\right)_{\tau_{\tilde{3}}} = \Pi_{\tilde{5}}^{(1)}\left(\frac{\partial\tau_{\tilde{5}}}{\partial\tau_2}\right)_{\tau_{\tilde{3}}}.$$

Inserting these several terms into (73), and setting the left-hand side equal to zero, we may solve approximately for the time $\tau_{3\mathscr{R}}^*$ at which neighbouring curves passing through 2 will intersect:

$$\tau_{3\mathscr{R}}^* - \tau_2 \cong \frac{-4}{\bar{\mathscr{M}}\Pi_2^{(1)}}\left[\mathscr{C}_2(\beta_2) + \tfrac{1}{2}\Pi_2^{(2)} - \tfrac{1}{2}\Pi_6^{(2)} - \frac{\bar{\mathscr{M}} - 4}{4}\int_{\tau_2}^{\tau_{3\mathscr{R}}^*}\left(\frac{\partial\tau_{\tilde{5}}}{\partial\tau_2}\right)_{\tau_{\tilde{3}}} \cdot \Pi_{\tilde{5}}^{(1)}\, d\tau_{\tilde{3}}\right].$$

Inspection of (71) for the condition that 3 coincides with 2 shows that the result just given may be expressed more effectively as

$$\tau_{3\mathscr{R}}^* - \tau_2 \cong \frac{-4}{\bar{\mathscr{M}}\Pi_2^{(1)}}\left[\left(\frac{\partial\xi}{\partial\tau}\right)_{\mathscr{R},2} - \frac{\bar{\mathscr{M}} - 4}{4}\int_{\tau_2}^{\tau_{3\mathscr{R}}^*}\left(\frac{\partial\tau_{\tilde{5}}}{\partial\tau_2}\right)_{\tau_{\tilde{3}}} \cdot \Pi_{\tilde{5}}^{(1)}\, d\tau_{\tilde{3}}\right], \tag{74}$$

where $(d\xi/d\tau)_{\mathscr{R},2}$ is the slope of $\mathscr{R}$ at 2.

Here it is interesting to observe the presence of the term $\bar{\mathscr{M}}$, the sign of which determines steepening or broadening of simple waves (§ 12); and the term $(\bar{\mathscr{M}} - 4)$, the sign of which determines the nature of wave transmission and reflexion in a gradient of external pressure (§ 9).

Equation (74) is unfortunately not explicit in $\tau^*_{3\mathscr{R}}$ because the integral depends upon $\tau^*_{3\mathscr{R}}$. If however, point 4 originates inside the ramp, $\Pi^{(1)}_{\tilde{5}} = 0$; furthermore, according to (70*b*), $\beta_3 = \beta_2$; thus $\bar{\mathscr{M}} = \mathscr{M}_2$. Accordingly, (74) reduces to

$$\tau^*_{3\mathscr{R}} - \tau_2 \cong \frac{-4}{\mathscr{M}_2 \Pi^{(1)}_2} \left(\frac{d\xi}{d\tau}\right)_{\mathscr{R},2}. \tag{75}$$

In these equations, $(d\xi/d\tau)_{\mathscr{R},2} > 0$, $\Pi^{(1)}_2 > 0$ and $\Pi^{(1)}_{\tilde{5}} > 0$; but $(\partial\tau_{\tilde{5}}/\partial\tau_2)_{\tau_{\tilde{3}}} < 0$, as may be seen from figure 30.

Intersections in zone II. If $\mathscr{M} > 0$, (75) indicates that $(\tau^*_{3\mathscr{R}} - \tau_2) < 0$, a result that is physically meaningless in the context of this analysis. The appropriate interpretation is that, since $(\tau^*_{3\mathscr{R}} - \tau_2)$ is not positive, compression $\mathscr{R}$ waves starting on the line m–10 of figure 27 (*a*) do not intersect within zone II.

Previously we found that, for $\mathscr{M} > 0$, a simple compression wave tends to form intersecting characteristics. The present result therefore implies that the rarefaction $\mathscr{L}$ waves in this flow so interact with the compression $\mathscr{R}$ waves as to inhibit the latter from steepening within zone II, even though $\mathscr{M} > 0$.

When $\mathscr{M} < 0$, on the other hand, intersections do tend to occur in zone II.

Intersections in zone IV. The term $\frac{1}{4}(\mathscr{M} - 4)$ multiplying the integral in (74) vanishes for $\mathscr{M} = 4$, as do reflexions produced by the gradient $\partial p_e/\partial x$. Thus this term presumably represents the effects on $\mathscr{R}$ waves of reflexions from $\mathscr{L}$ waves.

Inspection of (74) shows that, when $\bar{\mathscr{M}} > 4$, $\mathscr{R}$ waves do not intersect in zone IV. When $\mathscr{M} < 4$, it is ambiguous whether such intersections occur, except that, when $\mathscr{M} \cong 0$, any tendency to intersect would be delayed until the $\mathscr{R}$ waves have passed out of zone IV.

Intersection of $\mathscr{L}$ waves. A parallel analysis for the $\mathscr{L}$ wave of figure 30 gives the following expression for the time $\tau^*_{3\mathscr{L}}$ at which neighbouring $\mathscr{L}$ waves passing through point 5 will intersect:

$$\tau^*_{3\mathscr{L}} - \tau_5 \cong \frac{4}{\bar{\mathscr{M}} \Pi^{(1)}_5} \left[-\left(\frac{d\xi}{d\tau}\right)_{\mathscr{L},5} + \frac{\bar{\mathscr{M}} - 4}{4} \int_{\tau_5}^{\tau^*_{3\mathscr{L}}} \Pi^{(1)}_2 \left(\frac{\partial\tau_{\tilde{2}}}{\partial\tau_5}\right)_{\tau_{\tilde{3}}} d\tau_{\tilde{3}} \right]. \tag{76}$$

Here, point $\tilde{2}$ is located at the intersection of the $\mathscr{R}$ wave passing through either $\tau = 0$ or $\xi = 0$ and a point $\tilde{3}$ located along the line 5–3.

If point 1 originates inside the ramp, (74) becomes explicit for $\tau^*_{3\mathscr{L}}$, since $\Pi^{(1)}_2 = 0$ and $\mathscr{M} = \mathscr{M}_5$. It reduces to

$$\tau^*_{3\mathscr{L}} - \tau_5 \cong \frac{4}{\mathscr{M}_5 \Pi^{(1)}_5} \left(-\frac{d\xi}{d\tau}\right)_{\mathscr{L},5}. \tag{77}$$

In these equations $(-d\xi/d\tau)_{\mathscr{L},5} > 0$, $\Pi^{(1)}_5 > 0$, and $\Pi^{(1)}_{\tilde{2}} > 0$; but $(d\tau_{\tilde{2}}/d\tau_5)_{\tau_{\tilde{3}}} < 0$.

Intersections in zone III. Here equation (77) is applicable. Thus, if $\mathscr{M} > 0$, intersections are possible; if $\mathscr{M} < 0$, intersections cannot occur; and, if $\mathscr{M} \cong 0$, any tendency to intersect would be delayed until the $\mathscr{L}$ waves have passed out of zone III.

The fact that it is rarefaction waves that tend to intersect for $\mathscr{M} > 0$ is curious, since a simple rarefaction wave would broaden. Presumably this signifies the importance of the interaction with the compressive $\mathscr{R}$ waves to the tendency of steepening or broadening.

Intersections in zone IV. Inspection of (76) shows that: (*a*) when $\mathscr{M} > 4$, intersections are ambiguous; (*b*) when $0 < \mathscr{M} \leqslant 4$, there is a tendency for intersections to occur;

(*c*) when $\mathscr{M} < 0$, intersections do not occur; (*d*) when $\mathscr{M} \cong 0$, any tendency to intersect would be delayed until the $\mathscr{L}$ waves passed out of zone IV.

When, in any of the foregoing instances, there is a tendency for intersections to appear, they occur more rapidly as the intensity of the pressurization function $\Pi^{(1}$ is increased, owing to the greater strengths of the wave systems and the concomitantly greater nonlinearities.

13.5. *Results for constant applied pressure using a simple tube law*

Several generalities mentioned above are further illuminated by the calculations below for a specific tube law and schedule of pressurization.

Pressurization function. We assume that the applied pressure is constant and applied instantaneously. Thus, for $\tau \geqslant 0$, $P_{e-} = P_e^* = \text{constant}$; $\Pi^{(1)}(\tau) = P_e^*$; $\Pi^{(2)}(\tau) = P_e^* \tau$; and $\Pi^{(3)}(\tau) = \frac{1}{2} P_e^* \tau^2$.

Tube law. As a compromise between a realistic representation and one that results in mathematical transparency, we select the function $\mathscr{P} \equiv \frac{1}{2}(\alpha^2 - 1)$. The associated variables are then: $\mathscr{C} = \alpha$; $\beta = \alpha - 1$; and $\mathscr{M} = 4$. Note that this value of $\mathscr{M}$ implies that wavelets do not reflect and that simple compression waves steepen.

Solution. Table 6 displays results obtained in a straightforward manner by inserting these particulars into the general formulas developed previously. It has been assumed for table 6 that the wave diagram has the general form of figure 27 (*a*); for this it is sufficient but not necessary that the flow be everywhere subcritical.

In zone I, the dimensionless flow rate is $\mathscr{U}\alpha = P_e^* \tau$, increasing linearly with time up to $\tau_{14} = \frac{1}{2}$.

In zone IV, both $\mathscr{U}$ and α become wholly independent of time, varying only with ξ. Beyond τ_{10}, therefore, the segment within the ramp region, $0 \leqslant \xi \leqslant 1$, behaves like a *rigid* tube in which there is a *steady* flow that merely transfers fluid from $\xi < 0$ to $\xi > 1$. In accord with this, the flow rate proves to be $\mathscr{U}\alpha = \frac{1}{2} P_e^*$, i.e. it is a constant, varying neither with time nor distance. For a tube law which permits wave reflexions, this would not necessarily be the case, but presumably an approximation to this condition would prevail for large τ.

Choking. At $\xi = 0$, $\mathscr{U}$ increases linearly with time up to $\tau_{10} = [1 - (1 - 2P_e^*)^{\frac{1}{2}}]/P_e$, and subsequently remains constant at the value $(\mathscr{U})_{\xi=0, \tau>\tau_{10}} = \frac{1}{2}[1 - (1 - 2P_e^*)^{\frac{1}{2}}]$.

If P_e^* reaches the value $\frac{1}{2}$, however, the critical condition $\mathscr{U}_{10} = \mathscr{C}_{10} = \frac{1}{2}$ occurs at $\tau_{10} = 2$. The $\mathscr{L}$ characteristic at 10 then has a vertical slope. For $P_e^* > \frac{1}{2}$, the $\mathscr{L}$ characteristic n–14 would turn rightwards even before reaching $\xi = 0$, producing the situation of figure 28. The solution of table 6 is then valid only up to the $\mathscr{R}$ characteristic which intersects, at $\xi = 0$, the $\mathscr{L}$ characteristic 50–51. The formation of shock-like transitions, discussed below, might further restrict this solution.

If $P_e^* > \frac{1}{2}$, the flow at $\xi = 0$ and in zone V becomes independent of events downstream beyond the time τ_{51}, for then $\mathscr{L}$ waves no longer propagate upstream. From table 6, the dimensionless flow at $\xi = 0$ up to the critical condition is given by

$$(\mathscr{U}\alpha)_{\xi=0} = \alpha(1 - \alpha).$$

This has a maximum value (the choking flow rate of figure 24*c*), namely $(\mathscr{U}\alpha)_{\max} = \frac{1}{4}$, which is first reached at the conditions given previously and which then remains constant until other effects begin to influence the solution.

Zone	$\mathscr{U}$	$\alpha = \mathscr{C} = 1+\beta$
I	$P_e^*\tau$	1
II	$\frac{1}{2}[P_e^*\tau - 1 + \sqrt{(1+2P_e^*\xi)}]$	$\frac{1}{2}[1 - P_e^*\tau + \sqrt{(1+2P_e^*\xi)}]$
III	$\frac{1}{2}[P_e^*\tau + 1 - \sqrt{(1-2P_e^*(1-\xi))}]$	$\frac{1}{2}[P_e^*\tau + 1 + \sqrt{(1-2P_e^*(1-\xi))}]$
IV	$\frac{1}{2}[\sqrt{(1+2P_e^*\xi)} - \sqrt{(1+2P_e^*(\xi-1))}]$	$\frac{1}{2}[\sqrt{(1+2P_e^*\xi)} + \sqrt{(1+2P_e^*(\xi-1))}]$
V (at $\xi = 0$)	$\frac{1}{2}P_e^*\tau$	$1 - \frac{1}{2}P_e^*\tau$
VI (at $\xi = 1$)	$\frac{1}{2}P_e^*\tau$	$1 + \frac{1}{2}P_e^*\tau$

TABLE 6. Solution for figure 27 with $P_{e-} = P_e^*$ and $\mathscr{P} = \frac{1}{2}(\alpha^2 - 1)$.

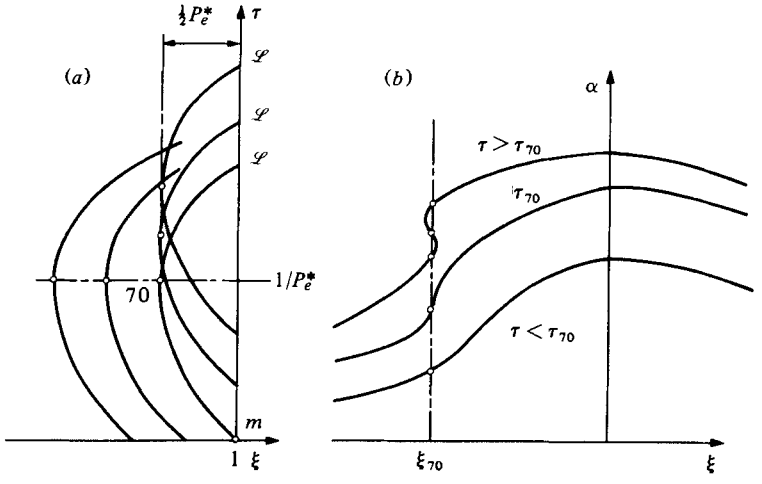

FIGURE 31. Intersecting $\mathscr{L}$ characteristics in zone III when $P_e^* > 2$. (*a*) Wave diagram near $\xi = 1$. (*b*) Schematic of area profiles near the time τ_{70} of intersection of $\mathscr{L}$ waves.

Intersection of characteristics at high pressurization. Applying the formulas for $\mathscr{U}$ and $\mathscr{C}$ in table 6 to (68), one may readily integrate ξ, τ trajectories of the $\mathscr{R}$ and $\mathscr{L}$ characteristics in each zone. From this, one discovers that: (*a*) in zones I and IV, the $\mathscr{L}$ and $\mathscr{R}$ characteristics are respectively parallel, both shifted along ξ; (*b*) the $\mathscr{R}$ characteristics in zone II and the $\mathscr{L}$ characteristics in zone III are respectively parallel, shifted along τ; and (*c*) the $\mathscr{L}$ characteristics in zone II and $\mathscr{R}$ characteristics in zone III are respectively parallel, shifted along ξ.

From the foregoing it is evident that, if the flow remains subcritical, intersections do not occur. But when $\mathscr{U}$ exceeds $\mathscr{C}$ in zone III, the $\mathscr{L}$ characteristics cross there as in figure 31.

For reference, we note here that the integrated characteristics of figure 27 (*a*) give the co-ordinates of point 14 as $\tau_{14} = \frac{1}{2}$ (independently of P_e^*!) and $\xi_{14} = \frac{1}{2}(1 + \frac{1}{4}P_e^*)$. Now zone I lies entirely within the ramp region only if $\xi_{14} \leqslant 1$, i.e. only if $P_e^* < 4$. We note further that zone III is bounded by $\tau_4 = [(1+2P_e^*)^{\frac{1}{2}} - 1]/P_e^*$.

From the integrated characteristics it may be shown that $\mathscr{U} = \mathscr{C}$ in zone III at the time $\tau = 1/P_e^*$ and at the location $\xi = 1 - (1/2P_e^*)$. Since $\tau_{14} = \frac{1}{2}$, it follows that the configuration of figure 31 (*a*) occurs when $P_e^* > 2$.

Above and to the right of point 70 in figure 31 (*a*), three $\mathscr{L}$ characteristics pass through each point; hence $\mathscr{U}$ and α are triple-valued. When $P_e^* > 2$, therefore, the

mathematical solution for, say, $\alpha(\xi, \tau)$ develops as shown schematically in figure 31(*b*). Such a solution is physically inadmissible and must be modified in the region $\tau > \tau_{70}$ and $\xi > \xi_{70}$. By analogy with similar situations in gasdynamics, some type of shock-like transition presumably occurs.

14. Numerical integrations of the characteristic equations

When the term $\mathscr{H}$ is present, solutions must generally be obtained by simultaneous numerical integrations of (54) and (55). Several points relevant to the numerical integrations now bear further discussion: dissipative losses, tributaries, numerical techniques, and boundary and initial conditions. Inasmuch as numerical calculations are specific, the discussion is in the context of the experiments of part 3, namely the collapse of a long tube by the application of external pressure (see figure 32).

14.1. *Skin-friction*

The appropriate form of the friction term C_f in (7) and (55) depends on several circumstances, such as: (*a*) on whether the flow is laminar or turbulent; (*b*) on whether the time scale is such that the boundary layer is confined to a narrow region close to the wall or fills the passage in fully-developed flow; and (*c*) on the shape of the tube cross-section, in particular on whether it consists of two parallel tubes ($\alpha \gtrsim 0{\cdot}27$) or one approximately round tube ($\alpha \lesssim 0{\cdot}27$).

One cannot hope for great accuracy in the calculation of C_f. Fortunately, in the experiments to be considered, this is not necessary, since wall shear stresses *per se* are not dominant physically, except in the latter states of collapse where an accurate estimate becomes possible. Accordingly, reasonable approximations are adopted for C_f in making numerical calculations, as summarized in table 7.

14.2. *Modelling a system of symmetrically branching vessels*

Several physiological applications involve a branching system of collapsible vessels.

As a first approximation to such, we adopt a model which, with only minor modifications, may still be treated by the equations for a single tube. We assume (*a*) that the branching system is symmetric, and (*b*) that the effects of secondary flows and other loss-producing mechanisms at the junctions may be accounted for by appropriate modifications of the friction term.

At a point located at the distance x upstream of the location where the several generations of the branching symmetric system merge into a single trunk, the system consists of n identical, parallel tributary vessels. Consider the equations of mass and momentum conservation for a control volume which includes a segment of length dx of each of the tributaries.

The continuity equation is the same as for a single tube, but now $A_0(x)$ represents the *total* unstressed cross-sectional area of all n tributaries at the location x. Similarly, $q_L(x)$ is the total fluid influx per unit length entering the system as a whole.

The momentum equation of a single tube is also essentially unchanged with one important exception. The frictional term must now be modified so as to account for the difference in flow resistance between a single vessel and a system of n vessels having the same total cross-sectional area. In equation (7) and table 7, therefore,

Flow conditions	C_f
Laminar flow[a]	
Developing boundary layer[b]	
$\alpha > 0{\cdot}27$[c]	$\frac{4}{\sqrt{\pi}}\left(\frac{\mu}{\rho c_0 L}\right)^{\frac{1}{2}}(\mathscr{U}T^{\frac{1}{2}})^{-1}$
$\alpha < 0{\cdot}27$[c]	$\frac{4}{\sqrt{\pi}}\left(\frac{\mu}{\rho c_0 L}\right)^{\frac{1}{2}}(\mathscr{U}T^{\frac{1}{2}})^{-1}$
Fully developed	
$\alpha > 1{\cdot}0$[d]	$8\sqrt{(\pi)}\frac{\mu}{\rho c_0 A_0^{\frac{1}{2}}}(\mathscr{U}\alpha^{\frac{1}{2}})^{-1}$
$1{\cdot}0 > \alpha > 0{\cdot}36$[e]	$8\sqrt{(\pi)}\frac{\mu}{\rho c_0 A_0^{\frac{1}{2}}}(\mathscr{U}\alpha)^{-1}$
$\alpha < 0{\cdot}36$[f]	$\frac{70}{\sqrt{(2\pi)}}\frac{\mu}{\rho c_0 A_0^{\frac{1}{2}}}(\mathscr{U}\alpha^{\frac{1}{2}})^{-1}$
Turbulent flow[g]	
$\alpha > 0{\cdot}27$[c]	$0{\cdot}079\left(\frac{\sqrt{\pi}}{2}\right)^{0{\cdot}25}\left(\frac{\mu}{\rho c_0 A_0^{\frac{1}{2}}}\right)^{0{\cdot}25}\frac{\mathscr{U}}{\lvert\mathscr{U}\rvert}(\alpha\mathscr{U})^{-0{\cdot}25}$
$\alpha < 0{\cdot}27$[c]	$0{\cdot}079\left(\frac{\sqrt{(2\pi)}}{2}\right)^{0{\cdot}25}\left(\frac{\mu}{\rho c_0 A_0^{\frac{1}{2}}}\right)^{0{\cdot}25}\frac{\mathscr{U}}{\lvert\mathscr{U}\rvert}(\mathscr{U}\alpha^{\frac{1}{2}})^{-0{\cdot}25}$

(*a*) The flow is assumed laminar for $Re < 4000$, where Re is the Reynolds number based on hydraulic diameter.

(*b*) Computed with the assumption of a linear velocity–time profile.

(*c*) $\alpha = 0{\cdot}27$ corresponds to first contact between opposing vessel walls. For $\alpha < 0{\cdot}27$ the vessel is treated as two separate channels, each circular.

(*d*) Poiseuille flow in a tube of circular cross-section.

(*e*) Poiseuille flow in an elliptical tube (Milne-Thompson 1950).

(*f*) An approximation extracted from the results of Flaherty *et al.* (1972).

(*g*) For $Re > 4000$, and assuming a hydraulically smooth tube of circular cross-section (Schlichting 1960). Also, for turbulent flow it is assumed that the boundary layer grows so rapidly in time that the flow is always fully developed.

TABLE 7. Approximate expressions used for the friction coefficient C_f.

the area A_0 and the hydraulic diameter D_e now refer to the individual tributary. If the flow is laminar, and quasi-Poiseuille, however, one may merely use the value of A_0 for a single vessel having the combined area of all, and at the same time multiply the expression for C_f by the total number n of tributaries.

In many branching systems, this procedure precludes the necessity for retaining in (6) the term representing fluid influx, q_L. The decision as to which model to use depends primarily on the characteristics of the system itself. If the tributaries entering the trunk are not exposed to a variable external pressure, the most appropriate choice may be a function $q_L(x)$ which is independent of time. On the other hand, if the tributaries are pressurized in the same manner as the rest of the system, they are most easily accounted for by modification of the frictional term as suggested above.

14.3. *Additional loss at a rapid expansion*

We have seen in §§ 12 and 13 that certain types of external pressurization produce a constricting throat followed by a rapid expansion. Accordingly, a realistic calculation

must account for head losses associated with flow separation, and subsequent dissipative re-entrainment, in the region of rapid expansion in cross-section area (typically at the downstream border of the pressurized zone).

In order to estimate these losses, we assume (*a*) that the flow in this region is quasi-steady, and (*b*) that the flow separates as a jet at the minimum area and subsequently fills the cross-section by viscous entrainment. Then the head loss is, approximately, the so-called 'Borda–Carnot shock loss' (Prandtl–Tietjens, 1934)

$$(\tfrac{1}{2}\rho u^2+p)_2-(\tfrac{1}{2}\rho u^2+p)_1 = -\tfrac{1}{2}\rho u_1^2(1-A_1/A_2)^2. \tag{78}$$

Here the subscripts refer to the upstream (1) and downstream (2) positions of the rapid expansion. Comparison of (78) with the integrated form of the momentum conservation equation reveals that the separation losses may conveniently be incorporated into the analysis by rewriting (2) in the following manner:

$$\int_1^2 \left(\frac{\partial \mathscr{U}}{\partial \tau}+2C_f\frac{L}{D_e}\mathscr{U}^2\right)d\xi+\tfrac{1}{2}\Gamma(\mathscr{U}_2^2-\mathscr{U}_1^2)+(P_{e2}-P_{e1})+\frac{1}{\rho c_0^{*2}}[(K_p\mathscr{P})_2-(K_p\mathscr{P})_1]=0, \tag{79}$$

where

$$\Gamma \equiv \frac{\mathscr{U}_2^2-\lambda\mathscr{U}_1^2}{\mathscr{U}_2^2-\mathscr{U}_1^2}. \tag{80}$$

In this expression, $\lambda = 1$ everywhere *except* in a region of rapid expansion where it has the special value

$$\lambda \equiv \left(1-\frac{\alpha_1}{\alpha_2}\frac{A_{01}}{A_{02}}\right)^2. \tag{81}$$

Defining Γ in this way produces a consistent result on both sides of the expansion, independent of the grid size used in the numerical calculations.

The process of boundary-layer separation and reattachment actually occurs over a distance of several duct diameters. In our calculations we have treated this distance as negligible, since the lengths of tubing are much larger than the reattachment distance. This model of the separation–reattachment process is thought sufficient to connect the variables at the boundaries of the expansion zone in a reasonably correct manner even though the details of the transition structure are lost.

14.4. *Numerical procedures*

Hartree's method. The numerical integration of (54) and (55) was effected by a method due to Hartree (1952) in which the solution is found along characteristic curves which intersect a fixed, predetermined ξ–τ grid. The curves along which the solution is computed are thus not continuous, but are shifted with each successive time step. Although this procedure forfeits the elegant appearance of continuous characteristic curves, it avoids the cumbersome interpolation otherwise needed for practical interpretation of the results.

The details of marching the solution forward in time are similar to those described by Lister (1960). At a boundary, the intersecting characteristic curve is solved simultaneously with the boundary condition there.

Modified solution procedure at shock-like discontinuities. As we have seen, the characteristic curves of one family may intersect, giving rise to a region of multivalued solutions. Presumably, some mechanism not accounted for in the original set

of differential equations becomes important and dissipates enough energy to maintain a single-valued solution. By analogy with gasdynamic shock waves and open-channel hydraulic jumps, we postulate a rapid area increase through a transition region in which the head loss is given by (78). Observations of shock-like transitions in collapsible tubes (Griffiths 1971*a*; Elliott & Dawson 1977; Kececioglu 1978) suggest that the transition resembles most closely the hydraulic jump.

Methods used to accommodate shock-like discontinuities fall into two general categories which can be classified as either (*a*) 'shock-fitting', or (*b*) 'through' methods. *Shock-fitting techniques* generally model the transition as a true discontinuity and use a set of 'jump' conditions to bridge the gap between two neighbouring smooth solutions. *Through methods*, conversely, allow one to use the same finite difference formulation of the governing equations throughout the entire solution space. Methods of this type have been widely used in the analysis of unsteady open channel flows (Abbott 1975).

Procedures used. In the pressurized region, away from regions of discontinuity, we used Hartree's method.

In the region where discontinuities might occur, a procedure similar to the 'through' method was employed. The conservation equations, (6) and (79), were used in an implicit difference form. They were solved by applying the mass and modified momentum conservation conditions at alternate points in a leap-frog fashion.

14.5. *Boundary and initial conditions*

Here we refer to the specific experiments discussed in part 3 and illustrated by figure 32.

Upstream boundary condition. The flow originates at the level h_A in a high-pressure reservoir, and passes through a linear resistance, R_A, before entering the test section. Thus the boundary condition entering the collapsible tube, at $x = 0$, is

$$(uA)_{x=0} = \frac{\rho g h_A - p_0}{R_A}. \tag{82}$$

The value of R_A was determined by a preliminary calibration.

Downstream boundary condition. The compliant tube of figure 32 that comprises the test section discharges into two rigid ducts in series, each having resistance and inertance, separated by a capacitance tank. Characterizing the resistances by R_1 and R_2, the fluid inertances by $\mathscr{L}_1$ and $\mathscr{L}_2$, and the capacitance by C_v, the pressure changes between the nodal points marked on figure 32 are given by the following equations:

$$p_L - p_c = Q_1 R_1 + \mathscr{L}_1 \frac{dQ_1}{dt} + h_L \rho \left(\frac{Q_1}{A_1}\right)^2, \tag{83}$$

$$p_c - \rho g h_B = Q_2 R_2 + \mathscr{L}_2 \frac{dQ_2}{dt} \tag{84}$$

and

$$p_c - p_{c_{t=0}} = \frac{1}{C_v} \int_0^t (Q_1 - Q_2)\, dt, \tag{85}$$

where the subscripts $(\ )_1$ and $(\ )_2$ denote the first and second rigid ducts, respectively. The last term in (83), involving the loss coefficient h_L (which we assume equal to 0·55), accounts for a dissipative loss due to the abrupt changes in vessel diameter at all

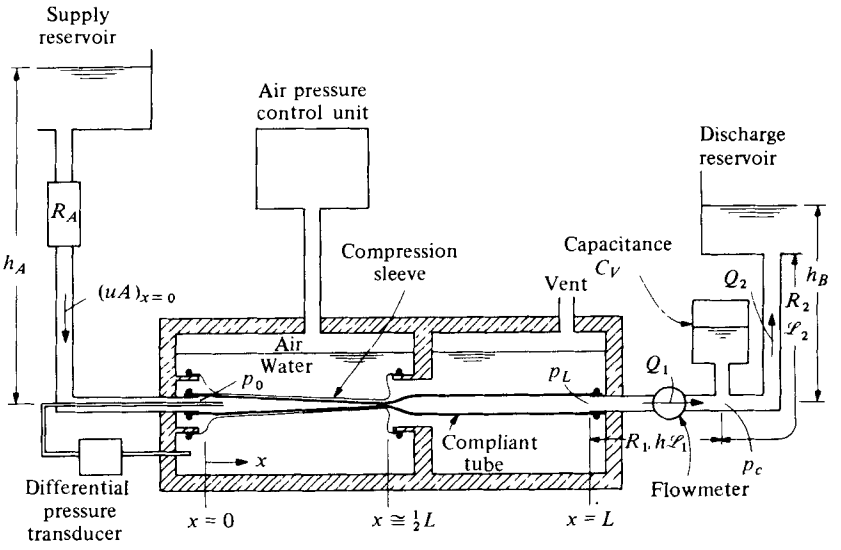

FIGURE 32. Schematic of the flow circuit and test section.

downstream locations and is computed using standard methods (ASHRAE 1969). The resistances R_1 and R_2 are related to wall shear stress and therefore depend upon the instantaneous flow conditions. We estimated them by means of the same approximations as for the collapsing vessel (table 7).

Initial condition. In the initial steady state, the collapsible tube is somewhat distended. Thus the dominant resistance of the system is concentrated upstream of the test section. The initial flow resistance in the collapsible tube may be estimated sufficiently well by Poiseuille's formula, assuming $A = A_0(x)$, where $A_0(x)$ is the unstressed cross-sectional area. Accordingly, the initial flow rate at $t = 0$ is calculated as

$$Q_{t=0} = \frac{\rho g(h_A - h_B)}{R_A + R_1 + R_2 + 8\pi\mu \int_{x=0}^{x=L} \frac{u}{A_0^2} dx}. \tag{86}$$

In the experiments, as in this expression, q_L is zero; however, a non-zero q_L can be introduced with only minor modifications.

Part 3. A simple experiment and its interpretation

15. Description of the experiment

15.1. *Apparatus and procedure*

The experiment illustrated in figure 32, although simple, exhibits many of the interesting and peculiar phenomena of unsteady flow in collapsible tubes. In addition, it contains most of the elements essential to a simulation of external compression of the veins or arteries.

Flow circuit. A single collapsible tube is attached to rigid ducting systems upstream and downstream, each of which may be simulated by a lumped-parameter model. Liquid from a constant-head supply reservoir drains through a linear resistance R_A

into the upstream end of the collapsible tube. The liquid leaving the tube enters the first of two rigid ducts which are separated by an air capacitance chamber. Leaving the second rigid duct, the liquid passes into a constant-head discharge reservoir.

Test section. The test section (figure 32) contains a single thin-walled latex rubber tube, 56 cm long, extending the entire length of a transparent cylindrical chamber which is divided into two parts approximately equal in length. External air pressure is transmitted to the upstream half of the collapsible tube through a thin, highly flexible plastic compression sleeve. The downstream part of the chamber is vented to the atmosphere. Thus the gauge pressure applied externally to the collapsible tube is essentially uniform throughout the upstream chamber, and falls to zero in a narrow transition zone, at the downstream edge of the compression sleeve.

This construction, with the external pressure applied through the sleeve, was devised to avoid the artifacts introduced near the downstream attachment zone when a collapsible tube mounted on rigid tubes is pressurized along its entire length (Shapiro 1977*b*). Furthermore, the construction simulates the pressure ramp exerted on a deep vein or artery of a pressurizing boot or cuff which surrounds a leg.

Properties of the collapsible latex tube. These have been described in § 2.3 and are summarized in figure 1.

Instrumentation. Unlike flows in rigid systems, flow measurements in collapsible tubes present formidable difficulties with regard to local observations of static pressure, cross-sectional shape and area, mean velocity, flow rate, and velocity profile. Only a few measurements can be made easily, as described below.

The elevations h_A and h_B in the constant-head reservoirs were measured on manometer scales.

A 0·033 inch internal diameter open-ended steel catheter was inserted into the tube, from the upstream end, to various longitudinal positions. This led to one side of a differential transducer, the other side of which was connected to the fluid surrounding the latex tube. Thus the transducer exhibited the transmural pressure, $(p-p_e)$.

Installed in the first length of rigid tube just downstream of the test section were a wall static pressure tap and an electromagnetic flowmeter.

Test procedure. Prior to the application of external pressure, a steady flow was established, and steady-state measurements of pressure, transmural pressure, and flow were made.

In a test run, the upstream chamber was pressurized above atmospheric in roughly an exponential fashion, characterized by the maximum gauge pressure achieved, $p_{e,\max}$, and by the rise time, $t_{1/e}$, required for the gauge pressure to reach $(1-e^{-1})$ of this maximum.

During the pressurization, all the measurements mentioned earlier were recorded.

15.2. *Parameters of the experiments*

In addition to serving the broad objectives of (*a*) exhibiting the general features of flow in a collapsing tube, and (*b*) providing a means for testing the theoretical studies, the experimental apparatus was designed to simulate compression of the veins of the lower leg. This physiologic application largely determined the ranges of parameter variations, although it is believed that the results are general in nature except perhaps for very viscous flows.

Exact modelling of the veins is not really practicable owing to the complex and variable

Parameter	Test no. 1	Notes	Test no.	Parameter varied
$p_{e_{max}}$ (cm H_2O)	27		2	$p_{e_{max}} = 10$
$t_{1/e}$ (s)	0·25		3	$p_{e_{max}} = 17{\cdot}5$
Q_i (ml s^{-1})	0		4	$p_{e_{max}} = 62$
$p_B - p_{e_1}$ (cm H_2O)	3·1	(*a*)	5	$t_{1/e} = 0{\cdot}07$
$p_B - p_{e_2}$ (cm H_2O)	3·2	(*b*)	6	$t_{1/e} = 0{\cdot}15$
C_v (cm^5/dyne)	0·011		8	$t_{1/e} = 0{\cdot}78$
L_1 (cm)	22	(*c*)	9	$C_v = 0{\cdot}002$
A_1 (cm^2)	0·317	(*c*)	10	$C_v = 0{\cdot}082$
L_2 (cm)	22	(*c*)	11	$L_1 = 41{\cdot}2$
A_2 (cm^2)	1·26	(*c*)	12	$L_1 = 9{\cdot}0$
ρ (gm cm^{-3})	1·00		13	$L_2 = \begin{cases} 17{\cdot}2 \\ 13{\cdot}0 \end{cases}$; $A_2 = \begin{cases} 0{\cdot}317 \\ 1{\cdot}26 \end{cases}$
μ (gm cm^{-1} s^{-1})	0·01		14	$p_B - p_{e_1} = 8{\cdot}8$
				$p_B - p_{e_2} = 8{\cdot}8$
(*a*) Initial transmural pressure in downstream chamber.			15	$p_B - p_{e_1} = 0{\cdot}45$
				$p_B - p_{e_2} = 0{\cdot}50$
(*b*) Initial transmural pressure in upstream chamber.			16	$Q_i = 1{\cdot}2$
(*c*) Lengths, L, and areas, A, of the rigid tubes upstream (1) and downstream (2) of the air capacitance.			17	$Q_i = 2{\cdot}8$
			18	$Q_i = 11{\cdot}5$
			19	$\rho = 1{\cdot}4$
				$\mu = 0{\cdot}055$

TABLE 8. Summary of flow experiments.

nature of the venous network. Thus, the choice of system parameters was to a certain degree arbitrary, but in each case these fell into the anticipated physiologic range.

The complete experimental sequence is summarized in table 8. In the first two columns are the parameters for test no. 1, which was taken as a reference for comparison. In each other test, all the parameters except for the one or two shown in the last column were the same as for test no. 1.

16. General character of the collapse process

The results for test no. 1, displayed in figure 33, indicate the general character of the flow and pressure traces observed in all the experiments. Several features are noteworthy.

16.1. *The wave of collapse*

The time course of external pressure application of test no. 1 is shown in figure 33(*a*). The corresponding transmural pressures at five locations inside the collapsing tube and at the point of the flow measurement in the rigid tube just downstream of the test chamber are shown in figure 33(*c*). Each of the five curves measured in the collapsing tube exhibits a sharp departure from nearly zero transmural pressure at a time that is successively later for locations further and further upstream. Having in mind that the transmural pressure also determines the area, the tube collapse is seen to be far from uniform. The data, supported by visual observations, show that initially the tube collapses only at the downstream end, and that a wave of collapse, as it were, proceeds from the downstream end to the upstream end. Concurrently with collapse, the tube effectively becomes much stiffer by reason of the strong nonlinearity of the

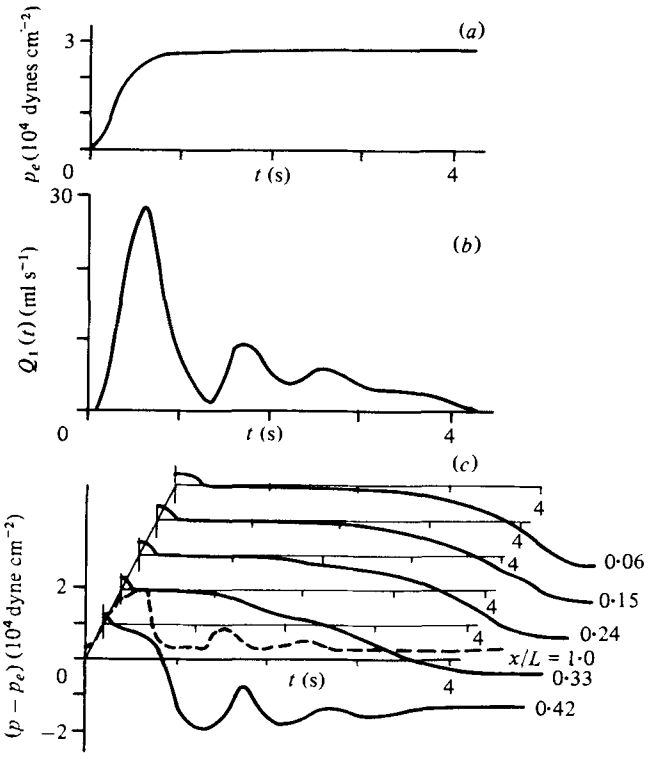

FIGURE 33. Results for test 1. (*a*) External applied pressure *vs.* time. (*b*) Volume flow rate at exit of test section, *vs.* time. (*c*) Transmural pressure difference, $p - p_e$, as a function of time, at the locations $x/L = 0{\cdot}06$, $0{\cdot}15$, $0{\cdot}24$, $0{\cdot}33$, $0{\cdot}42$ within the collapsing tube; and at $x/L = 1{\cdot}0$ at the end of the unpressurized segment (dashed line).

tube law (figure 1). Consequently, small volume excursions give rise to increasingly large changes in transmural pressure as the vessel collapses to smaller and smaller areas.

16.2. *Flow rate at exit*

As seen in figure 33(*b*), the flow rate $Q_1(t)$ at the exit of the test section first rises in response to the application of external pressure; then reaches a peak, often *before* the external pressure attains its maximum; then subsides to a generally lower level; and finally decreases toward the original steady-state flow as a new equilibrium state is established. In cases of non-zero initial flow, the final steady-state flow rate is slightly below the original one due to the additional flow resistance in the collapsed part of the tube.

Because the fluid at $\xi = 1$ is unaffected until compression waves arrive from the pressurized zone, the flow rate does not begin to rise immediately after the pressure is applied. In this regard, we note that $Q_1(t)$ is not the same as the flow rate at the exit of the pressurized zone ($\xi \simeq 0{\cdot}5$), nor is it identical with the flow rate in the collapsible tube at its downstream end but before the attachment to the rigid tube. However, since the collapsible tube is relatively stiff at positive transmural pressure, the displayed curve of $Q_1(t)$ is a fairly good indicator of the flow rate discharged from the pressurized segment of the collapsible tube.

16.3. *Evidence of critical speed and choking*

After the strong initial transient, damped ringing oscillations are superimposed upon a flow rate that remains roughly constant for a substantial time. These are due to the lumped inertance–capacitance discharge system which is excited by the incoming flow. Significantly, the oscillations are not transmitted upstream into the collapsing portion of the tube: except at $\xi = 0{\cdot}42$ they are absent in the pressure recordings. The position $\xi = 0{\cdot}42$ is located in the pressure ramp, presumably downstream of the point where the flow speed has become critical. Disturbances do not propagate upstream of this point. The oscillations are heavily damped owing to various head losses. They subside at approximately the same time that the tube approaches a new static equilibrium with the elevated external pressure, but this is coincidental.

Attainment of the critical speed and choking are also suggested by the fact that, apart from the artifact of ringing, the mean flow rate is nearly constant for a substantial period after the initial transient. The slow decay in mean flow rate is attributable to the increasing frictional losses upstream of the choke point.

16.4. *The three phases of the collapse process*

One may usefully think of the complete process of tube collapse as occurring in three phases, in each of which different physical phenomena are dominant.

Phase I: the initial transient. This is identified in the volume flow rate trace as the period of flow acceleration up to approximately the initial peak in $Q_1(t)$.

Owing to the high linear flow resistance upstream of the test section, and also because the supply reservoir pressure always exceeded the applied external pressure, emptying occurs in the downstream direction. The experimental observation, mentioned earlier, that the tube begins to collapse only near the downstream boundary of the compression sleeve, is precisely what was found theoretically in parts 1 and 2, and may be explained physically as follows.

When the external pressure is applied, the internal pressure at first increases by exactly the same amount because, until some collapse occurs, the transmural pressure must remain unaltered. A gradient of internal pressure therefore exists initially only at the location of external pressure gradient, that is, near the downstream edge of the compression sleeve. Since the fluid is accelerated only by means of such a pressure gradient, the volume flow rate first begins to increase at this location. Continuity requires that $\partial Q/\partial x + \partial A/\partial t = 0$; thus the space gradient of Q that is established requires a simultaneous time gradient of A. Accordingly, the vessel begins to collapse in the zone of acceleration. Rarefaction waves propagating upstream into the pressurized zone accelerate the fluid there in the downstream direction, also causing the area there to decrease, while the vessel continues to collapse at the downstream end. As the throat formed near the downstream end of the pressurized zone becomes progressively smaller, the exit flow rate is reduced by the simultaneous effects of the Bernoulli pressure drop, the pressure decrease due to the local acceleration $\partial u/\partial t$, and the frictional pressure loss, all of which are magnified by the reduced area. These effects in combination produce an abrupt peak in volume flow rate, even though the external pressure may still be rising.

Phase II: quasi-steady emptying. Two related events, the flow rate falling from its peak to a much lower level and the establishment of a quasi-steady throat in the

region of minimum cross-sectional area, mark the beginning of the quasi-steady phase. This is characterized by flow limitation or choking near the upstream end of the pressure ramp where the flow velocity now equals the wave speed. As time progresses, the choking flow rate slowly decreases owing to increasing head losses, and the wave of collapse propagates upstream more and more slowly. The accompanying ringing oscillations are an artifact of the discharge system.

Phase III: viscous drainage. Finally, as the length of the collapsed region increases, and the Reynolds number becomes progressively smaller, viscous effects come to dominate. This marks the beginning of a viscous drain-off phase which is analogous to a distributed nonlinear, variable capacitance discharging through a distributed linear but variable resistance. The liquid remaining in the tube is slowly squeezed out as the vessel asymptotically approaches its new equilibrium configuration.

In this case, phase III occupies a relatively brief period, but if the tube were much longer, or if the fluid viscosity were increased over that of test 1, it would account for a much larger fraction of the total emptying period.

17. Order-of-magnitude estimates

Before examining in § 18 the effects of various parameters on the results, and the degree to which full-blown numerical integrations of the characteristic equations are capable of predicting the experimental results, we present here simple order-of-magnitude analyses for each of the three phases of the collapse process.

17.1. *Phase I: the initial transient*

The two observable features which characterize the initial transient are the peak flow rate, Q_p, and the time, t_p, at which this occurs.

As the external pressure $p_e(t)$ is first applied, simple compression waves run downstream and simple rarefaction waves upstream, as described in § 12 for a spatial step in p_e and in § 14 for a spatial ramp in p_e. At small times, the flow curve of figure 24(*d*) may be approximated as linear. Thus,

$$Q(t) \cong K_Q A_0 c_0 [p_e(t)/\rho c_0^2], \tag{87}$$

where K_Q is a numerical constant; for a spatial step change in p_e, $K_Q \cong 0{\cdot}5$. Furthermore, for small times, $p_e(t)$ may be approximated by a linear function

$$p_e(t) \cong \dot{p}_e t, \tag{88}$$

where $\dot{p}_e \equiv dp_e/dt$ is taken as constant.

These combine to give

$$Q(t) \cong (K_Q A_0 c_0 \dot{p}_e/\rho c_0^2)\, t, \tag{89}$$

a linear relationship between Q and t that indeed approximates the initial portion of figure 33(*b*).

From the results of §§ 4 and 13, and from figures 24(*b*) and 29, it appears that, initially, fluid is transported from the collapsing upstream portion of the pressure ramp to the inflating downstream portion. In this regard, note that the cross-sectional area in zone I (figure 27) is constant, so that the central segment in the pressure ramp acts like a rigid tube. Now the inflating segment of tube is much stiffer and, concomitantly, has a much higher wave speed than the collapsing segment. Owing to both

these effects, the total fluid volume that has passed out of the pressure ramp up to the time t_p may be considered to have come principally from the volume change that occurs inside the ramp region. That the peak is usually much larger than the choked flow rate from the upstream region supports this assumption. We attribute the peak in the volume flow rate Q_p to the fact that this volume is of limited size, and that further transport of fluid is at a much lower rate because it must come from the upstream regiona relatively (which has low wave speed) through a constantly diminishing throat.

We may approximate the volume that can be disgorged from the pressure ramp as $K_R A_0 L_R$, where L_R is the length of the pressure ramp, and K_R is a numerical constant, of order of magnitude, say, $K_R \cong \frac{1}{2}$. Assuming that this volume is the time-integral of (89) from $t = 0$ to $t = t_p$, namely $\frac{1}{2} Q_p t_p$, we find that

$$Q_p \cong A_0 \left[(2K_R K_Q) \left(\frac{\dot{p}_e L_R}{\rho c_0} \right) \right]^{\frac{1}{2}}; \quad t_p \cong \left[\left(\frac{2K_R}{K_Q} \right) \left(\frac{c_0 L_R}{\dot{p}_e} \right) \right]^{\frac{1}{2}}. \tag{90}$$

These are crude estimates, to be sure, but they represent the essential physics sufficiently well to portray correctly the relationships among the flow variables during the initial transient.

17.2. *Phase II: quasi-steady emptying*

If we ignore the decaying flow oscillations in the region downstream of the collapsing zone, each test exhibits a period of relatively constant flow rate following the initial transient peak. This agrees with the theoretical findings (§§ 12 and 13) of flow limitation, or choking, at the edge of a region of uniformly applied external pressure. Since the limitation occurs at a condition of $u = c$, it is similar to the choking phenomenon familiar in gasdynamics and which occurs also for steady flow in a collapsible tube (Shapiro 1977*b*).

Previously we have associated the transient peak in $Q(t)$ with vessel collapse in the region of the pressure ramp. Once this collapse has occurred, however, the flow rates into and out of the ramp region must be nearly equal. Since the flow rate upstream is limited to the first plateau of figure 24 (*c*), the flow rate downstream must be limited as well. As viscous effects become increasingly important with the growing length of the throat region, however, the locus of possible states will fall below the curve shown in figure 24 (*c*), which was constructed for inviscid flow. This explains the slow temporal decay in volume flow rate beginning shortly after the initial peak.

For short tubes and fluids of low viscosity, only a fraction of the vessel empties before either viscous or end effects become dominant. During this period the vessel empties at a nearly constant rate Q_m whose upper bound is given roughly by the first peak in $\mathscr{U}\alpha$ on figure 24 (*c*):

$$Q_m \cong 0{\cdot}13 A_0 c_0. \tag{91}$$

If Q_m were nearly constant throughout a large fraction of the emptying period, the time t_e required to empty a tube of length L_u would be approximated by

$$t_e \cong A_0 L_u / Q_m \cong L_u / 0{\cdot}13 c_0. \tag{92}$$

This, we note, is about eight times greater than the time of wave passage.

17.3. *Phase III: viscous drainage*

As the extent of the collapsed region increases and the flow speeds decrease, viscous effects eventually become dominant. The flow rate unchokes and asymptotically goes toward zero.

We assume that the appropriate Reynolds number is sufficiently small so that the flow is essentially inertia-free. Thus it may be treated as locally-Poiseuille in character, in which case the momentum equation reduces to

$$\frac{\partial p}{\partial x} + K_f(\alpha)\mu\frac{u}{A} = 0, \tag{93}$$

where μ is the coefficient of viscosity and $K_f(\alpha)$ is a pure number that depends only on the shape of the cross-section. For a circular tube, $K_f = 8\pi$ (the familiar value for Poiseuille flow). For a collapsible tube, $K_f(\alpha)$ is only a weak function of α; in the similarity range, $K_f \cong 70$, and in fact this value is quite accurate in the range $\alpha < 0{\cdot}36$ (Flaherty *et al.* 1972).

Combination of (93) with continuity (for $q_L = 0$), equation (1), and with the wave-speed definition, equation (4), leads to a diffusion-type equation,

$$\frac{\partial \alpha}{\partial t} = \frac{\partial}{\partial x}\left[J(\alpha)\frac{\partial \alpha}{\partial x}\right], \tag{94a}$$

where

$$J(\alpha) \equiv \frac{\rho A_0 c_0^2}{\mu}\frac{\alpha \mathscr{C}^2(\alpha)}{K_f(\alpha)} \tag{94b}$$

is a highly nonlinear diffusion coefficient. During the viscous drainage phase, therefore, the last vestiges of collapse proceed upstream in a diffusion-like manner.

Similarity solutions. Introduction into (94*a*) of the well-known similarity variable of the form $x/t^{\frac{1}{2}}$ for diffusion-type problems yields the ordinary differential equation

$$\frac{d}{d\zeta}\left[\frac{\alpha \mathscr{C}^2(\alpha)}{K_f(\alpha)}\frac{d\alpha}{d\zeta}\right] + \frac{\zeta}{2}\frac{d\alpha}{d\zeta} = 0, \tag{95a}$$

where

$$\zeta \equiv \frac{x}{t^{\frac{1}{2}}}\left(\frac{\mu}{\rho A_0 c_0^2}\right)^{\frac{1}{2}}. \tag{95b}$$

Unfortunately, however, the initial and boundary conditions cannot be generally expressed in terms of ζ alone. Consequently similarity-type solutions of the viscous drain-off phase do not strictly exist for the problem at hand. Yet it is a reasonable conjecture that the general form of similarity solutions to the diffusion equation provides clues to the actual behaviour even when the boundary and initial conditions are not exactly of similarity form. To the extent that this is true, the following remarks apply.

The exit flow rate $Q(t)$ is given by the time rate of decrease of tube volume. Thus

$$Q(t) = \frac{d}{dt}\int (A_0 - A)\,dx = \frac{d}{dt}\left[\left(\frac{\rho A_0^3 c_0^2}{\mu}.t\right)^{\frac{1}{2}}\int (1-\alpha)\,d\zeta\right],$$

where the integral extends over the entire collapsing length. Now, since it is presumed that $\alpha \cong \alpha(\zeta)$, it follows that, in the viscous drain-off phase,

$$Q(t) \cong \text{constant}.\left(\frac{\rho A_0^3 c_0^2}{\mu}.\frac{1}{t}\right)^{\frac{1}{2}}, \tag{96}$$

where t is measured from the imaginary onset of inertia-free emptying, t_V. The corresponding volume of fluid discharged is given by

$$V_E \cong \int Q(t)\,dt \cong \text{constant}.\left(\frac{\rho A_0^3 c_0^2}{\mu}.t\right)^{\frac{1}{2}}. \tag{97}$$

Accordingly, the flow rate varies as the inverse square root of the viscosity, and time required for equal volume displacements varies directly with the viscosity.

18. Experimental results and comparison with numerical integrations

Numerical simulations, using the techniques described in § 14, were carried out for each of the tests listed in table 8.

For these calculations it was assumed that the pressure ramp at the downstream edge of the pressurized zone was S-shaped, consisting of two matched quadratic curves, with a total length of either 5 or 10 cm. The former was selected unless it displayed inadequate computational stability. The solutions were generally insensitive to changes in this parameter with, however, one exception: the frequency of the flow oscillations was lower for the greater ramp length.

18.1. *Experiments with different maximum applied pressure*

In tests 1, 2, 3 and 4, all the experimental parameters were held nearly constant, except for the magnitude of the applied pressure, which varied over the range 10 to 62 cm H_2O.

Figure 34 shows that the theoretically predicted time history of the volume flow rate at the exit of the test section is in generally good agreement with the experimental results. Except for test no. 2, the initial transient phase is remarkably well reproduced by the theory. The average level of flow during the quasi-steady period appears to be somewhat over-estimated. As a result, the collapse process ends earlier in the simulation than in the experiment. This discrepancy could easily be due to inaccuracies in the tube law, particularly the effects of longitudinal tension and curvature, and errors in the difficult task of estimating head losses following the throat region.

In order to ascertain the degree of success the simulation achieved in predicting general trends, several characteristic parameters of the flow curve were selected and each was plotted in figure 35 as a function of applied pressure for both experiment and theory. The parameters shown are (1) the peak flow volume flow rate, Q_p; (2) the time t_p at which the flow maximum occurs; and (3) the time t_e required for the tube to empty, approximated by the time at which the volume flow rate trace first goes negative.

Both t_p and t_e approach a more or less constant minimum as the external pressure is increased, while the peak flow rate appears to level off.

Examination of figure 34 shows that the quasi-steady flow rate in phase II is insensitive to the applied pressure, at least when the latter is above a certain threshold value (in this case, 17 cm H_2O seems sufficient). A similar effect is well established in pulmonary physiology (Mead *et al.* 1967): at a fixed lung volume the volume flow rate during forced expiration no longer increases with applied pleural pressure after the latter has reached a certain value. There is some support for the conjecture that this

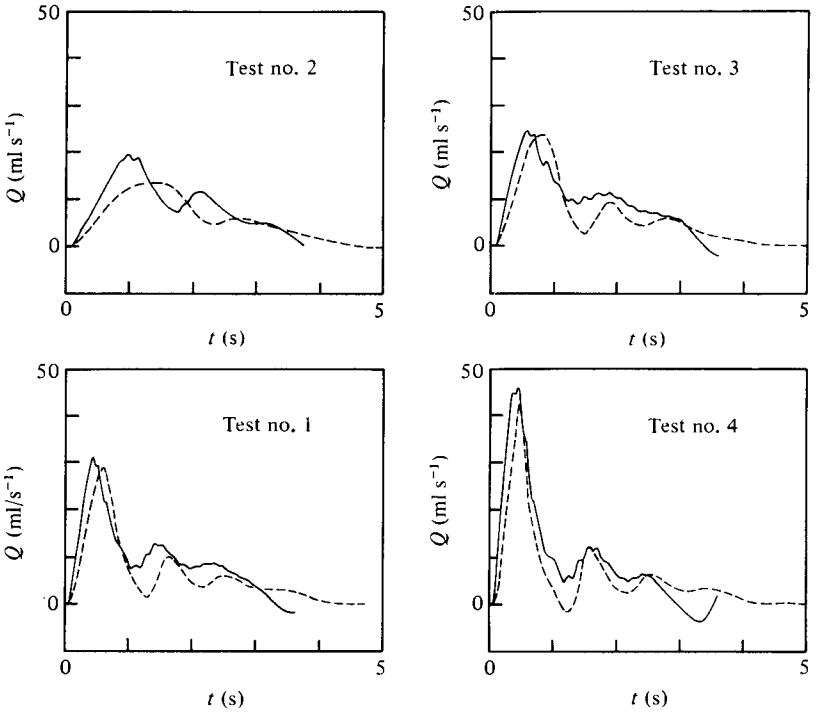

FIGURE 34. Volume flow rate *vs.* time at exit of test section, for different maximum applied pressures. Experimental: dashed lines. Theoretical: solid lines.

Test no.	2	3	1	4
$P_{e\ max}$ (cm H_2O)	10	17·5	27	62

'effort-independent' phenomenon is related to choking within the trachea at the critical speed (Elliott & Dawson 1977).

Although the theoretical and experimental curves are displaced by as much as 25 % the agreement in the general character of the curves is good.

18.2. *Variations in the rate of pressurization*

The influence of changes in compression rate was investigated in test nos. 1, 5, 6, and 8, with results as shown in figures 36 and 37. The format is the same as in the previous comparisons. These results, as in the previous set of experiments, indicate relatively mild trends toward higher peak flow rates and lower values of t_p for more rapid compression rates.

Again, t_e is nearly constant. If one wishes to minimize the time for complete emptying, therefore, neither raising the maximum pressure nor applying the pressure more quickly has a pronounced effect once certain values have been exceeded. This is in accord with the mechanism of the initial transient and with the phenomenon of choked flow.

The theoretical curves are again in rather good agreement with the experiments, considering the several uncertainties in application of the theory.

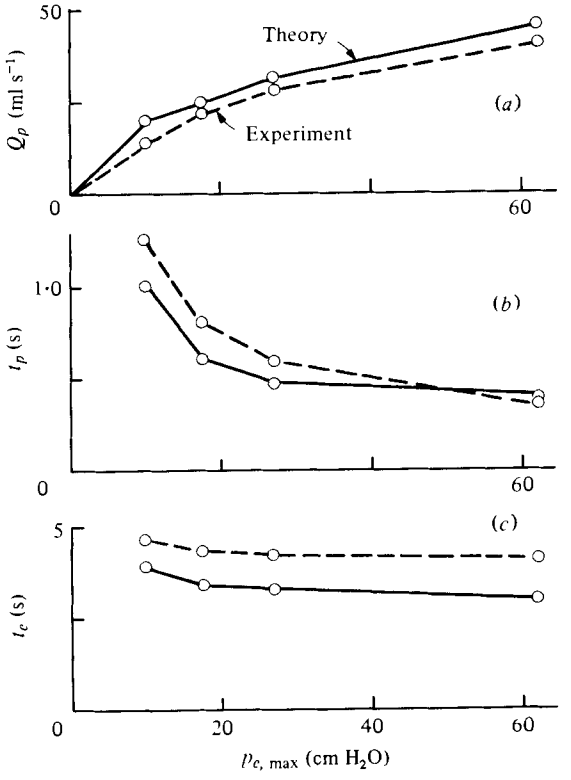

FIGURE 35. Characteristic flow parameters as functions of maximum applied pressure. Experimental: dashed lines. Theoretical: solid lines.

18.3. *The effect of downstream parameters*

The significance of the inertive–resistive and capacitive elements located downstream of the test section was evaluated in an extensive testing sequence: tests 9–15 in table 8. The results were notable in that they produced relatively little effect on the collapse process as reflected in the characteristic flow parameters Q_p and t_e.

Four tests of this series are compared in table 9, with test no. 1 as a reference. In this table, each number represents the ratio of the value of the parameter of the indicated test divided by that of test 1. For each test, the ratios are given for both the experimental measurement and the theoretical prediction.

In addition to Q_p and t_e, a third parameter is provided, namely the elapsed time between the first flow maximum and the first flow minimum, or, equivalently, the half period of the flow oscillations. This was the only flow variable which *did* change significantly with relatively large changes in the downstream flow parameters.

The mechanism producing the observed oscillations can be described in rather simple terms. The hydraulic system downstream of the throat consists essentially of three capacitors separated by two inertive–resistive elements. An impulse (the first flow peak) excites the system and causes it to ring at a frequency determined by the inertance and capacitance of each of the elements. Even lowering the discharge reservoir head, h_B, alters one of these elements, the capacitance associated with the compliance of the latex tube downstream of the throat, owing to nonlinearities in the tube law.

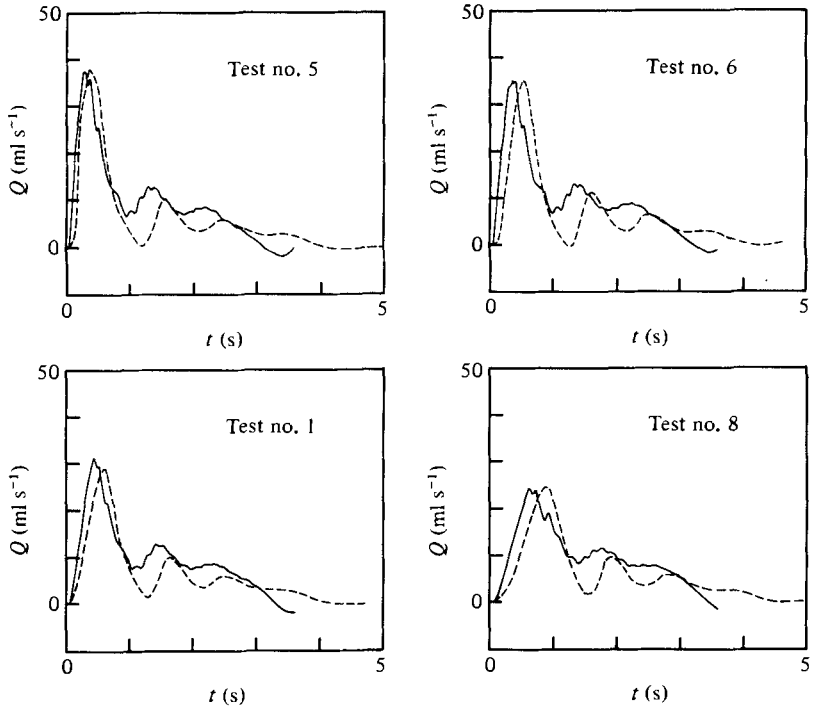

FIGURE 36. Volume flow rate *vs.* time at exit of test section, for different rise times, $t_{1/e}$. Experimental: dashed lines. Theoretical: solid lines.

Test no.	5	6	1	8
$t_{1/e}$ (s)	0·07	0·15	0·25	0·78

As noted earlier, the oscillations do not propagate upstream of the throat and have little or no effect on the flow behaviour in the collapsing portion of the tube. Changes upstream of the throat, then, can be brought about only by modifying either the pressure cycle (as described earlier), the upstream conditions, the tube properties, or the fluid properties.

18.4. *The effect of fluid viscosity*

Using a glycerine–water mixture, the fluid viscosity was raised in test no. 19 by a factor of 5·5. The experimental and theoretical flow traces for this test, figure 38, exhibit two important features. First, the initial transient, as expected, is largely inertia-dominated; even changing the viscosity by about sixfold caused very little change in the shape and magnitude of the initial flow peak. Second, a viscosity change of this magnitude significantly lengthened the viscous drainage phase, to the extent that it can no longer be neglected in estimating the total emptying time of the vessel. In both the theory and the experiment, it took more than twice as long to empty the vessel as compared with all previously discussed tests.

18.5. *Non-zero initial flow rate*

The baseline flow rates prior to pressurization were varied in tests 16–18 by changes in upstream flow resistance while the supply pressure and all other parameters were held constant. The maximum baseline flow rate was roughly equal to the

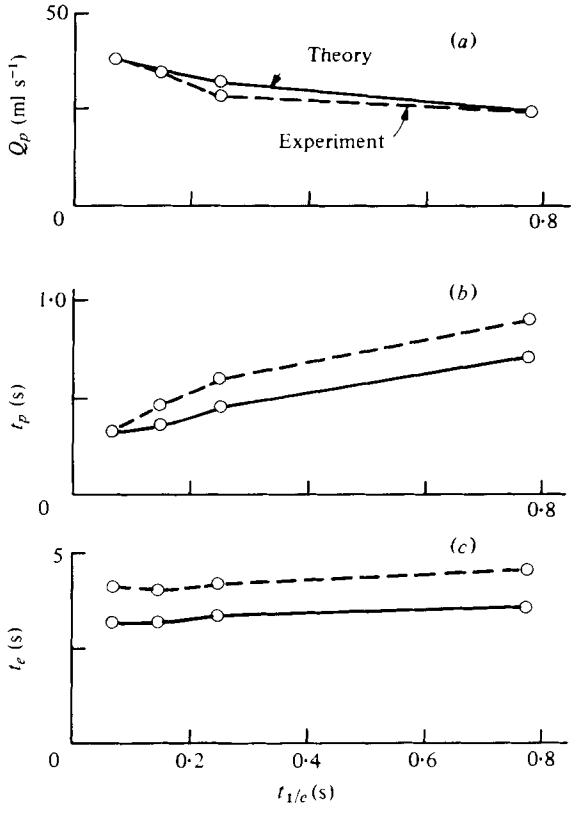

FIGURE 37. Characteristic flow parameters as functions of rise time. Experimental: dashed lines. Theoretical: solid lines.

	Test number							
	9		11		13		15	
Variable	Exp.	Theory	Exp.	Theory	Exp.	Theory	Exp.	Theory
Q_p	1·0	0·98	0·89	0·86	1·05	1·00	0·97	0·89
t_e	1·01	0·98	1·11	1·06	1·08	1·00	1·08	1·06
Half period of oscillation	0·77	0·71	1·16	1·36	0·99	0·93	1·51	(*a*)

(*a*) Oscillations were too weak to permit accurate measurement of the oscillation period.

TABLE 9. The effects of changes in downstream parameters. (Each number is the ratio of the value of the parameter of the indicated test divided by that of test 1.)

predicted limiting flow rate using the approximate analysis of (91), which was, in turn, approximately one-third of the typical values of peak flow rate.

Supporting the hypothesis that most of the fluid volume expelled during the initial transient phase originates in the pressure-ramp region, Q_p remained nearly constant in these tests.

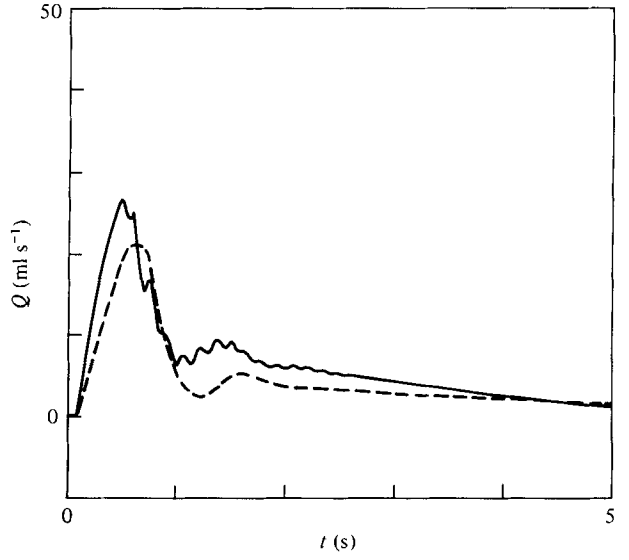

FIGURE 38. Results for test 19, with a viscosity 5·5 times that of test 1. Experimental: dashed line. Theoretical: solid line.

In the final equilibrium state the vessel is not uniformly collapsed. Owing to frictional pressure losses, the area is greater at the upstream end than at the downstream end. In general, the increased frictional resistance at the throat, accompanying higher flow rates, leads to a more inflated final state.

In separate tests we have found that the degree of collapse is insensitive to the level of applied pressure. As the pressure is increased, a balance is struck between the higher driving pressure in the upstream fluid and the greater frictional losses at the throat. This balance results in a vessel profile which is relatively independent of the applied pressure.

18.6. *Comparisons with the order-of-magnitude estimates*

We have observed that, in nearly all the tests, the time to empty the vessel remains relatively constant. This is in good qualitative agreement with the prediction of (92) based on constant values of c_0 and L_u. The quantitative estimate obtained using (92) is about two-thirds of the experimental value, which, considering the nature of the approximation, is quite good.

This order-of-magnitude estimate was based on the assumption that the viscous drain-off period (phase III) accounts for only a small fraction of the total process. In the range of these tests (with the exception of test no. 19), that assumption seems to be satisfied. The postulated dependence of t_e on L_u/c_0 has been further supported by additional experimental and theoretical results, not reported here, in which vessels with different wall thicknesses were found to empty either much more slowly or more rapidly depending on whether the wall was more or less flexible.

In other exploratory tests not reported here tests over a wide range of viscosities gave approximate verification to the similarity conjectures of (96) and (97).

The claims of the order-of-magnitude analysis concerning the time and magnitude of the peak flow rate cannot easily be verified for the following reasons. First, the

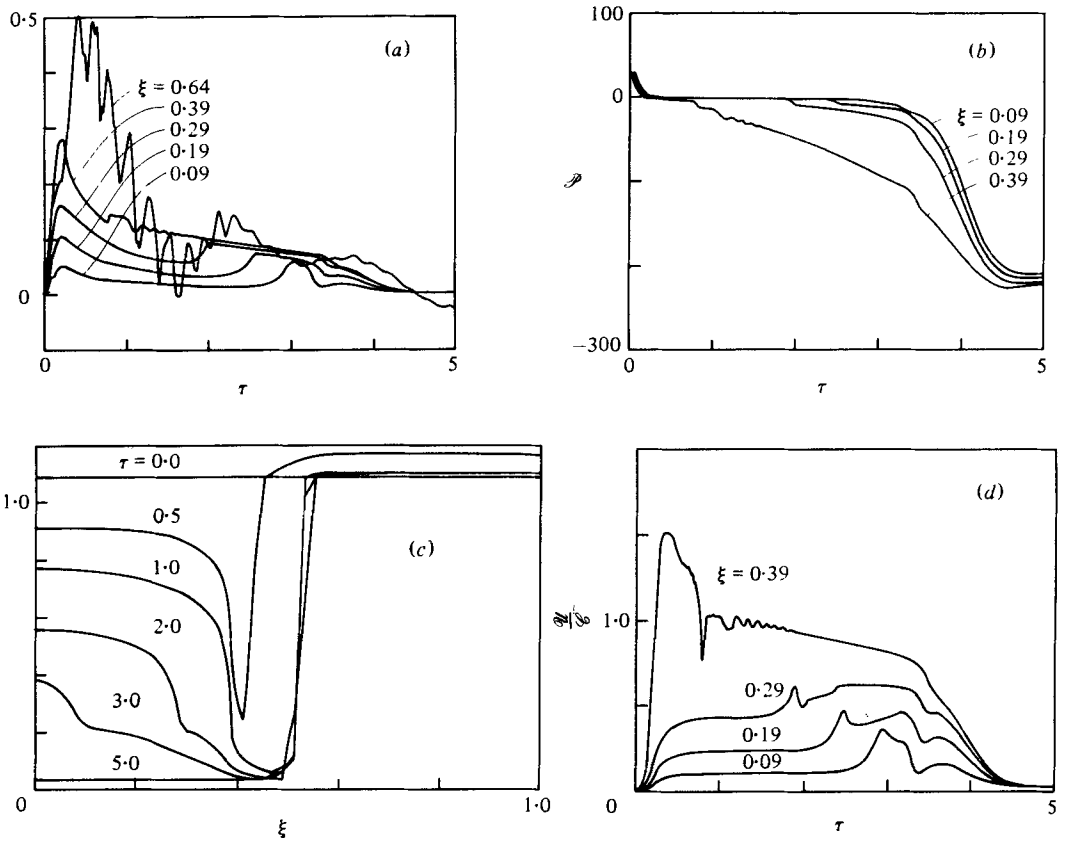

FIGURE 39. Detailed results of numerical calculations for the parameters of test 1, with $A_0 = 1{\cdot}06$ cm^2 and $c_0 = 60$ cm s^{-1}. (*a*) Flow rate *vs.* time at 5 locations. (*b*) Transmural pressure *vs.* time at 4 locations. (*c*) Area *vs.* distance at 6 times. (*d*) Speed index $\mathscr{U}/\mathscr{C}$ *vs.* time at 4 locations.

experimental measurements were made at the exit of the test section located a considerable distance downstream of the throat. Flow conditions there are strongly influenced by the nature of the boundary condition. Second, we assumed previously that the effect of reflexions can be neglected. In contrast, the numerical results clearly indicate that reflexions do reach the edge of the pressurized region well before the peak occurs, causing flow disturbances not accounted for in the order-of-magnitude analysis.

19. Theoretical details of the collapse process

Having demonstrated the general validity of the theory as presented, we may now, with some confidence, use numerical simulations to gain information concerning details of the collapse process that would be most difficult to obtain experimentally.

Figure 39 exhibits the detailed numerical solution for the case of a uniform tube ($A_0 = 1{\cdot}06$ cm^2; $c_0 = 60$ cm/s), with the parameters of pressure application and fluid and boundary parameters all as in test no. 1.

19.1. *Volume flow rate*

Figure 39(*a*) shows the normalized volume flow rate (Q/A_0c_0) as a function of normalized time (c_0t/L) at five locations: one just downstream of the pressure ramp, one inside the upstream end of the ramp, and three at successive locations further upstream in the region of uniform compression. Violent flow oscillations are evident only in the trace downstream of the ramp. Their absence in the other four traces signals the presence of a supercritical region which effectively isolates upstream points from disturbances created downstream. The two frequencies superimposed in the downstream flow trace represent (*a*) wave reflexions back and forth in the unpressurized region of the collapsible tube, and (*b*) ringing associated with the coupling between the compliant tube and downstream flow elements as mentioned earlier. In the experiments of § 18, the former are largely damped downstream of the collapsible tube, apparently much more so than in the theory, and therefore are barely detectable in the flow traces.

The curve representing volume flow rate at $\xi = 0{\cdot}39$ serves to illustrate some of the predictions of the order-of-magnitude analyses. The initial peak is higher than the estimate of (91) partly because the tube is initially in a more inflated state than was assumed previously. Modifying figure 24(*c*) to account for this initial condition, we find that the peak corresponds well with the estimate of simple-wave theory. This curve demonstrates also the slowly decaying flow rate characteristic of phase II.

At larger times we find the end of phase II strongly delineated from the final phase of viscous drainage by an abrupt decrease in flow rate. Afterward the flow rate falls asymptotically to zero as the tube empties.

19.2. *Transmural pressure*

Figure 39(*b*) shows that, upon the application of external pressure, the transmural pressure drops rapidly to nearly zero, the change propagating at the wave speed in the initially distended tube.

Further changes, however, occur much more slowly. At each location, the time corresponding to vessel collapse can be identified as the sudden departure from zero transmural pressure. This event, too, propagates in a wave-like fashion but at a much slower speed. It has the appearance of a diffusion-like wave and moves progressively more slowly as the vessel collapses.

19.3. *Cross-sectional area*

The successive area profiles are shown in figure 39(*c*) in the form of normalized cross-sectional area *versus* distance at six different times. These curves dramatically exhibit the necking down that occurs very early in the collapse process and which limits the rate of further emptying of the vessel. The necked-down region or throat develops first at the upstream end of the ramp; at the same location where, at $\tau = 0{\cdot}5$, a shock-like transition appears. Subsequently, the throat moves downstream until a relatively constant profile is achieved within the ramp zone.

The curves also show clearly how the collapse proceeds upstream in a wave-like manner.

19.4. *Speed index*

Finally, since many of the predicted flow phenomena depend upon whether or not the flow becomes supercritical, figure 39(*d*) shows $\mathscr{U}/\mathscr{C}$ as a function of time at four different upstream locations. Only at $\xi = 0{\cdot}39$, a point just inside the upstream end of the ramp, does $\mathscr{U}/\mathscr{C}$ temporarily exceed unity. Following a short supercritical interval, which corresponds in time to the initial transient, the flow speed returns to the critical value and then slowly decays in accordance with the flow-rate trace.

There is some evidence of a shock-like transition in the uppermost curve ($\xi = 0{\cdot}39$) at $\tau \cong 0{\cdot}7$.

19.5. *Further results*

These calculated results, together with the experimental data, clearly show the importance to the collapse process of the formation of a flow-limiting throat.

As suggested by several of the examples in part 1, this phenomenon can to a large degree be eliminated by different and somewhat more complex modes of pressurization: in particular, (*a*) through application of the external pressure in a 'milking' wave; or (*b*) by applying it as a non-uniform gradient, higher at the upstream end. These indications of the linearized theory are confirmed by numerical calculations based on the nonlinear theory of § 14.

This research was supported by the Fluid Mechanics Program of the National Science Foundation (Grant no. ENG-76-08924), by the National Heart, Lung and Blood Institute (Grant no. 1-R01-HL17974), and by a pre-doctoral Fellowship in Biomedical Engineering (to RDK) under Grant no. 5 T01 GM-02136 of the National Institute of General Medical Sciences. Dr Peter W. Scherer contributed to the early phases of the research.

REFERENCES

Abbott, M. B. 1966 *An Introduction to the Method of Characteristics*. New York: American Elsevier.

Abbott, M. B. 1975 Weak solutions of the equations of open channel flow. In *Unsteady Flow in Open Channels* (ed. K. Mahmood & V. Yevjevich), vol. 1, pp. 283–312. Water Resources Publications.

Arnitzenius, A. C., Koops, J., Rodrigo, F. A., Elsbach, H. & Brummelen, A. G. E. 1970 Circulatory effects of body acceleration given synchronously with the heart beat (BASH): Ballistocardiography and cardiovascular therapy. *Bibl. Cardiol.* vol. 26, no. 180.

ASHRAE 1969 *ASHRAE Guide and Data Book – Equipment Volume*. New York: American Society of Heating, Refrigeration and Air Conditioning Engineers.

Attinger, E. O. 1964 *Pulsatile Blood Flow*. McGraw-Hill.

Beam, R. M. 1968 Finite amplitude waves in fluid filled elastic tubes: wave distortion, shock waves, and Korotkoff sounds. *N.A.S.A. Tech. Note* D-4803.

Brawley, R. K., Oldham, H. N., Vasko, J. S., Henney, R. P. & Morrow, A. G. 1966 Influence of right atrial pressure pulse on instantaneous vena caval blood flow. *Am. J. Physiol.* **211**, 347–353.

Collins, R. E. C. 1976 Physical methods of prophylaxis against deep vein thrombosis. In *Prophylactic Therapy of Deep Vein Thrombosis and Pulmonary Embolism* (ed. J. Fratantoni & S. Wessler), pp. 158–172. DHEW Publication no. (NIH) 76–866.

Dawson, S. V. & Elliott, E. A. 1977 Wave-speed limitation on expiratory flow – a unifying concept. *J. Appl. Physiol.* **43**, 498–515.

ELLIOTT, E. A. & DAWSON, S. V. 1977 Test of wave-speed theory of flow limitation in elastic tubes. *J. Appl. Physiol.* **43**, 516–522.

FLAHERTY, J. E., KELLER, J. B. & RUBINOW, S. I. 1972 Post buckling behavior of elastic tubes and rings with opposite sides in contact. *SIAM J. of Appl. Math.* **23**, 446–455.

GRIFFITHS, D. J. 1969 Urethral elasticity and micturition hydrodynamics in females. *Med. & Biol. Engng* **7**, 201–215.

GRIFFITHS, D. J. 1971*a* Hydrodynamics of male micturition – I: Theory of steady flow through elastic-walled tubes. *Med. & Biol. Engng* **9**, 581–588.

GRIFFITHS, D. J. 1971*b* Steady fluid flow through veins and collapsible tubes. *Med. & Biol. Engng* **9**, 597–602.

GRIFFITHS, D. J. 1973 The mechanics of the urethra and of micturition. *Brit. J. of Urology* **45**, 497–507.

GUYTON, A. C., LANGSTON, J. B. & CARRIER, O. 1962 Decrease of venous return caused by right atrial pulsation. *Circulation Res.* **10**, 188–196.

HARTREE, D. R. 1952 Some practical methods of using characteristics in the calculation of non-steady compressible flows. *Los Alamos Rep.* LA-HU-1.

KANTROWITZ, A. 1968 Theoretical and experimental analysis of the intra-aortic balloon pump. *Trans. Am. Soc. Artif. Int. Organs* **14**, 338–343.

KECECIOGLU, I. 1978 Structure of shock waves in collapsible-tube flow. *Proc. 31st Ann. Conf. Engng in Medicine & Biol., Atlanta, Ga.*

KIVITY, Y. & COLLINS, R. 1974 Nonlinear wave propagation in visco-elastic tubes: application to aortic rupture. *J. Biomech.* **7**, 67–76.

LISTER, M. 1960 The numerical solution of hyperbolic partial differential equations by the method of characteristics. In *Mathematical Methods for Digital Computers* (ed. A. Ralston & H. S. Wilf), pp. 165–179. Wiley.

MACKLEM, P. T. & MEAD, J. 1967 The physiological basis of common pulmonary function tests. *Archives of Environ. Health* **14**, 5–9.

MCCLURKEN, M. E. 1978 Shape-independent area measurement in collapsible tubes by an electrical impedance technique. *Proc. 31st Ann. Conf. Engng in Medicine & Biol., Atlanta, Ga.*

MCMAHON, T. A., CLARK, C., MURTHY, V. S. & SHAPIRO, A. H. 1971 Intra-aortic balloon experiments in a lumped-element hydraulic model of the circulation. *J. Biomech.* **4**, 335–350.

MEAD, J., TURNER, J. M., MACKLEM, P. T. & LITTLE, J. B. 1967 Significance of the relationship between lung recoil and maximum expiratory flow. *J. Appl. Physiol.* **22**, 95–108.

MILNE-THOMPSON, L. M. 1950 *Theoretical Hydrodynamics*, pp. 515–517. New York: Macmillan.

MORSE, P. M. & INGARD, K. U. 1968 *Theoretical Acoustics*, ch. 4. McGraw-Hill.

OATES, G. C. 1975 Fluid flow in soft-walled tubes; Part 1: Steady flow. *Med. & Biol. Engng* **13**, 773–778.

OLSEN, J. G. & SHAPIRO, A. H. 1967 Large-amplitude unsteady flow in liquid-filled elastic tubes. *J. Fluid Mech.* **29**, 513–538.

PRANDTL, L. 1934 *Fundamentals of Hydrodynamics and Aerodynamics* (transl. by O. G. Tietjens), p. 243. McGraw-Hill.

ROBERTS, V. C. & COTTON, L. T. 1975 Mechanical methods for the prevention of venous thromboembolism. In *Venous Thrombo-Embolic Disease* (ed. C. V. Ruckley & I. M. C. Macintyre), ch. 2. Edinburgh: Churchill Livingstone.

ROSS, B. B., GRAMIAK, R. & RAHN, H. 1955 Physical dynamics of the cough mechanism. *J. Appl. Physiol.* **8**, 264–268.

RUDINGER, G. 1970 Shock waves in mathematical models of the aorta. *Trans. A.S.M.E., J. Appl. Mech.* **37**, 34–37.

SCHLICHTING, H. 1960 *Boundary Layer Theory*, ch. 20. McGraw-Hill.

SHAPIRO, A. H. & HAWTHORNE, W. R. 1947 The mechanics and thermodynamics of steady one-dimensional gas flow. *J. Appl. Mech.* **14**, A317–A336.

SHAPIRO, A. H. 1977*a* Physiologic and medical aspects of flow in collapsible tubes. *Proc. 6th Canadian Cong. Appl. Mech. Vancouver*, pp. 883–906.

SHAPIRO, A. H. 1977*b* Steady flow in collapsible tubes. *J. Biomech. Engng* **99**, 126–147.

SOROFF, H. S., GIRON, F., RUIZ, U., BIRTWELL, W. C., HIRSCH, L. J. & DETERLING, R. A. 1969 Physiologic support of heart action. *New England J. Med.* **280**, 693–704.

WEISSMAN, K. & MOCKROS, L. 1967 The mechanics of a collapsing tube heart pump. *Int. J. Mech. Sci.* **9**, 113–121.

WEXLER, L., BERGEL, D. H., GABE, I. T., MAKIN, G. S. & MILLS, C. J. 1968 Velocity of blood flow in normal human venae cavae. *Circ. Res.* **23**, 349–359.

WHITHAM, G. B. 1974 *Linear and Nonlinear Waves*, pp. 164–167. Wiley.